Universität Trier

Bachelor's Thesis

Sea Ice Surface Roughness from Single Beam Laser Altimeter Measurements

Method Development and Comparison with Airborne Laser Scanner Profiles

Trier, 30.09.2021.

1st Supervisor: Dr. Sascha Willmes

2nd Supervisor: Univ. Prof. Dr. Günther Heinemann

Author: Mira Suhrhoff

                1356630

                s6misuhr@uni-trier.de

Contents

3

1 Introduction

The Arctic is a region that is undergoing major changes and is strongly affected by climate change. It is a place where surface temperatures have increased at more than double the global average (Thoman et al. 2020). Since 1979, a decline in Arctic sea ice extent has been observed in every month of the year, with the greatest changes occurring in autumn with a loss of 13.1 % per decade (September 1979-2020) (Perovich et al. 2020) along with a decrease in ice thickness and age (Schweiger et al. 2021, Krumpen et al. 2019). The loss of sea ice with a regime shift towards younger and thinner ice results in lower mean albedo and increased absorption of solar energy, further accelerating the warming process. This is known as an ice-albedo feedback loop and could result in the pole soon being ice-free in summer (Notz & Community 2020).

To understand past and future changes, information on sea ice deformation and roughness plays an important role, as it influences and reflects climate variability. Roughness is a characteristic of different sea ice types and is an indicator of ice thickness, divergence, and convergence (Zabel et al. 1996, Peterson et al. 2008, Gegiuc et al. 2018). It is also needed for boundary layer climate modeling because it affects the wind stress and the aerodynamic roughness length (Guest & Davidson 1991, Weiss et al. 2011, Lüpkes et al. 2012) and enhances atmospheric boundary layer turbulence, which in turn affects turbulent energy transfer and boundary layer height (Sturm 2002, Smeets et al. 1999). In addition, sea ice roughness in late winter was found to be the largest contributor to the variance in ice albedo in late summer (Landy et al. 2015). Roughness affects the lateral extent of melt ponds (Eicken et al. 2004), which have lower albedo. Thus, sea ice roughness is also a predictive indicator of Arctic sea ice albedo. However, current ice-ocean models are unable to capture the heterogeneity of sea ice deformation (Girard et al. 2009). Instead, the surface roughness of sea ice is overlooked and often either ignored or misrepresented by current methods (Landy et al. 2020). Taking it into account can improve sea ice estimations and predictions.

The objective of this study is to develop a routine for deriving sea ice surface profiles from airborne laser altimeter data and their characteristics in terms of pressure ridges and roughness. This is based on a three-step filtering procedure by Hibler (1972), which

has already been widely used by others. It has been used to detect pressure ridges and to determine their height (Bing et al. 2013, Lewis et al. 1993, Castellani et al. 2014, Tan et al. 2012, Rabenstein et al. 2010), their spacing (Bing et al. 2013, Castellani et al. 2014, Tan et al. 2012, Rabenstein et al. 2010), as well as the height distribution (Lewis et al. 1993), density (Lewis et al. 1993, Rabenstein et al. 2010), and intensity (Bing et al. 2013, Tan et al. 2012). In addition, surface profiles are commonly used to calculate sea ice surface roughness (Lange et al. 2019, Johansson et al. 2017, Bing et al. 2013, Saldern et al. 2006, Prinsenberg et al. 2006, Lewis et al. 1993, Fors et al. 2016, Peterson et al. 2002, 2008). These parameters have been used to statistically analyze sea ice surface profiles (Lewis et al. 1993), investigate the morphology and distribution of pressure ridges in the northwestern Wedell Sea (Tan et al. 2012), improve the classification of ice thickness regimes (Saldern et al. 2006), to better understand the influence of sea ice topography and pressure ridges on atmospheric surface drag (Bing et al. 2013, Castellani et al. 2014), to distinguish between level ice and deformed ice (Lange et al. 2019), or to analyze and characterize ice regimes of different ages and different deformation stages (Rabenstein et al. 2010).

The Alfred-Wegener-Institute for Polar and Marine Research (AWI) has collected a large data set of surface laser measurements during several aircraft and helicopter campaigns with an EM bird over the last two decades. This data set will be analysed in the future with regard to trends, temporal variability of sea ice surface roughness in key areas and possible connections with important variables such as ice thickness and ice age. The aim of this study is therefore to review previous studies and to develop a suitable method as well as to test and improve it, which includes a comparison with airborne laser scanner data. The method will be implemented in a processing chain that allows automated extraction of roughness information from previous and future campaigns.

2 The Arctic Sea Ice

2.1 The Arctic

As one of the polar regions, the Arctic is a key component of the global climate system that interacts with the rest of the world through shared oceans, atmospheres, ecological and social systems (Meredith et al. 2019). The Arctic, the northernmost region on Earth, is defined in various forms. Climatically, the Arctic can be defined by the July 10°C isotherm. It is an imaginary line north of which the multi-year average monthly mean temperature is below 10°C, even in the warmest month of the year. It encloses the entire Arctic Ocean as well as Greenland, Svalbard, most of Iceland and the northern coast and islands of Russia, Canada and Alaska. This boundary closely corresponds to the northern limit of tree growth, which is used as a botanic definition of the Arctic. Another common but rather simplistic and outdated method to describe the region is the Arctic Circle at 66°33' N. It is the latitude that corresponds to the southern limit of the midnight sun (AMAP 1998).

Within the Arctic region lies the Arctic Ocean that covers an area of 15.551·10^6 km^2 (Jakobsson 2002) and thus is the smallest of the world's five major oceans. Another approach to geographically delimit the Arctic marine environment is the AMAP (Arctic Monitoring and Assessment Programme) boundary. Thereafter, the Arctic marine area covers $20 \cdot 10^6$ km^2 and includes the Arctic Ocean, the adjacent shelf seas (Beaufort, Chukchi, East Siberian, Laptev, Kara, and Barents Seas), the Nordic Seas (Greenland, Norwegian, and Iceland Seas), the Labrador Sea, Baffin Bay, Hudson Bay, the Canadian Arctic Archipelago and the Bering Sea. It connects to the North Atlantic Ocean through Fram Strait, a deep passage between Svalbard and Greenland, and via the Nordic Seas. An additional smaller connection to the Pacific Ocean is formed by Bering Strait (Wadhams 2014).

The Arctic climate is, due to its location, influenced by the strongly variable solar radiation. While the Arctic region receives most solar radiation in summer, with a maximum in June sometimes exceeding 340 W/m², it is almost completely absent in the winter months (Serreze et al. 1998). Still, the annual amount of received radiation is less than

in other parts of the world, which leads to characteristic cold air temperatures and a redistribution of heat from southern regions by air and ocean currents (AMAP 1998). The radiation imbalance thus is a fundamental driver in the Arctic climate system. It is also the reason for seasonal changes in one of the Arctic's most important climate variables, sea ice (Meredith et al. 2019). Sea ice is a predominant feature of the Arctic that covers large parts of the Ocean throughout the year. The extent varies seasonally with the varying strength of solar radiation, as can be seen in figure 2.1. An annual minimum is reached in September with almost 4 million km^2 (2020) whereas in March, the annual maximum, the sea ice covers almost 15 million km^2 (Perovich et al. 2020). Further its extent varies on a interannual and interdecadal time scale due to various reasons such as atmospheric pressure anomalies or the influx of Atlantic and Pacific waters (AMAP 1998).
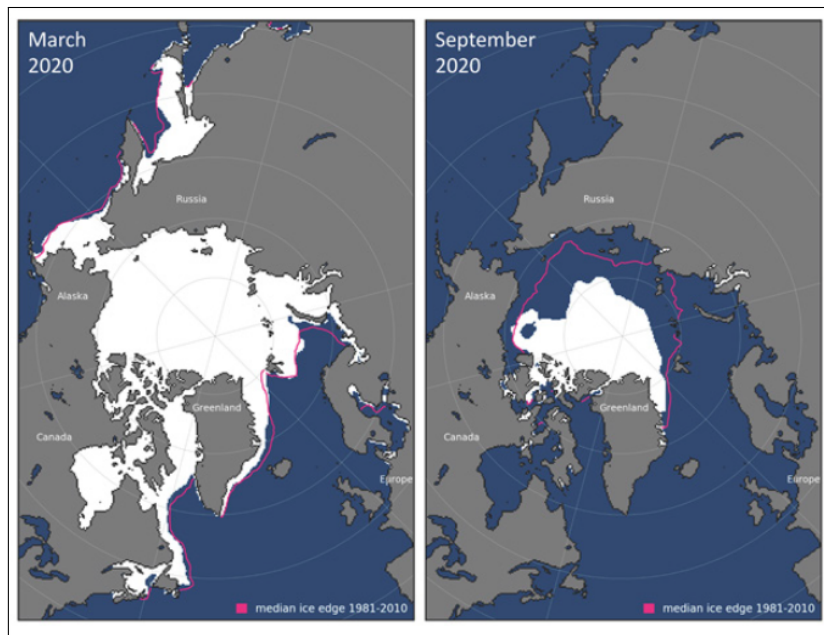

Figure 2.1: Average monthly sea ice extent in March (left) and September (right) 2020 that illustrates the winter maximum and summer minimum extent. The magenta line indicates the median ice extents in March and September, during the period 1981-2010 (Perovich et al. 2020).

2.2 The Sea Ice Cover

2.2.1 Sea Ice Formation and Types

Sea ice is a part of the earth's cryosphere that forms due to a freezing of sea water. It builds a solid layer made up of brine, ice crystals, air, and solid salts, which floats on the water surface and acts as a boundary layer between ocean and atmosphere (Marshall 2012). The freezing point in seawater and the temperature at which the water reaches its maximum density are depressed by dissolved salts. Seawater with an average salinity of 34.5 psu (practical salinity units) freezes therefore at -1.86°C (Petrich & Eicken 2009, Marshall 2012). Both the freezing point and the temperature of the maximum density decreases linearly with increasing salinity. However, the temperature of the density maximum decreases faster and exceeds the freezing point at 24.7 psu (Hay et al. 1998, Wadhams 2014). Thus the density of water with a salt content above 24.7 psu increases continuously as it cools to the point where it freezes. It is the reason why the ocean water, whose salinity is usually above 24.7 psu, experiences thermohaline convection. Meaning cool and dense surface water sinks and is replaced by warmer water from the depths, which in turn is cooled. This process continues until water temperatures reach the freezing point and sea ice forms.

Different development stages of sea ice are defined in the Sea Ice Nomenclature by the WMO (2014). Initially ice crystals grow under calm conditions that float on the surface in the form of tiny discs with a diameter of less than 2-3 mm (Wadhams 2014) and can break up under turbulence. Suspended in water, these ice crystals are shaped like needles, fine spicules and plates. That is a type of new ice called frazil ice or grease ice. In addition to the ice, formed by the growth of ice crystals on the water surface, it can also be formed by heavy snowfall. In that case snow saturated and mixed with water forms a vicious floating mass, referred to as slush ice. These types of ice can accumulate into spongy white lumps of ice a few centimetres in size. The formation of these new ice types builds a first layer on the ocean's surface that reduces the influence of wind stress and heat exchange and therefore the effect of thermohaline mixing. Under calm conditions and following a further freezing, the ice crystals form a thin elastic crust of ice up to 10 cm in thickness, called nilas. Once formed, the ice eventually thickens though a different process called congelation growth where water molecules freeze on the bottom of the ice cover. Through it sea ice in the Arctic can reach a thickness of 1.5 - 2 m thickness in one single season (Wadhams 2014).
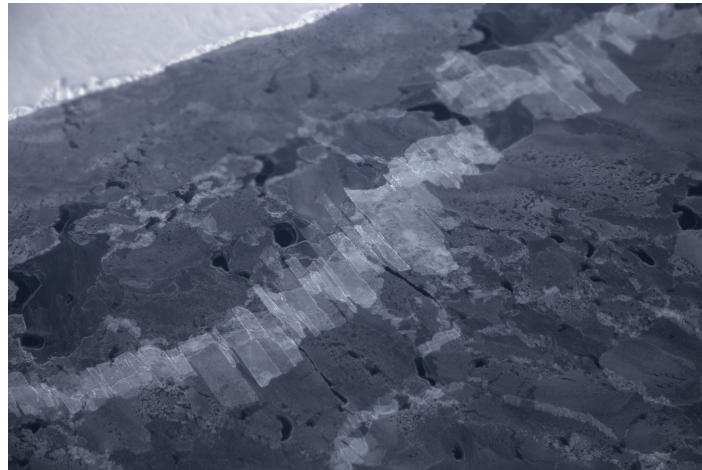
Figure 2.2: Nilas that form in an area of open water (Jeremy Harbeck / NASA).

Under turbulent water conditions different types of sea ice form. The dynamic environment favours the growth of frazil ice, often containing a dense suspension of it (Wadhams 2014). In this environment, the so-called pancake ice forms predominantly. It is ice composed of mostly circular pieces from 30 cm - 3 m in diameter and up to 10 cm in thickness with raised rims due to the collision of these pieces against one another. On a slight swell it forms from accretion of frazil crystals and under more severe swells and waves as a result of breaking nilas. Later the individual pancakes eventually consolidate trough frazil growth and congelation, forming consolidated pancake ice with an irregular and rough surface topography (Petrich & Eicken 2009, Wadhams 2014).

Figure 2.3: Pancake ice (Peter Lemke / AWI).

Both sea ice that has formed under calm conditions and sea ice formed in turbulent ones, is classified as first-year ice (FYI) as long as it is not older than one season. Its thickness ranges between 30 cm and 2 m. As soon as ice survives more than one melting season, it is classified as multi-year ice (MYI). It is mainly found in the central Arctic ocean and in the east of Greenland and is often thicker than 3 m and rougher compared to first-year ice (AMAP 1998, Wadhams 2014).

Based on its dynamic character, the sea ice landscape can be divided into four different sea ice zones, the landfast ice, shear zone, marginal ice zone and the central pack (Wadhams 1980b, Leppaeranta 2011). Landfast ice or fast ice occurs along the entire rim of the Arctic Ocean and in Subarctic regions (Wadhams 1980b). It is defined by the WMO (2014) as sea ice that forms and remains fast along the coast where it is attached to the shore or between shoals or grounded icebergs. According to Barry et al. (1979) it consists of an inner zone, the bottom fast including the ice foot near the beach, and an outer zone made of floating fast ice beyond the 2 m isobath. Fast ice differs from other sea ice by three factors. First, it remains relatively immobile for a period of time near the coast; second, it extends seaward from the coast as a continuous sheet of ice; and third, it is grounded or forms seaward a continuous sheet of ice to a zone of grounded ice (Barry et al. 1979). This sea ice zone goes through an annual cycle of formation, growth and expansion during the winter and the decay during spring where the ice breaks up, drifts away and exposes open water. The formation and growth of ice during the winter continues seaward where it eventually encounters the moving pack ice (Wadhams 1980b).

Figure 2.4: Fast ice in the Davis Strait, Baffin Island, Canada (Russell Hood / ARCUS).

Under onshore winds the pack ice will be driven towards the coast and deform the fast ice sheet. The result is an irregular relief composed of ice blocks that can pile up and form pressure ridges. These pressure ridges can grow large enough to become grounded to the seabed if the pressure exerted by the pack ice is high enough. Grounded ridges may also originate from the pack ice itself and be incorporated into the fast ice sheet. They form anchoring points, which stabilize the fast ice and can have a scouring effect on the seabed (Wadhams 1980*b*). A typical winter formation of landfast ice thus consists of a smooth inner ice sheet, which with increasing distance from the coast more often also includes floes and ridges, and finally the outermost zone, which consists of heavily deformed ice. It is sometimes separated from the shear zone, the adjacent sea ice zone of the moving pack, by a flaw lead (Wadhams 1980*b*). This is a narrow band where pieces of ice are in a chaotic state that forms when drift ice shears along the fast ice edge.

The shear zone forms when the pack ice moves against a fixed boundary of either land of landfast ice. The motion results in an area with widths up to 200 km (Leppaeranta 2011) composed of highly deformed ice with an ridging intensity often higher than that in the open ocean (Wadhams 1980*b*). It, together with landfast ice, forms a boundary oriented towards the coast.
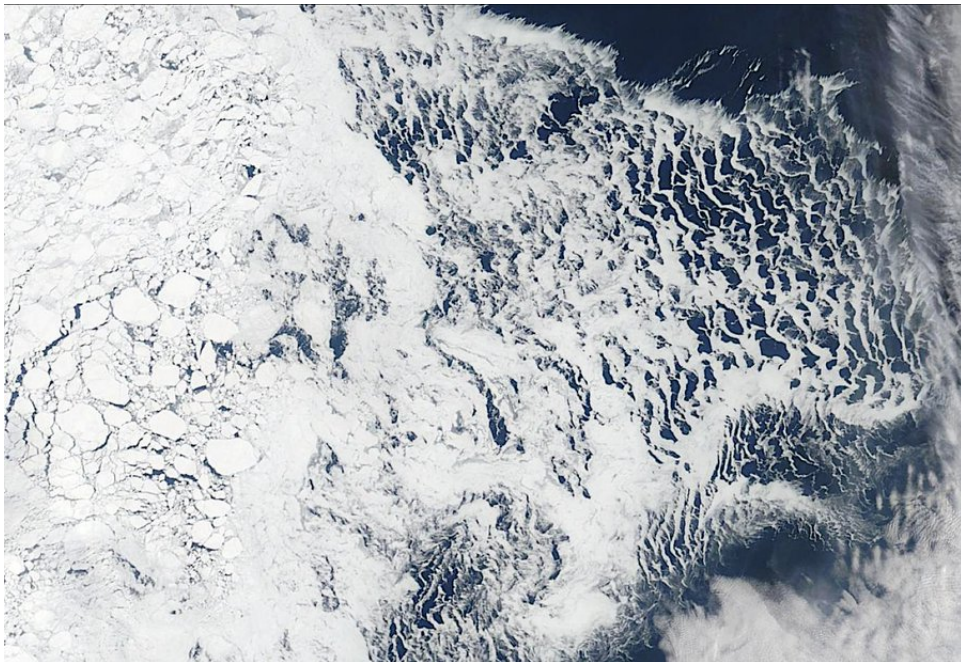

Figure 2.5: Marginal ice zone in the Barents Sea (worldview.earthdata.nasa.gov 17.04.20).

The boundary towards the open ocean is marked by the marginal ice zone (MIZ). It is the region of an ice cover that is affected by incoming waves and swells from the open ocean. The ice responds to the influence by bending until the stress is too high and it fractures, relieving flexural stress and breaking into smaller floes (Wadhams 1980b). The depth of penetration to which waves can fracture ice to create floes is taken to be the width of the MIZ (Wadhams 2014). The ice at the outermost edge is most affected by the open ocean and therefore the place where the smallest ice floes are found. Larger floes can be found further away from the edge where the ice is partially protected. By this theory, the floe size should increase with the distance to the edge. In reality the gradation to large floes is not continuous and often banding can be observed where belts of smaller floes are found between belts of larger floes (Wadhams 1980b). The high temporal and spatial variability of ice conditions and its intense air-ice-sea interactions are the main characteristics of the MIZ. Wind blowing towards the ice edge from the open sea compresses the MIZ ice field. It leads to an compact ice field with a sharp outer boundary of small fragments. In comparison, the MIZ is diffused as a result of wind blowing away from the edge and compact ice bands are formed that are separated by open water. And lastly, the central pack ice zone, often referred to as drift ice, is located within the MIZ boundary. It is free from direct influences originating from the borders. The extent of the pack ice depends on the basin itself and is therefore only found in large seas (Leppaeranta 2011).

2.2.2 Sea Ice Surface Features

The Sea Ice landscape is not an uniform sheet of level ice, but rather it is very complex and composed of various structures, some of which are presented here in an overview.
One fundamental part of the sea ice cover are ice floes. An ice floe is defined as any contiguous piece of sea ice, with different size classes of small to medium, big, vast and giant with a diameter of 20 m to 100 km in diameter. These floes can move and collide with each other and form pressure ridges, which are defined as a linear wall of broken ice along a fracture line forced up by pressure. Ridges consist of a keel, the part below the water surface, and a sail, the part above, and will be discussed in more detail in section 2.4.1. In case of long and lasting pressure, they can merge into rubble fields, areas of extremely heavily deformed sea ice of unusual thickness with deep ridges and randomly scattered and tilted ice blocks. Similar to ridges are hummocks. These are composed of broken ice and floe pieces that have been forced up by pressure but without a longitudinal extension. Rather, they form hills of ice blocks as they experience pressure from more than one side (WMO 2014).

Other common features of the sea ice landscape are leads and polynyas. They are openings of the ice cover and regions of open water and/or reduced ice extend. A lead is any fracture or passage-way through sea ice which is navigable by surface vessels (WMO 2014). They are linear features opened by forces of wind or ocean currents up to a couple of metres to a few kilometres wide and tens of kilometres long (Thomas & Dieckmann 2009). The highest density of leads can be seen in early winter and is associated with large-scale fields of ice divergence and shear (Willmes & Heinemann 2016). In winter, when the temperatures between the atmosphere and the water differ greatly, they will refreeze quickly or otherwise can be closed again by the movement of the ice (Barry & Gan 2011).
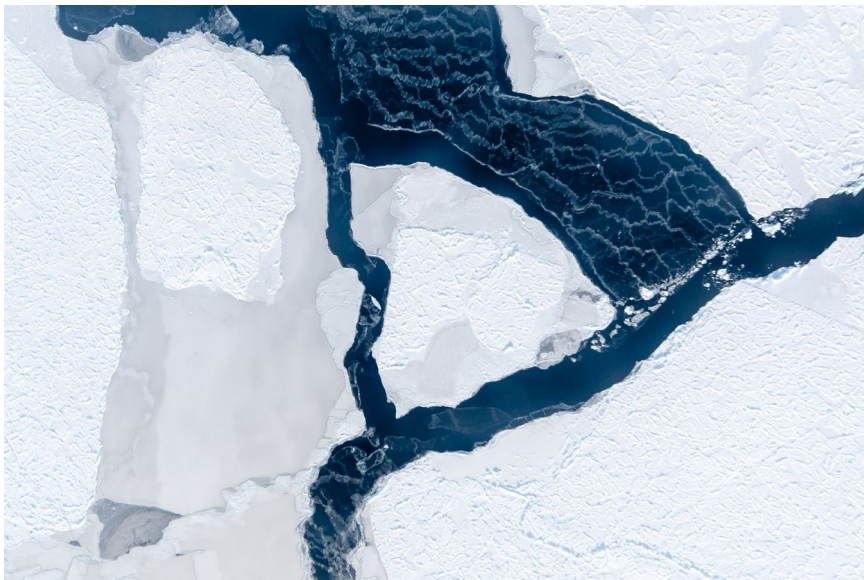
Figure 2.6: A lead created by wind that causes the ice to drift apart, exposing open water areas where new sea ice can form (Stefan Hendricks / AWI).

A polynya is any non-linear shaped opening enclosed in ice (WMO 2014). They are either persistent or recurring, often at fixed geographical locations, and can reach tens to tens of thousand square kilometres (Wadhams 2014). Commonly, two types of polynyas are distinguished, the sensible-heat polynya and latent-heat polynya. Sensible-heat polynyas are thermally driven through convection and typically formed in regions of upwelling, strong vertical mixing or strong interactions between ocean currents and topographic features. Here, the sensible heat content of the surface waters are reduced because heat is transferred from the ocean to the atmosphere. The flux of warm water to the surface

prevents ice formation and at the same time limits the area of this polynya (Wadhams 2014). Latent-heat polynyas are mechanically driven through ice-divergence and form through offshore winds along coastlines or down winds or currents of land-fast ice, glacier tongues or grounded ice bergs. Here, latent heat is removed from the water, which allows the oceanic water to form new ice that is again mechanically driven away (Thomas & Dieckmann 2009).

Furthermore, the morphology of the sea ice surface is influenced by its snow cover. At the end of winter its thickness averages between 30 and 40 cm with local variation (Barry & Gan 2011). After a snowfall, winds can cause redistribution of snow and erosion of the sea ice surface. The result is a heterogeneous distribution of snow thickness that can increase the surface topography, especially on level ice (Barry & Gan 2011). It accumulates preferentially in snowdrifts and downwind of morphological features (Sturm et al. 1998), such as ridges, and can locally exceed 1 m in thickness (Barry & Gan 2011). On the other hand, snow can reduce the roughness of the ice surface and smooth it by drifting in and around of rough sea ice structures (Sturm et al. 1998). On a small scale the snow relief is classified into three different types (Goodwin 1990). First, stationary depositional features form during precipitation from wind transported snow, such as dune fields. Second, redistributional features form as a result of the erosion of depositional features, such as sastrugi. These can be described as sharp and irregular ridges, which are aligned with the wind direction (Warren et al. 1999). Usually sastrugi reach heights of 0.3 m and in extreme cases they can be up to 2 m tall (Goodwin 1990) And lastly the relief contains erosional features form from the long-term exposure to winds. These can be glazed surfaces, which consist of a single snow-grain thickness layer cemented by a thin film of ice that is created by the kinetic heating under a constantly strong wind flow (Goodwin 1990). An then in late May - June the snow melts until July when most of it is gone. The melt water accumulates on the sea ice surface in meltponds and gradually forms an interlinked network (Barry & Gan 2011). Their extent is influenced by the surface roughness. Melt water on smooth ice can spread laterally, which results in larger ponds. On rougher surfaces, the melt water accumulates in crevices and in between roughness features, thus is spatially confined (Nolin & Mar 2019). The variability of melt ponds is the highest at the beginning of the melt season with 5 - 50 %. As melting progresses, the extent of melt ponds increases, while their extent often decreases on thicker, older ice due to drainage. This is important because melt ponds on sea ice greatly reduce albedo and lead to a positive ice-albedo feedback (Landy et al. 2015).

2.3 Sea Ice in Motion

2.3.1 The Momentum Balance

Most of the sea ice covering the Arctic is almost constantly in motion, affecting the ice sheet and changing the morphology of the sea ice. As a result, features such as ridges, leads, and polynyas are formed. This movement can be described by the momentum balance (Wadhams 2014). It considers the forces acting on a unit of the ice cover.

$$\text{Mass} \times \text{Acceleration} = \text{Air Stress} + \text{Water Stress} + \text{Coriolis Force} + \text{Internal Ice Stress} \quad (2.1)$$

$$M \times \; a = \tau_a + \tau_w + \tau_c + \tau_j + \tau_t \quad (2.2)$$

Thorndike & Colony (1982) found that sea ice moves on a time scale of one day or longer primarily in response to local winds and ocean currents. Thus, the most important driving forces for sea ice drift are air and water stress. Both contribute equally to ice movement over the long term (several months). Only on a shorter time scale (days to months) does wind contribute more than 70 % of the velocity in the central Arctic Ocean. The Coriolis force exerts the least influence on ice motion. It is the force that directs sea ice, icebergs, ocean currents, and global winds in the Northern Hemisphere to the right due to the Earth's rotation.
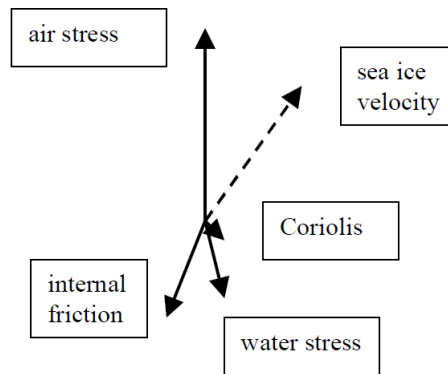

Figure 2.7: The major forces of drifting sea ice in the northern hemisphere (Leppaeranta 2011)

Another force acting on sea ice comes from the tilt of the ocean surface. This force arises because the height of the sea surface is partially different from that of the geoid. The geoid defines the surface on which the gravitational potential is constant. Thus, a tilt of the sea surface causes a horizontal pressure gradient that attempts to move the surface water and may affect the movement of sea ice to a small degree. And finally, the internal ice stress contributes to the momentum balance. The force develops when the ice experiences pressure transmitted through the surrounding ice sheet. The internal stress is the sum of the variable environmental stresses acting on the ice, as well as the rheology (the way the ice as a material responds to different types of stresses), strength, and thickness distribution of the ice sheet. In a state of free drift, the factor of internal stress is negligible. However, it plays an important role in close pack ice or enclosed seas and channels (Wadhams 2014).

2.3.2 Air Stress and Roughness

It could be observed that the wind stress acting on the surface of sea ice is proportional to the square of the wind speed relative to the surface (Wadhams 2014). This relationship is expressed by the constant of proportionality called drag coefficient. It is a function of the surface roughness (Banke et al. 1976) and thus important to model the response of sea ice in the wind field. The atmospheric drag over sea-ice can be expressed as

$$\tau_a = \rho_a u_*^2 = \rho_a C_{dn}(z) U^2(z) \tag{2.3}$$

with the air density ρ_a, the friction velocity over sea ice u_*, the average wind speed U and the air-ice drag coefficient C_a at the reference height z (10 m for wind measurements are recommended by the WMO) (Wadhams 2014).
It is a common approach to divide the drag coefficient into coefficients for small and large scale roughness (Arya 1973, 1975, Banke et al. 1976). The skin friction drag forms on top of undeformed ice whereas the form drag is a result of larger obstacles on the ice surface, i.e. pressure ridges, rafted ice, and vertical floe edges (Wadhams 2014). Several attempts have been made to relate the air-ice drag coefficient C_a to the measurable and variable surface roughness. Banke et al. (1976) suggested the equation

$$C_a = C_{10} + (C_f hn/2) \tag{2.4}$$

where the skin friction drag coefficient C_{10} varies between 0.0013 and 0.0021 for various surfaces and the form drag coefficient C_f ranges between 0.3 and 0.4 depending on the age of pressure ridges. The variation of the drag is thus largely determined by the the mean ridge height h and the number of ridges n.

Wadhams (2014) commented that this approach is too simplistic. First of all, undeformed ice can be subject to strong roughness variations as well and cannot be assumed more or less constant. This is the case especially for pancake or multi-year ice. Moreover, it is difficult to identify individual ridges on heavily deformed sea ice such as rubble fields. Furthermore, ice in the marginal ice zone has a higher drag coefficient due to floe edges that can vary quickly when floes break into smaller pieces. And lastly, he commented that the equation lacks information about the stability of the near-surface wind flow. This is because the air temperature compared to that of the sea ice has an influence on the development of surface drag. It is therefore very difficult to define generally valid values. However, from air-ice drag coefficients given in Guest et al. (1995) it can be said that grease ice, nilas and small pancake ice accounts for the smallest drag coefficient. They even offer a smaller surface for wind stress than open water. Multi-year ice mostly has higher drag coefficients than first-year ice. However, all drag coefficients can vary strongly between a smooth and rough surfaces. Another attempt to the influence of roughness is given by Arya (1975), who suggested that the total wind drag could be written as the sum of the skin friction drag S_D and the form friction drag F_D.

$$\tau_a = F_D + S_D \tag{2.5}$$

with

$$S_D = (1 - mR_i)\tau_0 \tag{2.6}$$

where R_i is the ratio of the mean ridge height h and the mean ridge spacing s, m = 20, and where τ_0 is the skin friction over sea ice without pressure ridges. Arya (1975) formulates the total form drag under the assumption based on Hibler et al. (1972), that ridging is homogeneous and isotropic in a given areas and that pressure ridges are randomly orientated and thus can be characterized by the mean ridging density R_D (total length of ridges per unit area).

$$F_D = \frac{R_D}{\pi} \int\limits_{h_0}^{\infty} C_{Dh}\rho U_h^2 h P(h) dh \tag{2.7}$$

Here is C_{Dh} the form drag coefficient, $P(h)$ the probability density function of the ridge height and h_0 the lower cut-off height. By specifying the cut-off, surface elevations that contribute mainly to the surface friction and surface elevations that contribute to the form drag can be differentiated.

2.3.3 Large Scale Drift Pattern of Sea Ice in the Arctic

In the Arctic, the drift of sea ice is mainly influenced by two major wind patterns (Timmermans & Marshall 2020). One is the Beaufort High with anticyclonic tendencies, centred above the Canadian Basin. The other one is the Icelandic Low with cyclonic tendencies in the Eurasian Basin, centred outside of the Arctic basin between Iceland and southern Greenland. They are drivers for the two major drifts: the Beaufort Gyre and the Transpolar drift stream.
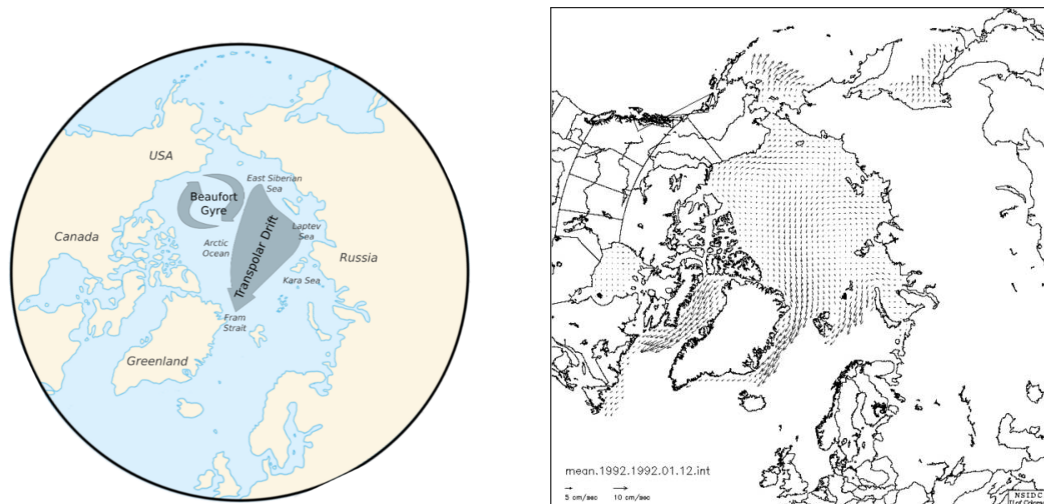
Figure 2.8: The Arctic Ocean and the two major drift systems, the Beaufort Gyre and the Transpolar Drift (right, (AWI 2019)) and the mean annual sea-ice drift (left, NSIDC).

The Beaufort Gyre is the dominant upper-ocean circulation in the Canadian Basin where ice typically takes 7 - 10 years to complete one circuit (Wadhams 2014). The Transpolar drift stream is a flow of ice and water from the coast of Siberia across the Arctic to the North Atlantic via the east cost of Greenland, where it exits the central Arctic Basin. Ice in the Transpolar drift system can be transported up to three years and hence leaves the Arctic more quickly. This route through Fram Strait is where most of the ice leaves the Arctic basin and the biggest water and heat exchanges occurs (Wadhams

2014, Thorndike 1986). Both drift fields are under various influences, e.g., changes in the atmospheric circulation structure. With these influences the position and intensity of drift fields vary from year to year. This variation in turn effects conditions like melt and ice growth and the redistribution of ice in the Arctic Basin as well as its removal through Fram Strait (Volkov et al. 2020).

2.4 Deformation

Sea ice is influenced by thermodynamic and dynamic processes. Thermodynamic processes effect the growth and decay of sea ice systematically over large areas through freezing and melting. The result is most often smooth level ice with a thickness of a few millimetres to an equilibrium thickness of 2-2.5 m (Maykut & Untersteiner 1971). Much thicker ice can be reached through dynamic processes, which deform sea ice and occur locally. This deformation of ice is caused by the drift of sea ice (Marshall 2012). The movement of ice is not regular but reacts quickly to changes in the local wind. In a model presented by Hibler et al. (1992) sea ice reaches a steady drift state within an hour after applying the wind force. The fast reaction and displacement of sea ice in the wind field can be also seen in drift tracks of single ice floes with the randomness of a "drunken march" (Colony & Thorndike 1985). It leads to a motion of ice that can be divided into three different types: divergence, convergence, and shear. Divergence is a dispersive motion that can reduce the ice thickness and relieve stress in the ice cover. It is the cause for openings of the ice cover and formation of leads and polynyas (Marshall 2012). Convergence, by contrast, is a compacting motion that can increase the ice concentration and produce stress. The third type is shear, which comes from ice moving in significantly different directions. The convergence and shear movements cause the deformation of the sea ice. The main deformation processes listed by the WMO (2014) are rafting and ridging. Rafting takes place if the ice is thin and elastic enough that it doesn't break under pressure and floes remain intact while sliding on top of each other. With growing thickness, the ice becomes less elastic and breaks up under the compressive forces. In that case, ice blocks pile up along the fracture zone and form a pressure ridge. Other deformation processes listed by the WMO (2014) are fracturing, hummocking, shore ice ride-up and weathering. Fracturing is described the initial deformation process where the ice deforms permanently under pressure and hummocking is the pressure process by which sea ice is forced into hummocks. Furthermore, sea ice that is subject of shore ice ride up is pushed on land or other structures. Finally, the process of weathering leads to a ablation where irregularities on the sea ice surface are eliminated gradually.

2.4.1 Sea Ice Ridges

The presence of pressure ridges is important for several reasons. First, they are an important factor in the mass balance of sea ice because they contain a large fraction of the mass of the ice sheet. Depending on the degree of deformation, pressure ridges can account for 30-80% of the total ice volume (Wadhams 2014). In addition, their height and spatial distribution is related to the average regional ice thickness. Therefore, this information could contribute to the development of methods for determining ice thickness from remote sensing data based on ice roughness (Wadhams et al. 1992). Moreover, the momentum and heat transfer between the atmosphere and sea ice depends strongly on the aerodynamic roughness of the sea ice and pressure ridges, i.e., their height, mean distance, and intensity (Arya 1973). For ice engineering, ridges are important because they are associated with the highest ice loads on structures within first-year ice fields, scour the seafloor, and affect conditions for navigation and traffic on the ice (Leppaeranta 2011).
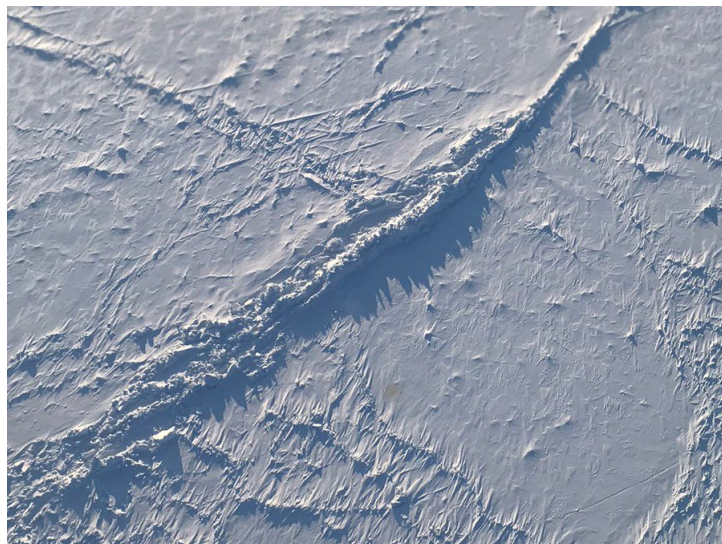
Figure 2.9: A large pressure ridge (NASA).

Ridges are the most important morphological feature of the sea ice surface, along with minor snow drifts and other roughness features (Tan et al. 2012). Pressure ridges are the result of high pressure created when ice floes collide or are compressed and cannot withstand the stress. They are distinguished from shear ridges, which are the result of extensive shearing between ice floes and typically occur at the boundaries between fast ice and the moving pack ice (Kovacs 1970). The accumulated ice blocks can freeze together

and consolidate into a permanent structure. And because of their blocky structure, they contain voids which, in the case of sails, may be filled first with air and later with snow or water that can refreeze and consolidate further (Kovacs et al. 1973).

Pressure ridges depend on the thickness of the parent ice, i.e., the ice from which they originate. The critical thickness at which pressure ridges occur depends on material properties such as temperature and porosity of the ice (Menge & Jones 1993). An average of 15 cm is described as a transitional state at which ridging begins, as the ice is thick enough to break and pile up ice in blocks (Kovacs 1970). The thickness of these ice blocks can be an indicator of ice thickness at the time of ridge formation (Tucker et al. 1984). However, a pressure ridge does not always consist of ice blocks of the same size. Instead, they may contain blocks that can vary by more than 1 m (Tucker & Govoni 1981).

In addition, both height and width are a function of the thickness of the parent ice (Parmerter & Coon 1972, Tucker et al. 1984). In general, the sail height appears to scale with the square root of the ice thickness. The sail height of ridges composed of thin ice blocks may be many times the ice thickness, whereas ridges composed of thicker ice are only 3 to 5 times the thickness (Tucker & Govoni 1981). Consequently, the thickness of the ice is also an indicator of how large a ridge will grow (Tucker et al. 1984). However, other studies do not confirm this relationship. According to Castellani et al. (2014), the correlation between sea ice thickness and ridge height is weak and not significant. Unless the pressure ridge has reached its maximum height after which it continues to grow laterally, its width also depends on the ice thickness (Tucker et al. 1984). The maximum width observed by Sudom et al. (2011) averaged at 13 m, with only a few exceeding 40 m in width.

Ridges can be very complex, variable, and non-symmetrical, but usually have a triangular shape (Timco & Burden 1997). Over time, the shape and characteristics of ridges change. This is also why they are usually classified by age into first- and multi-year ridges. Melt processes change the surface over time, forming a smoother surface. When newly formed, they often have sharp tops and a slope of the troughs of 40°, while highly weathered ridges have rounded tops and slopes of the sides around 20-30° (WMO 2014). Moreover, first-year ridges are usually loose and unconsolidated, while multi-year ridges are often almost completely consolidated (Sudom et al. 2011). In addition, the formation of leads breaks the ridge into a sequence of individual ice blocks, so that the linearity of the ridge is no longer apparent (Wadhams & Toberg 2012). Older ridges also tend to have wider and less deep keels relative to sail height compared to newly formed ridges (Timco & Burden 1997). Although pressure ridges are highly inhomogeneous and have a wide variety of shapes and sizes, relationships between the sail and keel can be

established (Kovacs et al. 1973, Sudom et al. 2011, Strub-Klein & Sudom 2012). For example, Timco & Burden (1997), who examined 112 first-year and 64 multi-year ridges, found clear relationships between sail heights and keel depths, with a ratio of keel to sail height of 4.4 for first-year ridges and 3.3 for multi-year ridges. Typical sail heights are generally between one and two meters (Strub-Klein & Sudom 2012, Duncan et al. 2018), with exceptions of extreme cases where ridge sails also reach 13 m (Kovacs et al. 1973) and ridge keels reach 47 m (Lyon 1963).
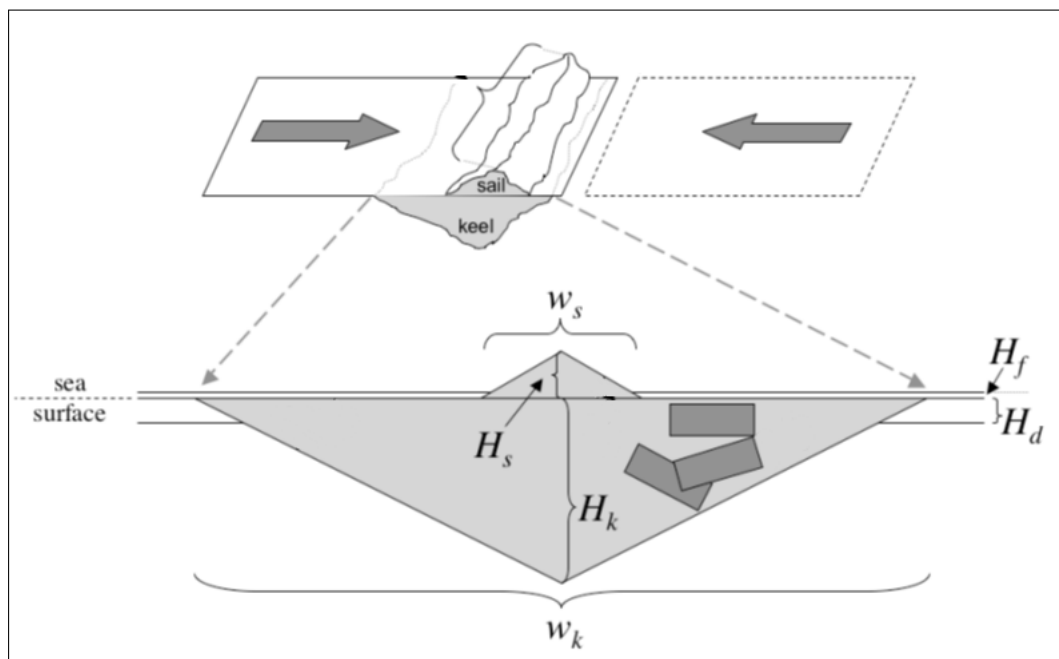
Figure 2.10: Convergent drift of sea ice pushes two ice floes into each other and forms a triangular shaped pressure ridge. The proportions of the sail and keel are scaled according to Timco & Burden (1997). The parameters are sail heigth H_s and width w_s, keel height H_k and width w_k, freebord height H_f and draft depth H_d. (Martin 2007)

The occurrence of ridges and the degree of deformation vary greatly in space and time, as they typically change for different sea ice zones. Ridges are generally more common in coastal zones, at the edge of fast ice, or in shear zones, whereas the degree of ridging is less in the central pack ice and even lesser in the MIZ (Wadhams 1980b). Large variability of ridge characteristics is also observed in different regions of the Arctic. Castellani et al. (2014) studied the height and mean spacing of ridges over 10 km sections in different regions, including the Lincoln and Laptev Seas. The results showed a high spatial vari-

ability. The Lincoln Sea had a high degree of deformation with typical sail heights of 1.5 to 1.6 m and a ridge spacing of 50 m. In contrast, the Laptev Sea exhibited a lower degree of deformation with typical sail heights of 1.1 m and a ridge spacing of 150 to 200 m. In general, there has been a decrease in the occurrence of pressure ridges, particularly multi-year pressure ridges (Wadhams & Toberg 2012). Observations have also shown that, in addition to a thinning of ice over almost the entire Arctic, the greatest loss has been in thick ice, where the volume of ridged ice has decreased more rapidly than that of level ice (Lindsay & Zhang 2005). This is an underlying change in the morphology of the actic sea ice.

3 Instruments and Data

This section provides an overview of the measurement instruments and data. In order to create profiles of the sea ice surface, data from the laser altimeter (_alt.dat) and GPS (_gps.dat) are needed. These measuring instruments are on board of the electromagnetic (EM) bird and are flown over the sea ice by a helicopter or an airplane. In addition, the results of this work are compared with data from a laser scanner. For this purpose, two laser scanner data sets were selected that were recorded simultaneously with those of the laser altimeter and are introduced in this section.

3.1 EM Bird

The so-called EM bird is a system developed by the Alfred-Wegener Institute (AWI) for systematic measurements off the ice thickness with a helicopter or aircraft for a better study of climate and polar oceanography. It uses the geophysical electromagnetic (EM) induction method to determine the height of the instrument above the water surface by examining the different conductivity between sea ice and water. In addition, a laser altimeter measures the height of the EM system above the ice surface. The ice thickness then is the difference between the electromagnetically determined height of the ice underside and the height above the ice surface from laser measurements. It is the sum of snow and ice thickness (Haas et al. 2009).

The EM system is composed of the EM bird, a towing cable and devices inside the helicopter for system control and power supply. Towed to a 20 or 30 m long cable the bird is flown at typical flights speed of 80 to 90 knots at altitudes of 10 to 20 m above the ice surface. Thereby the bird is stabilized during the flight by the presence of a "drag assembly" near the trailing end (Holladay et al. 1997). The EM bird itself is 3.5 m long with a diameter of 0.35 m and 105 kg. Its size and weight makes it possible to be shipped to remote places and also allows for more complicated operations such as from helicopter decks of icebreakers. All measuring instruments are mounted on a plate within a cylindrical kevlar shell (see figure 3.1). On the front and rear ends are the EM coils for electromagnetic induction sounding together with a computer in the center and the

laser altimeter at the bird's nose. Furthermore, a Differential Global Positioning System (DGPS) antenna is mounted on top of the shell.
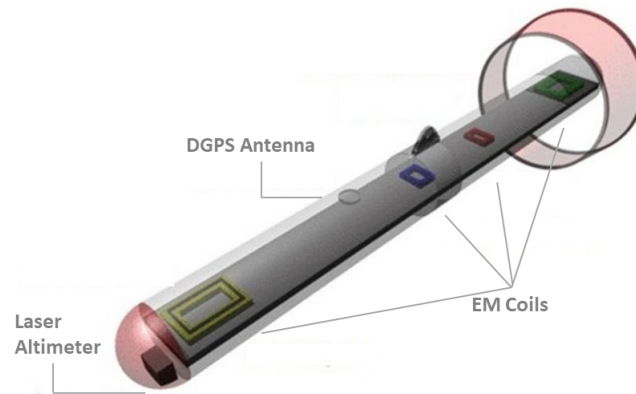
Figure 3.1: The elements of the EM Bird (top, AWI) as it is lifted by the shipboard helicopter (bottom right, AWI) and flown over the ice (bottom left, AWI).

The method of electromagnetic induction sounding has now been used for several decades for measurement of ice thickness. Extensive surface-based EM measurements of ice thickness by Kovacs & Morey (1991) provided the necessary basis for the development of Airborne electromagnetic (AEM) systems. Helicopter-electromagnetic (HEM) mapping of sea ice thickness began in the 1980s in North America and Canada and has been conducted in Europe since the early 1990s (Kovacs et al. 1987, Kovacs & Holladay 1990). The first European helicopter-based measurements of ice thickness using this principle

were carried out in the Baltic Sea by the Geological Survey of Finland (Multala et al. 1996). The Alfred Wegener Institute itself developed a small, digital HEM system in the late 1990s for ship- and land-based expeditions to measure sea ice in the Arctic, Antarctica, and Baltic Seas (Pfaffling et al. 2004, Haas et al. 2009). It has already been operated from several different helicopter types, such as MD500, AS350, Bell 206, BO 105, Bell 212 and MI-8.

3.2 Laser Altimeter

The Laser Altimeter, looking vertically downward, measures the height of the EM system above the ice, based on time-of-flight measurements at wavelengths of 905 nm (invisible, near-infrared) with a frequency of 100 Hz. For a flying speed of 80 to 90 knots this results in a point spacing of 30 - 40 cm. Until 2018, the Alfred-Wegener Institute used a the Riegl LD90-3100HS distance meter. It is a high-speed altimeter with an typical accuracy of ± 15 mm (in the worst case ± 50 mm) (Riegl 2010). The divergence of the infrared measuring beam is 1.8 mrad. At a height of 20 m, the footprint on the ground is thus approximately 3.6 cm. The Riegl LD90-3100HS has a semiconductor laser diode that converts energy from an electrical pulse generator into infrared light pulses, which are transmitted by a collimating lens. The reflected echo signal is received through a receiving lens and hits a photodiode. There, an electrical signal is generated, which is then processed by a micro-computer. The distance between the laser and the target is calculated from the time interval between the transmitted and received pulse (Riegl 2010). Later the Riegl LD90-3100HS was replaced by a Jenoptik LDM301 laser altimeter. It measures with a precision of ± 60 mm and has a similar beam divergence of 1.7 mrad (Jenoptik 2017).

3.3 Data

3.3.1 _alt.dat

Laser Altimeter measurements are stored in files with the ending _alt.dat. The filename consist of the date and time when the data recording was started.

<year><month><day><hour><minute>_alt.dat

Example: 201108021245_alt.dat

Each file has a header line and the columns:

1. fid_alt: Fiducial number (serves as timestamp)

2. height: Laser range (height) in meter (Fill value: 999.99)

3. echo: The echo strength (dummy value for some altimeter type)

4. N: Data rate per 10 Hz telegram

Table 3.1: Sample of the _alt.dat file

fid_alt	height	echo	N
58088.000000	16.38	69	10
58088.100000	16.36	69	10
58088.200000	16.32	69	10
58088.300000	16.30	67	10
58088.400000	16.24	69	10
58088.500000	16.22	69	10
58088.600000	16.22	69	10
58088.700000	16.22	68	10
58088.800000	16.20	70	10
58088.900000	16.22	69	10
58089.000000	16.24	70	10

Looking at the flight data, one can see a pattern of measurements at alternating low and high altitudes (see figure 3.2). At low altitudes, the actual ice thickness is measured, whereas the bird ascends to more than 100 m every 15 to 20 minutes to monitor and correct for electrical system drift. No surface height measurements are available during such ascents. Therefore, sections where the altimeter is raised to more than 20 m are filtered out.
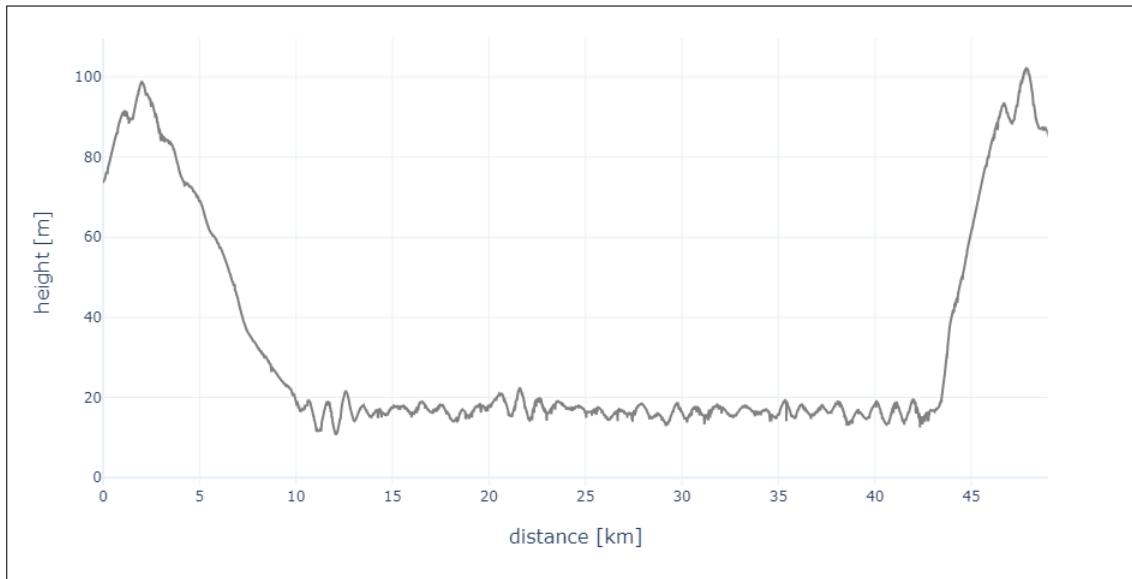
Figure 3.2: Laser Altimeter profile with measurements at alternating low and high altitudes.

3.3.2 _gps.dat

The EM system further provides data of the geolocation and the reference time. The filename consist of the date and time of the measurements.

<year><month><day><hour><minute>_gps.dat

Example: 201108021245_gps.dat

Each file contains a header line and the columns:

1. gpsweek: GPS week (0: dummy value for newer file versions)

2. gpsseconds: GPS seconds of the week (or seconds of the data if GPS week is dummy value)

3. lat: Latitude in degrees north

4. lon: Longitude in degrees east

5. gpsheight: WGS84 elevation in meter

6. gpsfid: Fiducial number (serves as timestamp)

7. gpsspd: GPS speed in meter/sec (0.0: dummy value for newer file versions)

8. gpsdir: True heading in degrees (0.0: dummy value for newer file versions)

Table 3.2: Sample of a _gps.dat file

gpsweek	gpsseconds	lat	lon	gpsheight	gpsfid	gpsspd	gpsdir
300	228427.500000	78.587203	-6.239855	19.827000	58002	27.522000	198.167000
300	228428.500000	78.586973	-6.240241	21.045000	58012	26.971000	198.158000
300	228429.500000	78.586748	-6.240612	22.288000	58022	26.338000	197.737000
300	228430.500000	78.586526	-6.240956	23.271000	58032	25.803000	197.082000
300	228431.500000	78.586304	-6.241284	22.942000	58042	25.530000	195.812000
300	228432.500000	78.586085	-6.241579	23.759000	58052	25.621000	194.892000
300	228433.500000	78.585861	-6.241879	23.381000	58062	26.000000	194.587000
300	228434.500000	78.585633	-6.242179	22.372000	58072	26.525000	195.404000
300	228435.500000	78.585401	-6.242521	21.284000	58082	27.046000	196.178000
300	228436.500000	78.585166	-6.242880	20.492000	58092	27.593000	196.794000
300	228437.500000	78.584927	-6.243264	19.801000	58102	28.085000	197.556000

The GPS data is used to assign the measurement points to geographical positions. Both files, _alt.dat and _gps.dat, can be merged via the columns "fid" and "gpsfid". When merging the data, it should be considered that the measuring frequency of the laser is greater by a factor of 10. The surface height is measured by the laser with a frequency of 100 Hz, while the GPS data is recorded with a frequency of 10 Hz. This means there are 10 laser measurements between two GPS points. To determine the geographic coordinates for each of these points, the coordinates are linearly interpolated. It is assumed that the speed does not change between the two GPS points.

The distance between GPS coordinates was calculated using the Haversine Formula (Sinnott 1984)

$$a = \sin^2(\Delta\phi/2) + \cos\phi_1 \cdot \cos\phi_2 \cdot \sin^2(\Delta\lambda/2) \tag{3.1}$$

$$c = 2 \cdot atan2(\sqrt{a}, \sqrt{(1\text{-}a)}) \tag{3.2}$$

$$d = R \cdot c \tag{3.3}$$

where ϕ is the latitude, λ is the longitude and R is the earth's radius (mean radius = 6,371 km). Together with the number of measuring points, an average point spacing of the profiles can be calculated. Compared to the expected value of 0.3-0.4 m, the average point spacing is usually several centimeters to decimeters higher.

3.4 Airborne Laser Scanner

In addition to the EM bird, the scientific instrumentation of some flight campaigns includes an airborne laser scanner (ALS). It provides high-resolution information of the sea ice topography and is used to estimate the surface roughness as well as freeboard that supplement snow and ice measurements from remote sensing and snow radar.

The ALS data is used for comparison with laser altimeter data and was acquired within the IceBird aircraft campaign of the Alfred Wegener Institute in April 2019[1] that was equipped with a set of different sensors (EM bird, Airborne Laserscanner, Snow Radar) for direct observations of snow freeboard, snow depth on sea ice and sea ice thickness. Installed in the Polar-6 campaign was the laser scanner model called Riegl VQ-580 that is especially designed for measurements of snow and ice (Riegl 2012). It uses a narrow near-infrared laser beam and a fast line scanning mechanism with a rotating mirror to measure the range between the instrument below the aircraft and the surface topography based on the principle of time of flight measurements, echo signal digitization and online waveform processing. The result is a set of linear, unidirectional and parallel scan lines. Further instrumentation specifications are given in table 6.1.

Table 3.3: Technical specifications for the Airborne Laserscanner Riegl VQ-580.

Parameter	Value
Field of View	$\pm$ 30°
Laser Beam Divergence	0.2 mrad
Angle Measurement Resolution	0.001°
Scan Speed	10 - 150 scans/second
Laser Pulse Repition Rate	50 - 380 kHz
Minimum Range	10 m
Accuracy	25 mm
Precision	25 mm
Wavelength	near infrared (1064 nm)

---

[1]More information about the IceBird campaign 2019 Winter can be found in the ICESat-2 Validation Data Acquisition Report (Hendricks et al. 2019).

The data from ALS measurements, i.e. the height of the sea ice plus snow surface above the local sea surface, lies interpolated together with GPS coordinates on a space-time grid. This is in contrast to the Laser Altimeter data, which forms a horizontal measurement line along the flight track. For comparison, the GPS coordinates for each laser altimeter measurement point were extracted and the nearest GPS point on the ALS grid with its corresponding freeboard value was written out.

4 Sea Ice Profile from Laser Data

The laser altimeter data itself does not provide the final surface profile. The following explains why and how it is determined. For this purpose, various parameterisations have been tested that have proven to be suitable for both aircraft and helicopters and are presented here.

4.1 Hibler Method

An airplane or helicopter cannot fly perfectly level and therefore laser profiles consist of low and high frequency variations. The high frequency variations are due to the roughness of the sea ice surface and are then mixed with low frequency variations triggered by the motion of the helicopter. To determine the surface profile, the flight pattern, which
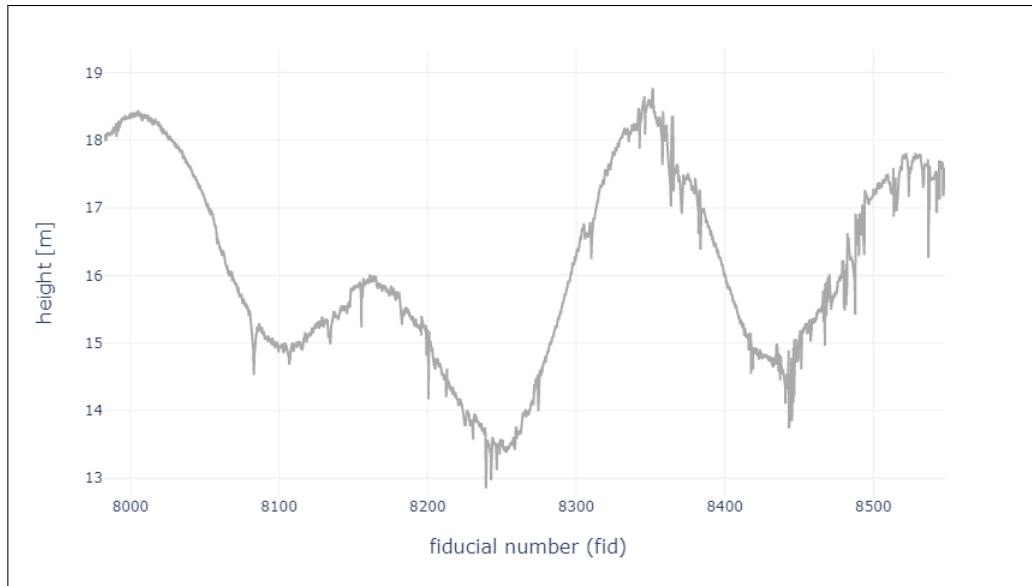

Figure 4.1: Sample of a laser altimeter profile (IceBird 2019 campaign on April 10 located in the Eastern Beaufort Sea).

is unknown, must first be subtracted. Both influences are clearly visible in the profiles. Figure 4.1. shows the measurement curve of the laser altimeter, which expresses the distance between the sensor and the ice surface. To remove the variation caused by the flight movement from the laser profiles, the data was processed using a method developed by Hibler (1972). The method includes both a high-pass and a low-pass filter. A simple high-pass filter cannot be applied here because the frequency spectra of the roughness and the helicopter motion partially overlap. This portion is significant on the scale of the surface roughness. A single high pass filter thus would remove parts from the roughness profile as well as suppress high pressure ridges.

The method after Hibler (1972) consists of three steps:

1. **Application of a high-pass filter**
   A high-pass filter only lets through wavelengths smaller or frequencies higher than the chosen cut-off value. What is left is the profile roughness with a small residual influence from the EM bird.

2. **Selection of minimum points**
   Minimum points in a defined window are selected from the filtered profile. At these points, the distance between the helicopter and the surface is the biggest and therefore, they are the lowest points on the profile. The corresponding points on the initial profile are connected with straight-line segments.

3. **Application of a low-pass filter**
   At last a low-pass filter is applied to smoothen the constructed curve. Compared to the high-pass filter, the low-pass filter only lets through wavelengths higher or frequencies lower than the chosen cut-off value.

The result is a modelled aircraft or helicopter flight curve that lies above the initial profile. To derive the surface profile, the flight curve is subtracted from the laser altimeter profile. The result, as shown in figure 4.2, is the surface topography with respect to the level ice. Furthermore, since the laser altimeter measures only the distance to the surface, the profile consists of ice thickness plus snow thickness.
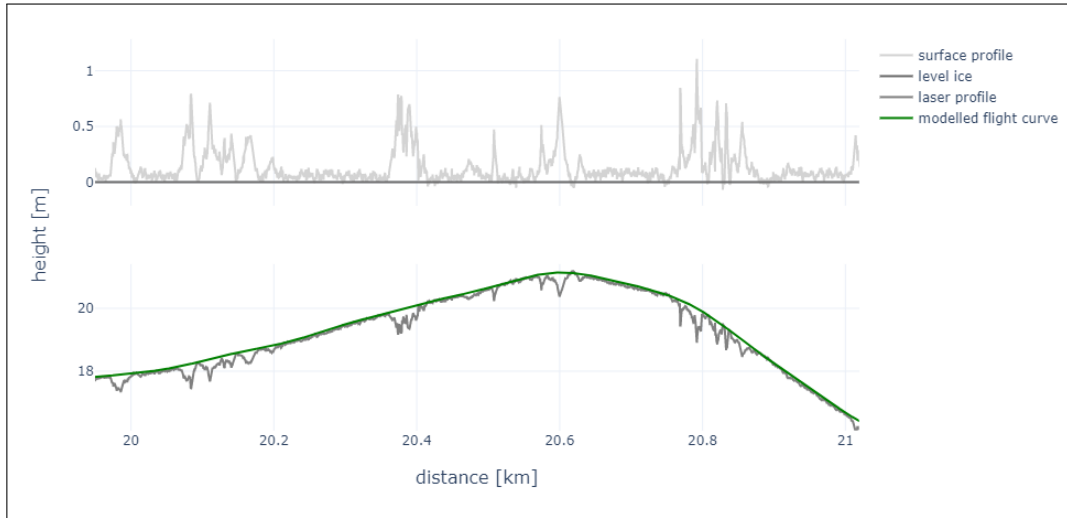
Figure 4.2: The surface profile (top) and the laser measurement together with the modeled trajectory (bottom).

4.2 Filter Parameters

The three-step filter process is implemented as a routine written in Python. For this process, the parameters λ_{hp}, λ_{lp}, step_{min} and step_{max} a are needed.

λ_{hp} and λ_{lp} are the cutoff frequencies for the high-pass and low-pass filtering in steps one and three. In high-pass filtering, λ_{hp} is the wavelength that defines the cutoff of the filter. The reciprocal of λ_{hp} is the limit of the filter, expressed as frequency. Only wavelengths less than or equal to λ_{hp}, or frequencies greater than or equal to $1/\lambda_{hp}$, will pass through the filter. In low-pass filtering, the cutoff frequency λ_{lp} is needed. Here, only wavelengths greater than or equal to λ_{lp} or frequencies less than or equal to $1/\lambda_{lp}$ pass through the filter.

A similar routine, written in C++ by Prof. Haas (AWI) and modified by Dr. von Saldern (AWI), used a wavelength of $\lambda_{hp} = 40$ m for the high pass filter and a wavelength of $\lambda_{lp} = 55$ and 35 m for the low pass filter, which changes with the helicopter. Johansson et al. (2017), who calculated the surface roughness from helicopter-borne laser altimeter measurements based on this method, used an zero-phase Butterworth filter with cut-off wavelength of 60 m for both high-pass and low-pass filtering. By contrast, Peterson et al. (2008) chose $\lambda_{hp} = 90$ m for the high-pass filtering and at another point removed variations over distances greater than 30 m (Peterson et al. 2002).

Here, different parameter values for both filters were investigated with the aim to model

the trajectory as good as possible. Figure 4.3 shows the laser profile and the curve for different wavelengths after the second processing step. The profile was high-pass filtered at different wavelengths, minimum points were identified and connected with straight line segments in the unfiltered profile. When choosing the cut-off frequency, it is important
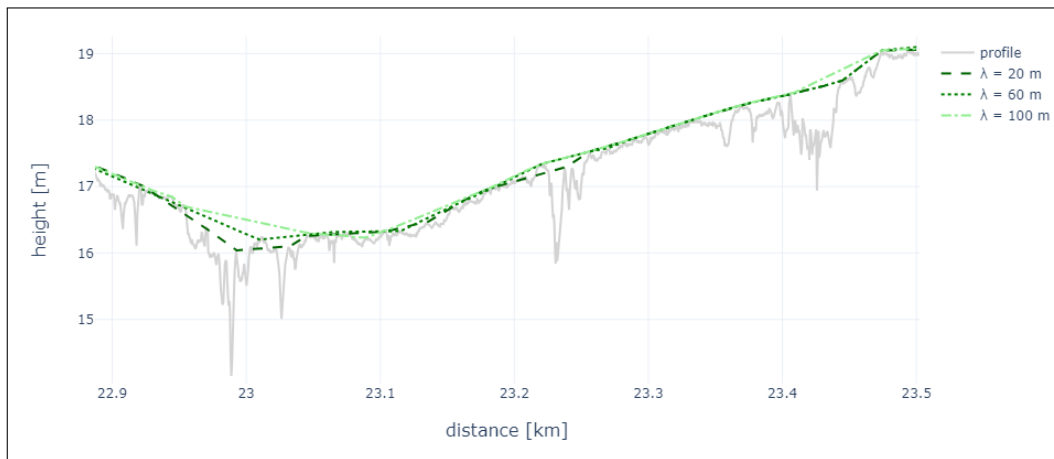

Figure 4.3: The unfiltered profile of the laser altimeter and the curves connecting the minimum points with straight segments for different high-pass filter parameters.

that not only high frequencies pass through the filter. Wavelengths shorter than 40-60 m tend to cut off the profile, resulting in an underestimation and negative surface elevations. Higher cut-off wavelengths, on the other hand, tend to give a result that does not always follow the bird's motion, ignoring small changes and overestimating the surface height. Concave profile sections are particularly affected by this. Last but not least, the width of ridges has to be taken into account when choosing the filter wavelength. The typical or maximum ridge width should pass the high-pass filter. This is important because wide ridges contribute to the overall roughness and cannot be neglected. Here, a digital Butterworth filter with a wavelength of $\lambda_{hp} = 60$ m was used for high-pass filtering. This value is well suited for most laser profiles after comparing the filter parameters. For the low-pass filter, it is only important that the curve does not deviate too much from the initial profile or the movement of the helicopter or aircraft. Here, a digital Butterworth filter with a wavelength of $\lambda_{lp} = 60$ m has proven to be most suitable. Hibler (1972) found that both parameters, λ_{hp} and λ_{lp}, affect the final result, but are not critical. However, compared to the filter cut-off values, the identification of the minimum points and hence the parameters $step_{min}$ and $step_{max}$ that define the spacing of the selected

minimum points are much more critical for the final result. According to Hibler (1972), the best approach to identify minimum points is to determine one and start from it to search for the next minimum point in a window of defined width. Thus, the window size influences the distance between the minimum points. The distance should not be too small, because then only the original profile is reproduced. On the other hand, the distance should not be too large, otherwise the result is not representative for the flight movement. To identify minimum points in the old C++ Program, a minimum window width of $step_{min} = 10$ m was chosen. The maximum window width changed with the flight campaign between $step_{max} = 80$ m for GreenICE in 2004 and 2005 and $step_{max} = 50$ m for PoleAirship. The default value was set to $step_{max} = 30$ m. A sliding window with a width of 90 m was chosen by Johansson et al. (2017) and Peterson et al. (2008) selected a window size of 22 m for flying speeds of 45 m/s to locate the minima. For this work, the approach was slightly modified. Here, the window width varies with the roughness, as exemplified in Figure 4.4. In sections with low surface roughness, the
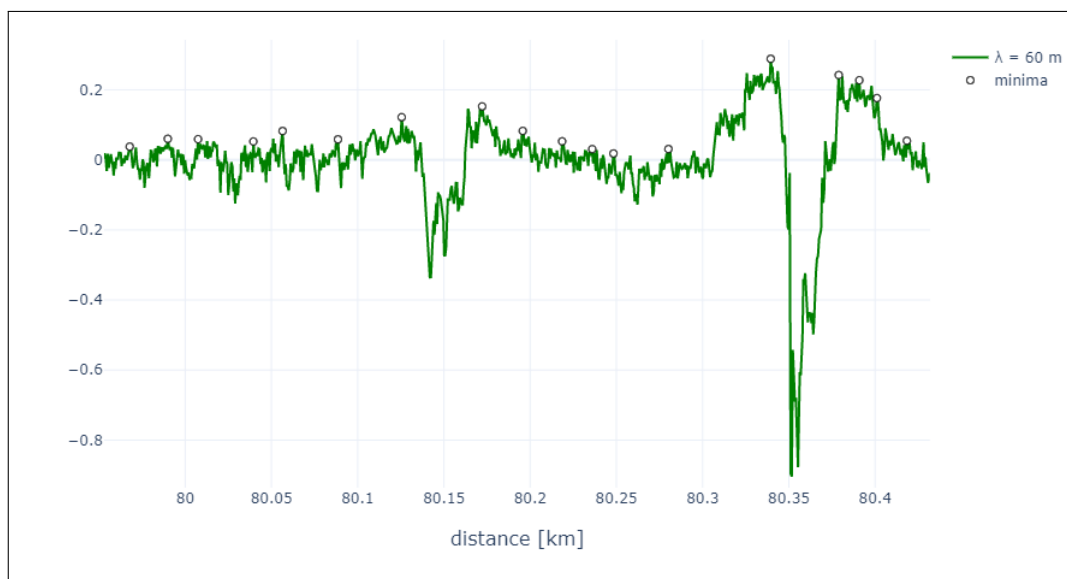
Figure 4.4: Sample of a low pass filtered profile with identified minimum points.

window is smaller than in very rough areas. This is because in highly deformed areas with broad ridges, there is often little level ice to fit the curve to. In these sections, it is important that the point spacing is large enough to find intersections with the level ice. In weakly deformed areas, on the other hand, there is a plenty of level ice to which the flight curve can be well fitted. It is therefore possible to choose a smaller spacing and

thus to resolve the motion of the EM bird more accurately. If the standard deviation between 10 and 70 meters is smaller than 0.1, minimum points in a window of 10 - 40 m are searched. If the standard deviation is smaller 0.4 the window is 10 - 70 m. And if the roughness is even higher, points are searched in a window of 10 - 100 m.

4.3 Sources of Uncertainties

This section discusses the influence of attitude changes of the EM bird, mentions laser dropouts and lists several possible sources of uncertainty that may vary in their occurrence and magnitude between profiles. They depend, for example, on the way the helicopter or aircraft is flown, or on the surface morphology. This makes it difficult to determine a general error. Castellani et al. (2014), for example, who used the same filter method to derive surface profiles from laser altimeter data, only identified topographic features higher than 0.2 m due to uncertainties in determining errors in the filter method. Inaccuracies usually concern the vertical, i.e. the height of the surface in relation to the level ice. On the horizontal scale, distance errors can occur due to variations in airspeed, which cannot be taken into account between two GPS points, corresponding to a distance of approximately 3-4 m. On the vertical scale, in addition to the inaccuracies of the measuring sensors, errors can also be caused by following:

- Sudden elevation changes that occur caused by abrupt flight changes or floe edges that can seem like pressure ridges. These features cannot be resolved by the automatically calculated minimum points.

- Highly deformed regions with little to no level ice make it difficult to fit a trajectory to level ice and are therefore particularly error-prone. There is a lack of intersections through which the curve can be fitted. As a result, the surface heights in these regions are underestimated.

- The width of some pressure ridges in the laser profile can be larger than the largest possible distance between two automatically determined minima and thus be underestimated.

- The width of pressure ridges can be overestimated if they are not flown over strictly vertically during the flight, but at an oblique angle.

- The flight curve may slightly over- or undercut the real surface profile at turning points of the flight movement, at valleys and peaks, which may result in small artificial bumps in the surface profile.

- The detection of the minimum points takes place within a defined window width. If there is an even higher point shortly before or after the window, the trajectory placed through the minimum point undercuts the surface profile and leads to negative heights.

- Different cutoff frequencies chosen by several authors for different profiles indicate that the filter parameters vary slightly for different flights.

The former program in C++ allows a manual correction after the minimum points have been identified automatically and a first trajectory is available. Saldern (2007) investigated how these manual corrections affected a selected profile. The result showed the largest differences for the mean altitude with deviations in the range of ±5.14% and a smaller range of variation of ±1% for pressure ridges. Manual adjustments mainly improve the accuracy of the average surface height and not that of the pressure ridges. The method is therefore particularly suitable for ridges.

4.3.1 Orientation of the EM bird

During the survey, the EM bird continuously experiences changes in orientation due to various forces (e.g., gravity, lift, drag, cable pull, and wind), which generate small errors (Fitterman & Yin 2004). The types of swinging motion are divided into roll, pitch and yaw. Roll is the swing across the direction of the flight around the longitudinal axis, pitch is the fore and back swing of the EM bird and yawing means a rotation around the vertical axis. These movements can be minimized by the pilot if possible, but are often unpredictable and difficult to correct in gusty weather or if the bird encounters unexpected localized winds (Holladay et al. 1997). All movements result in a lateral offset that changes the surface sampling location. Further, roll and pitch movements lead to an overestimation of the surface elevation, here also referred to as an altitude effect. These height deviations are mainly influenced by the rolling of the EM bird. If the bird's altitude is measured with a laser altimeter, the orientation-induced altitude effect at the height of the EM bird, h, is of order Δh ($Holladay\ et\ al.$ 1997).

$$\Delta h = -h/cos(pitch) \times cos(roll) \tag{4.1}$$

Most sea ice systems do not measure pitch and roll, making it difficult to correct for attitude errors. To find a typical value that can be used to account for attitude errors in this work, Multisensory Airborne Sea Ice Explorer (MAiSIE) data, recorded on 05.04.2014,

has been used (see figure 4.5). The MAiSIE-System was developed to overcome limitations associated with traditional, simple sea-ice AEM systems. It is accompanied by high-accuracy attitude sensors, sensing roll and pitch angles by the Inertial navigation system (INS) (Pfaffhuber et al. 2012).
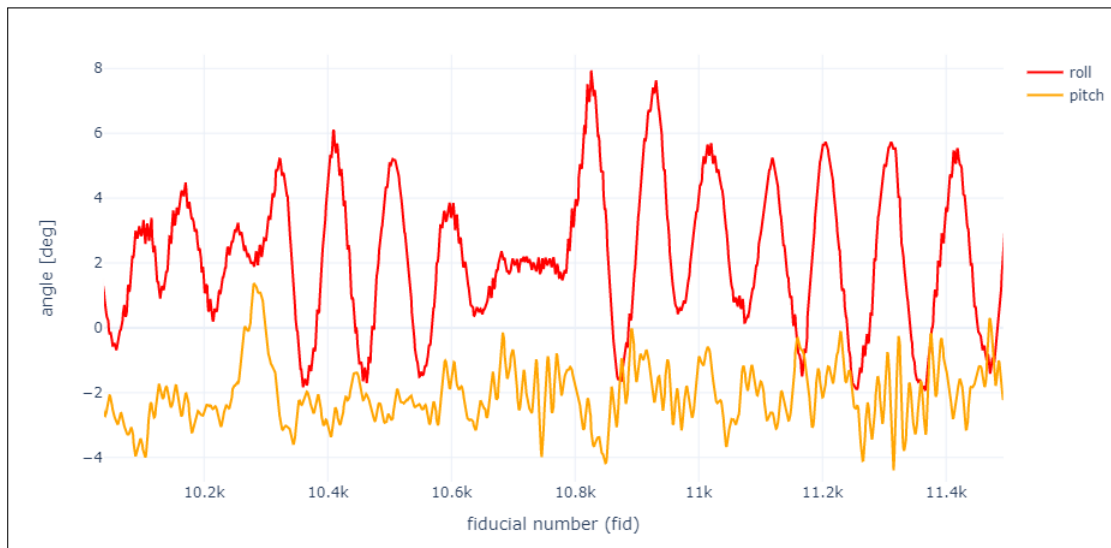
Figure 4.5: Pitch and roll angles of the EM bird from MAiSIE measurements (20140405_012425).

Errors due to roll and pitch were calculated for two flight sections for which the flight level was assumed to be 20 m. The latter is important because the magnitude of overestimation is proportional to the flight altitude. The result is a mean total error for both data sets of ± 0.037 m with a maximum total error of ± 1.01 m. Individual errors of roll and pitch are listed in table 4.1. Strong deviations, like the maximum measured roll angle of 16.58°, lead to a large overestimation, but are exceptional cases. They are most likely due to flight maneuvers. The 95% quantile for the roll angle is $\pm 6.66°(\pm 13.5$ cm) and that for the pitch angle is $\pm 3.48°(\pm 3.7$ cm). The observed flight angles are mostly smaller than 10°. At an altitude of 20 m, this corresponds to an error of 30 cm, which is considered to be representative for all flights.

Table 4.1: Average attitude angle and the resulting altitude effect.

	mean angle [°]	mean [cm]	max angle [°]	max [cm]
roll	2.85	2.5	16.58	91.8
pitch	1.98	1.2	5.37	8.8

4.3.2 Laser Dropouts

A reason for laser dropouts can be measurements over open water and melt ponds. The emitted near-infrared wavelengths cannot penetrate the water surface and thus most of its energy is absorbed by the water column or reflected (Höfle et al. 2009). Compared to snow and ice surfaces, where diffuse reflection is expected, laser energy is specularly reflected. Dropouts occur when the reflected signal is not detected by the receiver, either because it is reflected outside the field of view or because the orientation changes slightly due to movement to the EM bird. The result is a characteristically high number of laser shot dropouts and low backscatter energy over open water. The laser range dropouts are automatically filled with values of 999.99, which are easy to identify. Individual dropouts are interpolated linearly. If there are less than 5 values per GPS second, these are replaced by NaN values. One second usually contains eight to ten measured values, which corresponds to a data interval of 2.4 - 4 m with a typical point spacing of 0.3 - 0.4 m. Since changes in the profile can already be observed on smaller scales, more than seven contiguous NaN values in the profile are excluded to avoid deviations in the profile. In addition, dropouts could be observed in individual data sets of certain flights. They are individual measurements with different heights. To remove them as far as possible, measured values in the surface profile that are at least 1.5 m higher than the neighboring values on the left and right are replaced with NaN values and then linearly interpolated.

4.4 Comparison with ALS Data

In this section, two surface profiles from laser altimeter data are compared with simultaneously acquired laser scanner data. To do this, first of all it is important to point out their differences. They are the reason why the profiles will always differ by a certain amount, even with an error-free processing of the Laser Altimeter measurements.

The biggest difference is that both profiles show the sea ice surface elevation with respect to different reference heights. The profile of the laser scanner data is related to the freeboard and thus is the thickness of sea ice protruding above the water level. The laser altimeter profile, on the other hand, is referenced to level ice. This is the height of sea ice rising from the surface, which consists of undeformed ice and, if present, its snow cover. As a result the sea ice thickness of the laser scanner data is always higher than that of the laser altimeter and a comparison will show an underestimation of sea ice measured by the laser altimeter. Another reason for underlying differences in the data comes from the fact that the measurement points are geographically not exactly on top

of each other. Instead, the altimeter surface elevation of a GPS point is compared to the surface elevation of the laser scanner whose GPS point is nearest to that of the altimeter. A slight offset can result in different ice profiles, especially on deformed sea ice, where the height of the ice can vary greatly even in a small area.

Table 4.2: Key parameters of the laser altimeter profiles.

Parameter	201904101509 (A)		201904101548 (B)	
	AEM	ALS	AEM	ALS
profile length	62951.92 m		67099.16 m	
surface elevation:				
mean	0.12 m	0.19 m	0.18 m	0.38 m
median	0.07 m	0.14 m	0.10 m	0.27 m
points below zero	8.39%	0.42%	5.51%	0.68%

Profile 201904101509, hereafter referred to as A, is 63 km long, which is about 5 km shorter than profile 201904101548, referred to as B. Surface elevations in profile A are also lower than those of profile B. In addition, the comparison between altimeter and scanner show that elevations measured by an altimeter lie, as expected, below the laser scanner. The difference of the individual profile points in profile A for mean and median is 6.9 cm and for profile B, the mean difference is 19 cm while the median is 14.9 cm. The relatively high difference in profile B is due to the fact that the profile has been deformed in large parts, and these are the areas most prone to errors and underestimations of the sea ice surface. The altimeter profile A contains the largest percentage of negative surface elevations of 8.4 %. These are almost exclusively in range of 10 cm and occasionally reach 20 cm. Only in very rare cases does the surface extend further below 20 cm. In profile B, the proportion of negative surface heights is lower with 5.5 %. They are also mostly in the range of 10 cm and more rarely at 20 cm. The reason why the amount is larger in profile A is that the profile has larger areas of flat ice, so the modeled trajectory is closer to the profile. It increases the probability that individual points on the surface will be undercut. In comparison to the altimeter profiles, the proportion of negative surface heights in the laser scanner profiles is less than 1 %.

To illustrate the relationship between the altimeter and the scanner, they were plotted against each other (Figure 4.6a and 4.7a). Both profiles show a strong positive correlation. For profile A the correlation is 0.72 and for profile B it is 0.70. Since the profile heights do not match exactly, the average height within a window width of 10 m was compared as well (Figure 4.6b and 4.7b). This results in a slightly higher correlation of

0.86 for profile A and 0.81 for profile B. It also reveals a trend that seems to follow in loops. A possible reason is an offset between the profiles. This results in a slightly higher correlation of 0.86 for profile A and 0.81 for profile B. It also reveals a trend that seems to follow in loops. A possible reason is an offset between the profiles. Following this hint, one can observe a certain lag between the profiles, as in Figure 4.8, where the altimeter profile is placed in front of the laser scanner. Thus, both profiles were cross-correlated to determine how well they agree with each other and at what point the best match occurs. For profile A, the best result was obtained at an offset of 2 measurement points (1.07 m) and for profile B at 6 measurement points (3.27 m). Offsetting the profiles by this factor has a positive effect on the correlation of the data. While the correlation for profile A was previously 0.73, after correcting for lag it is 0.79. For profile B, it even increases from 0.70 to 0.84. One reason for the lag may be because of different processing speeds of the system, supplying information to the data acquisition system. This is because the internal software of the sensors needs time to process the measurements and generate a message. However, the time lag between data groups should be similar, because they are acquired from the same hardware at the same data rate. Different processing speeds and lags are therefore unlikely.
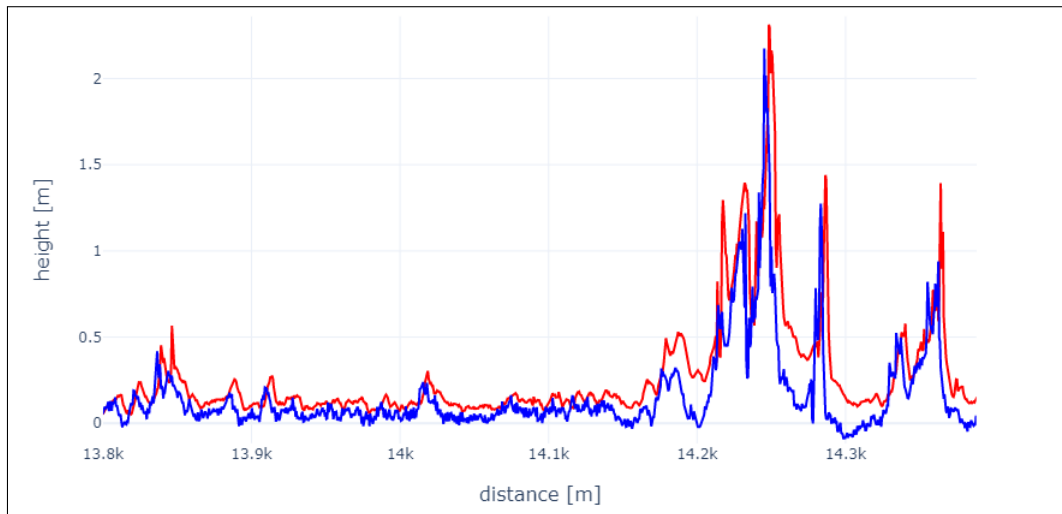
Figure 4.6: Profile 201904101548 (B) with the surface height measured by a laser altimeter (blue) and a laser scanner (red).
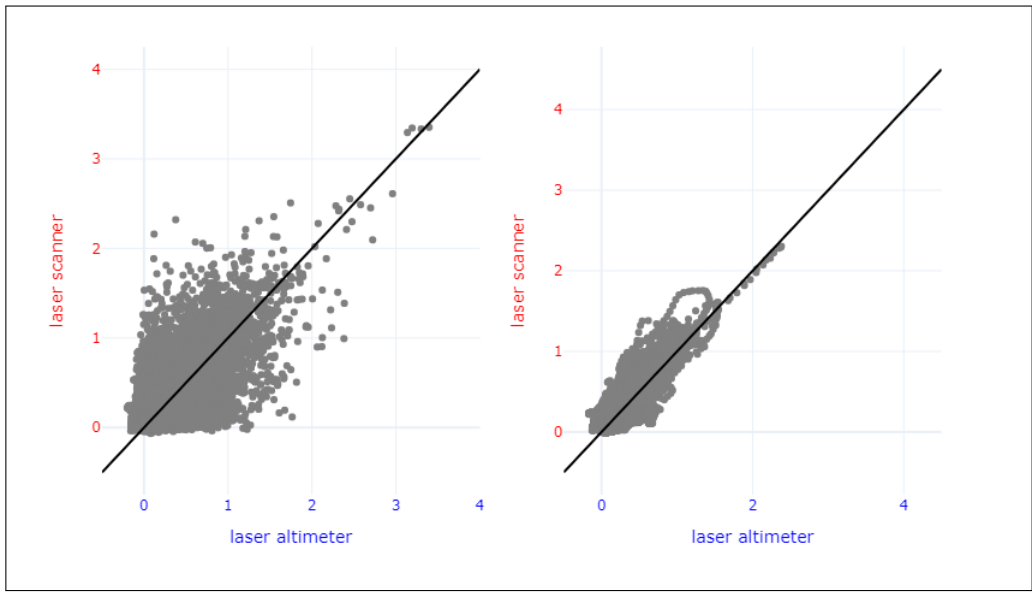
(a) correlation: 0.72

(b) mean values of 10 m window
correlation: 0.86
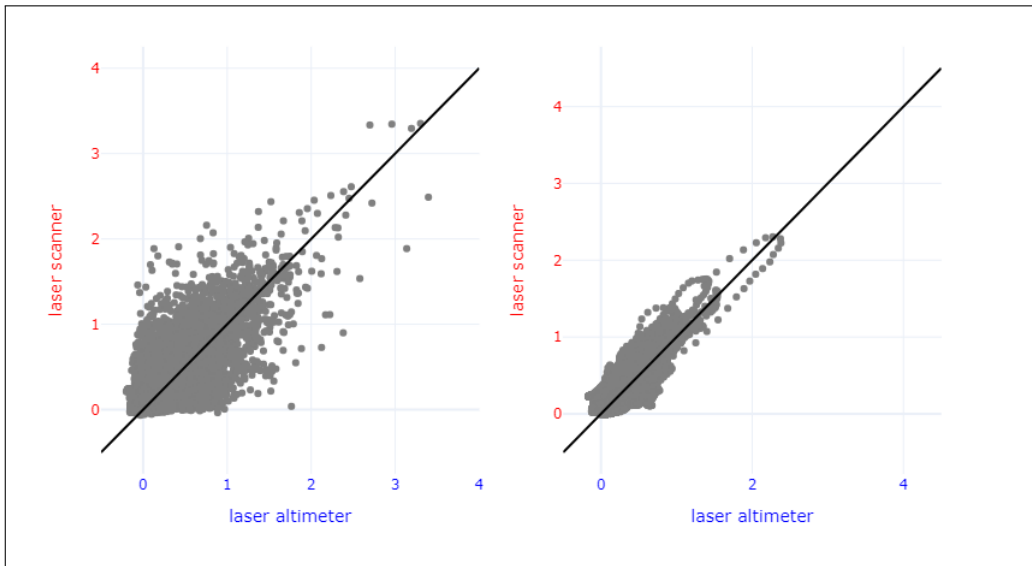
(c) cross correlation: 0.79

(d) mean values of 10 m window
cross correlation: 0.87

Figure 4.7: Scatter plots showing the correlation between laser scanner and altimeter for profile 201904101509 (A)
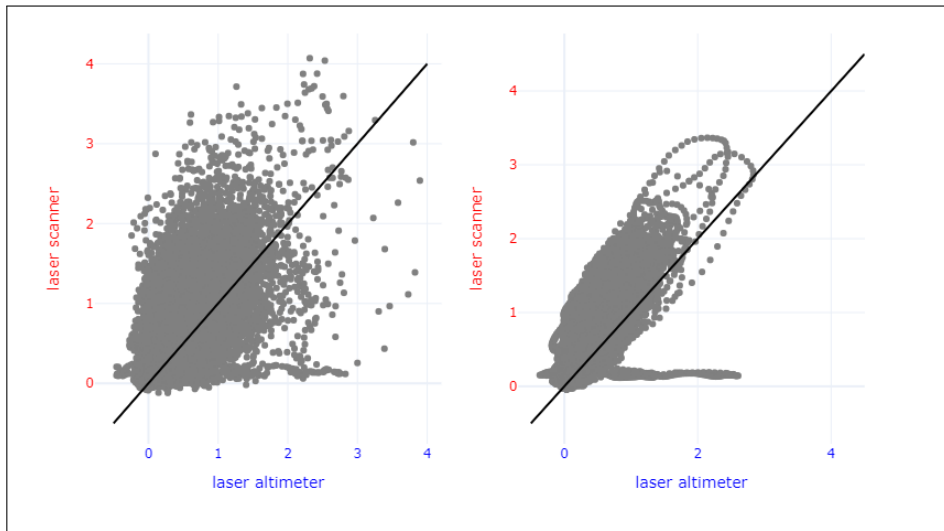
(a) correlation: 0.70　　　(b) mean values of 10 m window
correlation: 0.81
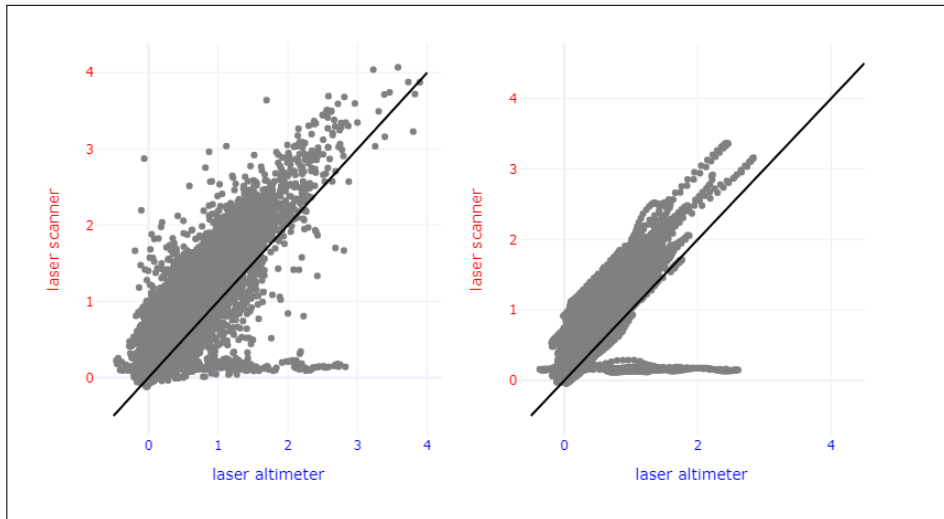
(c) cross correlation: 0.84　　(d) mean values of 10 m window
cross correlation: 0.85

Figure 4.8: Scatter plots showing the correlation between laser scanner and altimeter for profile 201904101548 (B)

In addition, the scatter plots show that the relationship between the profiles decreases with increasing profile height. This indicates that the routine works best at smaller heights or lower deformation rates. And as expected, it also can be seen that the altimeter profile height is slightly lower than that of the laser scanner. Further, a group of outliers can be observed in figure 4.7. They significantly overestimate the surface height of the

sea ice. This difference is an artifact caused by an incorrect altimeter measurement (see Figure 4.9) that cannot be corrected by the processing routine.

Figure 4.9: Artefacts in the laser altimeter measurements leads to errors in the surface profile.

Furthermore, the profiles were divided into six groups of different levels of roughness. For each point in the profile, the standard deviation in a rolling window of 10 m was calculated. If the standard deviation is less than 0.1, for example, the examined measuring point is assigned to the lowest roughness class. In addition, the average height within the window between the laser altimeter and laser scanner was compared and the difference between the two values was formed. From this it can be determined how large the height difference is for areas of different roughness levels. The results are summarized in table 4.3. It shows that profile B is rougher compared to profile A. More than 60 % of profile A is in the lowest roughness class whereas the percentage for profile B is about 50 %. In contrast, the amount of profile B is higher in all higher roughness classes. The mean height difference between the altimeter and the laser scanner profile A was lower in all roughness classes compared to B. Moreover, the height difference increases with increasing roughness for both profiles in each roughness class. For profile A it ranged from about 7 to 10 cm and for profile B it ranged from about 14 to 34 cm. The same was calculated for the profiles that were lag corrected; the correction reduced the height difference only slightly. It shows again that the accuracy of the laser height profile decreases especially in heavily deformed areas.

45

Table 4.3: The share of different roughness classes in the laser altimeter profiles and the average height difference within the classes to the laser scanner. The roughness is calculated as the mean standard deviation within a sliding window of 10 m for each point.

classes of roughness	share of the total profile	difference (time-lagged)
201904101509 (A)		
<= 0.05	63.273%	0.076
0.05 - 0.1	18.404%	0.089
0.1 - 0.15	8.179%	0.092 (0.091)
0.15 - 0.2	3.878%	0.095 (0.094)
0.2 - 0.3	3.837%	0.093 (0.089)
>= 0.3	2.408%	0.105 (0.100)
201904101548 (B)		
<= 0.05	51.793%	0.140 (0.139)
0.05 - 0.1	21.42%	0.227 (0.222)
0.1 - 0.15	9.9%	0.256 (0.251)
0.15 - 0.2	5.6%	0.286 (0.287)
0.2 - 0.3	6.3%	0.323 (0.321)
>= 0.3	4.8%	0.340 (0.350)

And lastly, the height distribution for both the laser altimeter profile and the laser scanner profile is shown in Figure 4.10. First, it can be seen that the laser profile consists in part of negative profile heights that occur when the modeled trajectory undercuts the profile. It can also be seen that all profile heights are underestimated except those between 0 and 10 cm. Some degree of underestimation is to be expected due to the difference in measurement references. This should be about the same for all bins where the underestimated heights accumulate and exceed those of the ALS measurements. The height distribution also shifts to the left at higher deformation rates of the profile, where the height of rough terrain is underestimated. This is particularly evident in histogram 4.10b, where the proportion of laser height in the 0 to 10 cm range is almost four times that of the laser scanner. In contrast, it is only slightly more than twice as high in the profile A.

The comparison shows that the method is suitable to derive sea surface heights from laser altimeter data and that realistic results can be obtained. The quality of the results suffers and the surface height is underestimated only in areas with strong deformation.
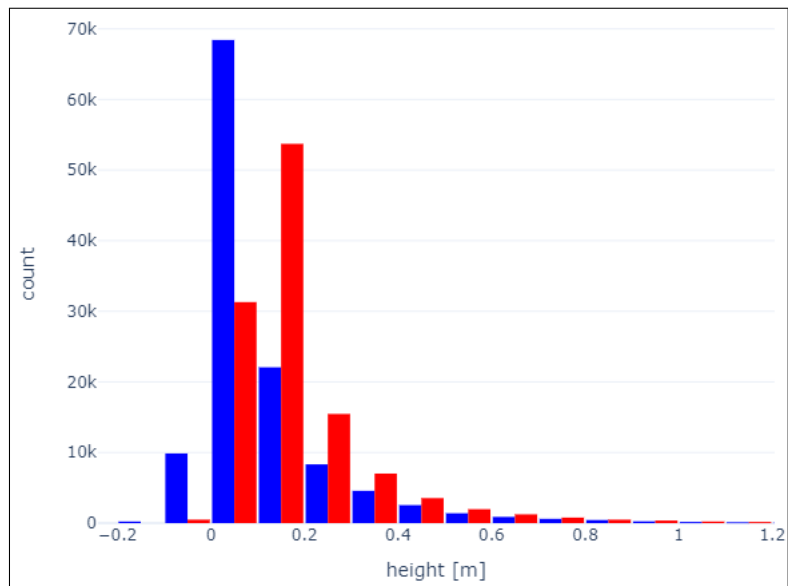
(a) Profile 201904101509 (A).
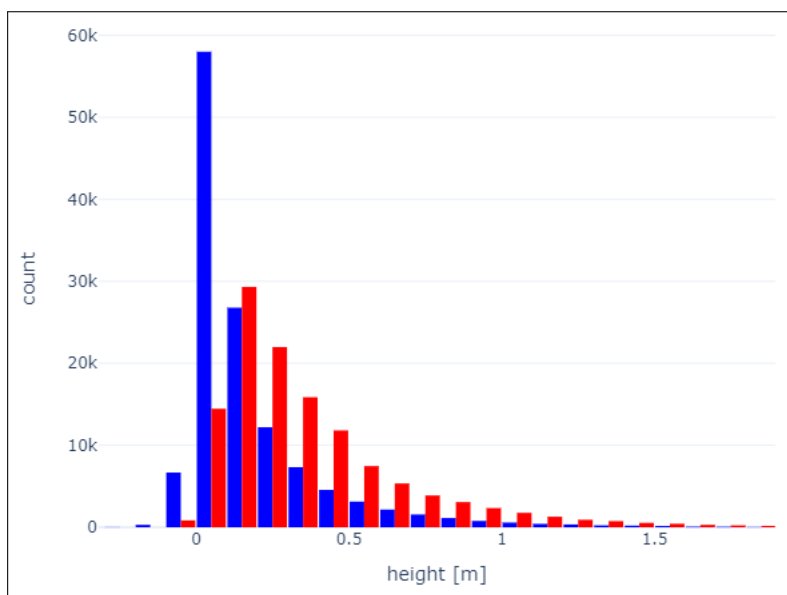
(b) Profile 201904101548 (B).

Figure 4.10: Height distribution of laser scanner (red) and laser altimeter data (blue).

47

5 Ridge Detection

For further insights of the laser surface profiles, the sails of pressure ridges are detected and characteristic information about height, width, spacing, density and intensity is extracted. The detection of pressure ridges is based on previous work as well as on the outdated C++ program and is composed of two steps, first identifying local maxima and then checking if they can be classified as a ridge.

The local maxima are automatically detected and have both a minimum height and a minimum distance to each other. The minimum height should be above the measurement uncertainty and high enough to avoid confusions with other topographic features such as snow dunes and sastrugi. At the same time, the minimum height of the maxima should be as low as possible to detect as many ridges as possible. Since the minimum height of the pressure ridges has a great influence on the amount of identified ridges, it is important to find a suitable value. Hibler et al. (1992) suggest a threshold of one meter due to the difficulties of deciding what a small ridge really is, especially in rubble fields. A similar value was chosen by Wadhams (1980b) to eliminate the small-scale roughness. A significantly lower cut-off height of 0.4 m was used by Lewis et al. (1993) to derive statistical properties in the Baltic Sea. Castellani et al. (2014), Dierking (1995) and Rabenstein et al. (2010) as well as the C++ script by Haas set it to 0.8 m, which is also the minimum height used here. In addition to the minimum height, local maxima are identified only when they are at least 10 m apart. This parameter, as in the C++ script, prevents maxima on the slopes of pressure ridges to be recognized as separate, independent formations.

Finally, each local maximum is checked according to the Rayleigh criterion (Hibler 1975, Wadhams & Horne 1980, Wadhams & Davy 1986) to determine whether or not it is a true ridge sail or part of a multi-pointed ridge. The criterion ensures that one broad, rough object is counted as one rather than multiple ones. For this purpose, the surface heights on either side of the maximum within 20 m radius are examined. Following the Rayleigh criterion, a maximum is classified as a ridge if it is at least twice as high as its troughs on both sides.
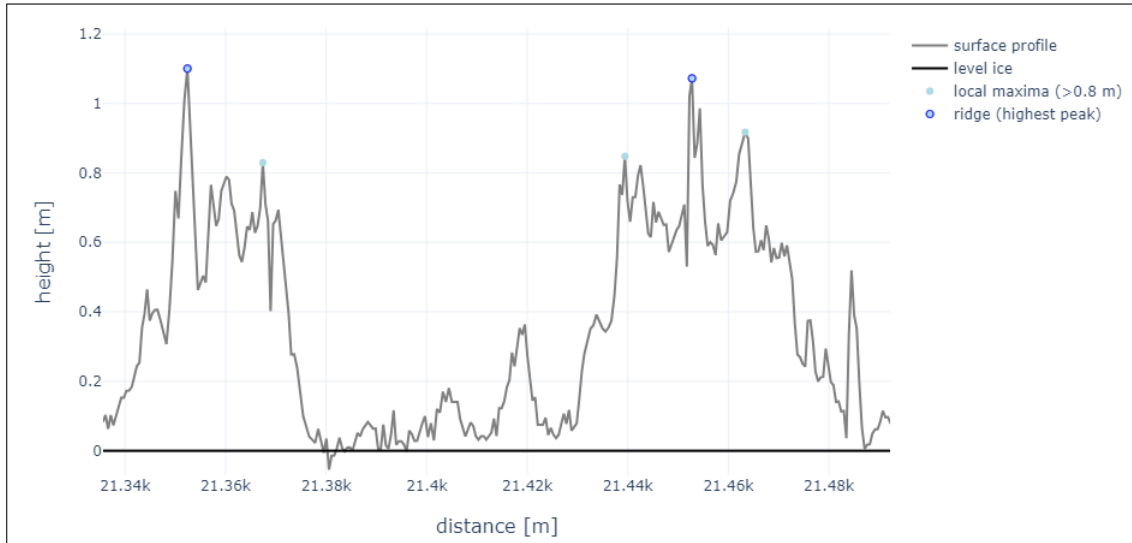
Figure 5.1: Local maxima with a minimum height of 0.8 m and a minimum spacing of 10 m and the local maxima (dark circled) that are classified as ridges according to the Rayleigh criterion.

The border of a pressure ridge is either the point that is shared by two neighbouring ridges or the point where a certain threshold, here 0.3 m, is reached. The left and right border define the width of a ridge. The spacing between ridges is the distance between the ridge borders. The threshold of 0.3 m was chosen instead of the nearest minimum of the profile to avoid unrealistic ridge widths. However, this results in an underestimation of the actual width because smaller ice blocks and boulders on both sides of the ridge are not included.

The calculation of average sail heights and spacing allows to determine the ridge density (Hibler 1975) and the ridge intensity (Lewis et al. 1993). The ridge density R_D (sometimes also ridge frequency) is the number of ridges per kilometre and can be used for a statistic characterization of pressure ridges. It is typically related to the state of ice motion (Martin 2006, Mock et al. 1972) and depends on the amount of open water in the profile (Martin 2006). However, the laser altimeter data does not allow to distinguish between open water and thin, non-deformed ice. Therefore, the amount of open water in the profile cannot be accounted for. This has an effect on the ridge spacing and density. Profiles with a larger amount of open water have a lower ridge density than profiles from areas that are completely covered with ice. The ridge intensity, R_i, is the ratio of the

average sail height $\langle h \rangle$ and the mean spacing $\langle s \rangle$.

$$R_i = \langle h \rangle / \langle s \rangle \tag{5.1}$$

Compared to density, this parameter takes into account the mean sail height. It is used in several studies as a proxy for the form drag and to classify different regimes of deformation (Arya 1973, Lewis et al. 1993, Dierking 1995, Martin 2007, Tan et al. 2012).
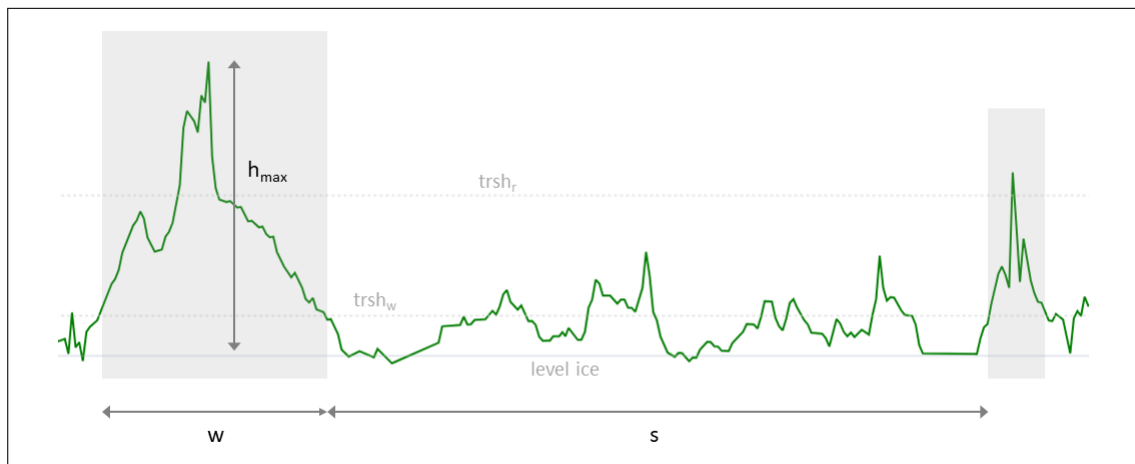
Figure 5.2: Section of a topography profile with detected pressure ridges marked in grey and their width (w), peak height (h_{max}) and distance (s). Only pressure ridges higher than a given threshold, $trsh_r$, are detected and the threshold $trsh_w$ marks the ridge boundary.

5.1 Comparison with ALS Data

Hibler described his method as particularly suitable for pressure ridges because the minimum points are often found on both sides of the ridges. Studies such as those of Weeks et al. (1971) showed that these points were often lowered slightly below the water level. How suitable the method is will be examined by comparing the altimeter profiles A and B with those from the laser scanner. To allow a comparison, a small change was made to the routine. The boundary to the left and right of the ridge is not reached when the height drops below 0.3 m, but is marked by the point where the Rayleigh criterion is met and the ridges troughs descends to a height half that of the local maximum, the highest point of the ridge. As a result, the ridges are narrower and the spacing between ridges is larger. It was necessary because the measured freeboard height of the laser

scanner varies greatly in some areas and can be well above 30 cm. Therefore, no uniform threshold could be set to determine the ridge boundary. The results of the comparison are summarized in Table 5.1.

Profile A had 246 ridges, fewer than Profile B, where 421 ridges were detected. This is partly because profile B is about 5 km longer, and partly because more deformation occurred. In addition, the number of ridges in areas of severe deformation is overestimated. In these areas, there are no tie points to the level ice, so the trajectory is adjusted to valleys and crevasses between individual ridges. As a result, it then looks like there are several individual ridges instead of one broad ridge. The number of ridges detected in both altimeter profiles is lower than for the laser scanner. This is to be expected because the altimeter surface heights are lower and therefore some ridges will be above 0.8 m in the laser scanner profile, but not in the laser altimeter profile, and only ridges above 0.8 m will be detected. In general, the number of ridges tends to be overestimated because some broad ridges are composed of several larger peaks which are recognized as individual sails. Especially difficult is the definition of individual ridges in rubble fields which may be entirely composed of randomly accumulated ice blocks. Floe edges are sometimes also recognized as ridges, which again falsely leads to an increase in the number of ridges.

Table 5.1: Comparison of ridge detection between sea ice surface profiles from laser altimeter and scanner data.

Parameter	201904101509 (A)		201904101548 (B)	
	AEM	ALS	AEM	ALS
profile length	62951.92 m		67099.16 m	
detected ridges	246	271	421	454
mean ridge height	0.80 m	0.80 m	0.90 m	1.02 m
mean highest ridge peak height	1.16 m	1.15 m	1.31 m	1.50 m
maximum ridge height	3.30 m	3.35 m	3.90 m	4.07 m
mean ridge width	3.97 m	5.2 m	6.87 m	10.72 m
maximum ridge width	19.83 m	31.17 m	27.56 m	39.56 m
mean ridge spacing	295.86 m	267.50 m	170.96 m	154.44 m
ridge density (nr/km)	3.91	4.30	6.27	6.77
ridge intensity (height/spacing)	0.0030	0.0027	0.0066	0.0053

The mean height of the ridges, as well as their highest peak on average and the maximum ridge of profile A differ only slightly, if at all between the altimeter and scanner. The difference for profile B is slightly higher by around 10 cm. The mean ridge heights were in the range of 0.8 to 1 m, with the highest peaks averaging between 1.15 and 1.50 m

and the tallest ridges of all profiles were found to be above 3 m. A larger difference, on the other hand, can be seen in the ridge width, both between the altimeter profiles with the largest differences for profile B and between altimeter and scanner profiles. The difference is particularly large for the maximum ridge widths, which are clearly under-estimated in the laser altimeter profile. It can also generally be questioned whether the actual width of pressure ridges can be reliably derived from the data, since the angle at which the ridge is overflown is not known. Further, the comparison of ridge spacing shows an inverse relationship with the number of ridges. It is highest for profile A of the altimeter, which has the lowest number of ridges. The relationship with the number of detected ridges is also reflected in the ridge density. Accordingly, profile A has the lowest ridge density.

6 Sea Ice Surface Roughness

Between the first freezing and the final melt surface-atmosphere interactions, sea ice motion, and melt processes alter the surface roughness. The roughness can be seen as the topographic expression of the sea ice surface or as a short wavelength fluctuation with local maxima and minima at different amplitudes and distances. The roughness of the sea ice surface is spatially and temporal highly variable throughout the entire Arctic. It changes with the frequency of storm events, where the amount of deformed sea ice increases with the storm activity (Castellani et al. 2014). In addition, it is linked to different sea-ice regimes. First-year ice tends to contain less pressure ridges than multi-year ice and is usually thinner and smoother (Saldern et al. 2006). There is also likely a difference in surface roughness between summer and winter. Seasonal snow deposition during the winter can smoothen the surface, whereas wind erosion and redeposition of snow creates topography in the form of sastrugi and snow dunes (Fassnacht et al. 2009, Déry & Tremblay 2004). And the melt of the ice during the summer leads to a smoothing of the surfaces and the formation of melt ponds.

On a large scale, the surface roughness is mainly influenced by structures such as pressure ridges and thus can be quantified by the mean ridge height, mean ridge spacing, and ridge density as well as intensity (Hibler 1972, Wadhams 1980a, Dierking 1995). However, the roughness of small scales caused by snow accumulation and melt processes is an important factor as well. Castellani et al. (2014), for example, showed that a characterization of surface roughness only by large pressure ridges is not accurate enough to measure its impact on the surface drag. An increase in small topographic features found to have a significant effect on the form drag, and in some cases was even higher than the contribution of larger structures such as pressure ridges. The minimum horizontal scale on which the roughness can be analysed by a laser altimeter is limited by the measurement resolution of 0.3-0.4 m.

There are two approaches for quantifying the surface roughness (Shepard et al. 2001). The first approach assumes a stationary surface, where statistical properties do not change over different measurement scales. The second approach is based on physically measuring the topography of different surfaces without a priori assumptions and creating realistic

quantitative characterization of natural terrain. Sayles & Thomas (1978) have shown that natural surfaces are poorly described by stationary random processes. Instead, natural surfaces tends to exhibit power-law behavior. This means a sample with a finite length from a surface, i.e. sea ice, will never completely represent its properties. The length of profiles is also important because, on the one hand, shorter profiles consist of fewer points and are therefore more influenced by statistical errors and are generally more homogeneous with respect too their surface characteristics (Saldern et al. 2004). On the other hand, long profiles can only poorly distinguish between smaller surface features such as leads or ice floes due to averaging and can contain multiple roughness regimes. There is currently no standard method to characterize the surface roughness of sea ice. Most frequently used are the roughness parameters mean elevation, RMS height and autocorrelation length (Saldern et al. 2006). Parameters presented here, which describe the distribution of profile heights, are mean elevation, standard deviation of the profile elevation about the mean (RMS height), skewness and kurtosis. These would, under the assumption that the sea ice surface is formed by stationary random processes, take constant values and can characterize the surface regardless of its profile length (Saldern et al. 2006). But this is not the case; therefore the length should be considered for a direct comparison of the roughness parameters between different profiles. This is why Saldern et al. (2004) has divided the profiles to be studied for a comparison and the calculation of roughness parameters into 2 km sections. Parameters that are suitable to describe non-stationary profiles are the RMS slope and the fractal dimension.

6.1 Statistical Parameters

Mean Surface Height (R_a)

R_a is the arithmetic mean roughness value from the heights of all profile points, used by authors such as Saldern et al. (2006, 2004), Lewis et al. (1993), Goff et al. (1995) for the description of sea ice. It is determined as

$$R_a = \frac{1}{n} \sum_n^{i=1} z(x_i) \tag{6.1}$$

where n is the number of sample points and $z(x_i)$ is the surface height at point x_i (Shepard et al. 2001).

RMS Height (R_q)

The root mean square (RMS) height, or the standard deviation of the profile surface elevation about the mean, is one of the most commonly reported parameters (Saldern et al. 2006, 2004, Goff et al. 1995, Lange et al. 2019, Fors et al. 2016, Lewis et al. 1993, Manninen 1997) and simple to obtain. Together with the mean elevation R_a, it is a measure of the relative deviation of the profile from the mean line. It is calculated as

$$R_q = \sqrt{\frac{1}{n}\sum_{n}^{i=1}(z(x_i) - \bar{z})^2} \tag{6.2}$$

where $\bar{z}$ is the mean height of the profile (Shepard et al. 2001). Furthermore, the ratio of the RMS height and the mean height, also called coefficient of variation, can be an indicator of deformation processes (Goff et al. 1995, Key & McLaren 1991). A high ratio indicates that most ice thickening occurred through the emergence of topography, whereas a small ratio would mean that it primarily occurred due to a mass accumulation by precipitation above and a freeze beneath the ice (Goff et al. 1995).

Skewness (R_{sk})

The profile can also be described by the skewness (Saldern et al. 2006, 2004, Goff et al. 1995, Lewis et al. 1993, Peterson et al. 2002), the third central moment of a distribution. The parameter is used to describe the shape of a distribution and is a measure of its symmetry around the mean. It is calculated as

$$R_{sk} = \frac{1}{n}\Sigma_{i=1}^{n}[\frac{z(x_i) - \mu}{\sigma}]^3 \tag{6.3}$$

with respect to the mean line from the arithmetic mean μ and the standard deviation σ (Sachs 2004). It is useful to observe a general trend in peaks or valleys of the amplitude (Magsipoc et al. 2020). In the case of a positive skewness, the distribution is right skewed, meaning it is steep to the left where the majority of the distribution can be found. The smaller part lies in the longer tail on the right towards higher values. Conversely, if it is negative then it is steep to the right. For the sea ice surface profile, a high skew is an indicator of more isolated, separate features, such as ridges, extending above the background topography. Contrary and with regard to ridges, a lower skew indicates to a background topography that is similar to the size of ridges. The reason could be smaller ridges, larger background topography, or a high density of ridges (Goff

et al. 1995).
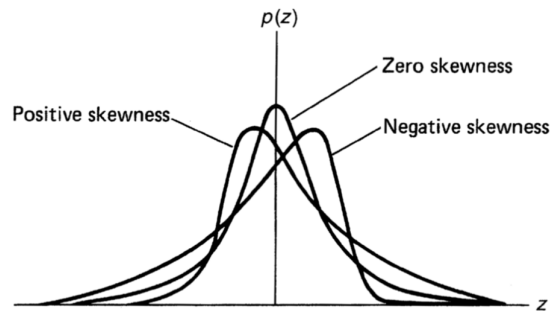
Figure 6.1: Probability density functions for random distributions with different skewness (Bhushan 2000)

Kurtosis (R_{ku})

Similar to the skewness, the kurtosis describes the shape of the probability distribution and is the fourth central moment of a distribution. It is the measure of the flatness of a distribution or the measure of dispersion around the arithmetic mean μ and the standard deviation σ and describes the position of the maximum in comparison to the normal distribution. The kurtosis is calculated as

$$R_{ku} = \frac{1}{n}\Sigma_{i=1}^{n}\left[\frac{z(x_i) - \mu}{\sigma}\right]^4 - 3 \tag{6.4}$$

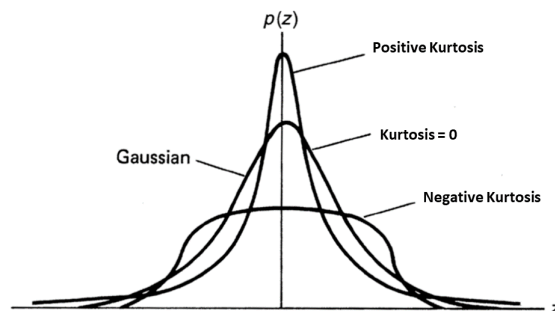
Figure 6.2: Probability density functions for symmetrical distributions (zero skewness) with different kurtosis (Bhushan 2000)

A positive value for the kurtosis is found in a distribution with high peakedness that is steeper than the normal distribution and a maximum that is higher within the same variance. This leptokurtic distribution means a strong curvature, scarcely occupied flanks and an excess of values near the mean. A distribution with negative kurtosis, also called platykurtic, is flatter with a maximum that is lower compared to the normal distribution and characterized by a negative value. For the ice profile this means that a distribution with positive kurtosis contains more high features (Saldern et al. 2004, 2006).

Autocorrelation Length (L)

The autocorrelation function of a profile is another widely used parameter (Goff et al. 1995, Lewis et al. 1993, Rothrock & Thorndike 1980, Manninen 1997) to describe the sea ice surface roughness and is the normalized covariance between the profile and itself with an offset τ. The function is a measure in how far points that are separated by a certain distance τ along the profile are similar or to which extend they influence one another. When the distance is zero, the function thus is equal to 1.0. The independence of two points is achieved for a shift τ at which the autocorrelation function is around zero.

The autocorrelation length is defined as the length where two points become statistically independent and is the distance required to reduce the correlation value to 10 % or $1/e$ (Magsipoc et al. 2020, Shepard et al. 2001). Therefore smoother surface profiles usually have a larger autocorrelation length than rougher surfaces. However, non-stationary profiles can not properly be described by the autocorrelation function (Magsipoc et al. 2020, Saldern et al. 2006, Thomas 1981). This is because, unlike stationary profiles, the correlation length depends not only on the displacement of τ, but also on the individual profile points. For profiles like the sea ice surface, this means that the correlation length does not assume a constant value, but varies for different profile lengths. A direct comparison of the autocorrelation length for quantitative statements of profiles with different lengths is thus imprecise. Therefore this parameter was not included into the routine analysis of the sea ice roughness.

RMS Slope ($\theta(\Delta x)$)

Another common roughness parameter is the RMS slope, s_{rms} (Saldern et al. 2006, Sayles & Thomas 1978), which measures the slope between profile points with a certain distance Δx. To calculate it, the RMS deviation (or Allan deviation) $v(\Delta x)$ is calculated first and then divided by the step size Δx. The RMS deviation is the RMS difference in height between points separated by the distance Δx. Both the RMS deviation and the RMS

slope are a function of the scale and are independent of the profile length. The RMS therefore can be used for a comparison of non-stationary profiles.

$$s_{rms} = \frac{v(\Delta x)}{\Delta x} = \frac{\sqrt{\frac{1}{n}\Sigma_{i=1}^{n}[z(x_i + \Delta x) - z(x_i)]^2}}{\Delta x} \tag{6.5}$$

The RMS deviation and slope can be computed at the sample interval, i.e., for two adjacent points and is convenient for investigating the smallest scales of roughness (Shepard et al. 2001). Further, it is common to report the RMS slope in degrees, $\theta(\Delta x)$, where $\theta(\Delta x) = tan^{-1}(s_{rms})$. It represents the distribution of the maximum tilt at each point, i.e. the gradient of the topographic contours.

Fractal Dimension (D)

Furthermore, a description of the profile by its fractal properties is suitable for non-stationary profiles and when the scale dependence of the surface roughness is to be taken into account. For that, the fractal dimension, D, is an often used parameter to describe sea ice (cf. Saldern et al. (2006, 2004), Goff et al. (1995), Bishop & Chellis (1989), Key & McLaren (1991), Rothrock & Thorndike (1980), Manninen (1997)).

Fractals are shapes that have self-similar details at all scales, i.e., independent of any scale. As magnification increases, more and more detail becomes visible, which can be viewed as a reduced image of the whole. On natural surfaces, such as sea ice, these details are not strictly self-similar. Instead the details are only statistically similar to those of the original section. Sea ice exhibits fractals in the sense that it consist of level ice areas and areas of deformed ice with ridges, which in turn consist of smaller level ice areas and ridges. To describe the scaling behaviour of a profile, the Hurst exponent H (or Hausdorff dimension) can be used (Shepard et al. 2001, Magsipoc et al. 2020). It is estimated by examining how the roughness, here expressed as the RMS deviation $v(\Delta x)$, changes for different horizontal scales Δx. The deviation increases with the step size Δ and follows a power law trend

$$v(\Delta x) = v_0(\Delta x)^{2H} \tag{6.6}$$

with the Hurst exponent, H, as a scaling parameter (Shepard et al. 2001).

For natural surfaces, however, the power law behavior does not hold at infinitely small or large scales. Surfaces do not become infinitely rough at smaller scales, nor do they roughen to infinitely large scales. On sea ice, the lower limit is either the particle size of which the surface consist or, as in this case, the measurement resolution. The upper limit

is determined by the distribution of large-scale features such as the height and spacing of the ridges. Furthermore, sea ice is smooth on large scales. Therefore, roughness increases slower on the vertical scale than the horizontal scale on which it is measured ($0 < H < 1$). It means both axes must be scaled differently to obtain a statistically similar form. Such profiles, which are invariant against anisotropic scale transformations, are called *self-affine*. And lastly, because the physical processes that shape the sea ice surface occur at different scales, such as ridging on a large scale and erosion and freezing on smaller scales, the exponent H cannot be assumed to be constant at all scales. Instead, the fractal properties and the Hurst exponent change at different ranges of scales (Goff et al. 1995).

To obtain the Hurst exponent, the RMS deviation for different scales is plotted as a function of horizontal distance on a log-log scale and taken from the slope of the least squares regression line. A good linear fit is given when the correlation is greater than
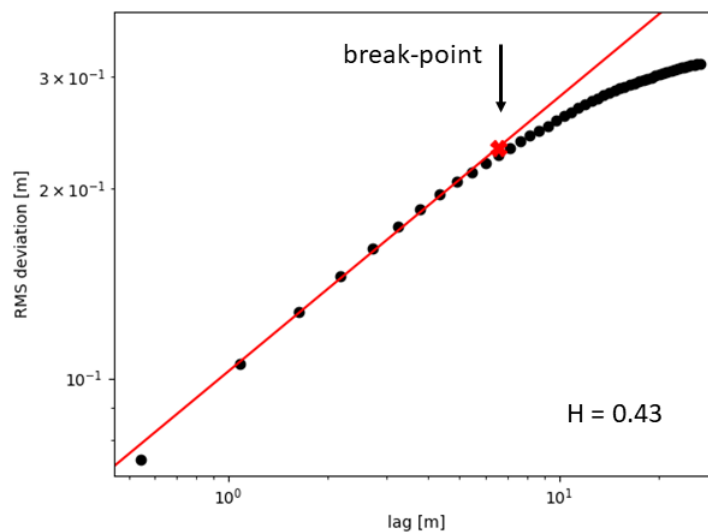
Figure 6.3: The RMS deviation as a function of the horizontal distance. The surface exhibits one power law from the smallest scale up to a break point (6.45 m) and eventually follows a different power law. The red curve is the regression line with a slope of H = 0.43.

0.95 (Shepard et al. 2001). The line is measured from the smallest scale to a horizontal scale where it appears to break and obey a different power law. Key & McLaren (1991), who studied the fractal dimension of the sea ice underside, found a difference in H between scales and related this to various physical processes that influence the surface.

Therefore, the break point can offer implications on the external processes that influence the surface roughness of ice profiles. To determine the break point, a linear regression is first calculated from three profile points. As long as the goodness of fit $R^2 >= 0.95$, this is repeated with one more data point. The break point is the point at which this is no longer fulfilled.

For self-affine two dimensional profiles the Hurst exponent is related to the fractal dimension, D, by

$$D = 2 - H \tag{6.7}$$

(Shepard et al. 2001). An increase of the fractal dimension represents and decrease in the roughness of the sea ice surface.

6.2 Comparison with ALS Data

The above parameters, with the exception of the correlation length, are calculated and compared for both the laser altimeter and laser scanner profiles. The results are shown in Table 6.1. A direct comparison between the altimeter and the scanner data is possible since they have the same length for profiles A and B, respectively. In addition, the mean height, RMS height, skewness and kurtosis parameters were calculated for 2 km long sections of the profiles (see Figure 6.4 and 6.5).

The statistical parameters show that the roughness between both flight sections is the highest in profile B. For both sections, A and B, the roughness of the laser altimeter surface profiles is lower compared to that of the laser scanner profiles. A difference between the two measurement methods is evident for all roughness parameters except for the RMS slope, and is the greatest for the rougher profile B. The RMS slope for the smallest point spacing differs only slightly, if at all, between the flight sections and the measurement methods and is therefore not suitable for a comparison of the surface profiles. Better suited is the RMS slope calculated for distances of 3 m. Here the difference between profile A and B is clearly visible. It amounts to 9°. The difference between the measurement methods is smaller and amounts to 2-3°. Skewness and kurtosis are lower in profile B, although the ice in this profile was more affected by deformation. This is due to high ridge density, and because the elevation of the background topography is similar to that of pressure ridges. Therefore, the right skewness and peakedness is less pronounced than in profile A. The calculated values of the fractal dimension can be aligned with the characteristics of the profile as well. The breakpoint, on the other hand,

varies more strongly and shows fractal behavior for the laser scanner profiles only up to scales smaller than those of the smoother laser altimeter profiles. This contradicts the expected result. For this reason, both the breakpoint and the fractal dimension cannot be reliably calculated here.

Table 6.1: Statistical roughness parameters for laser altimeter and scanner sea ice surface profiles.

Parameter		201904101509 (A)		201904101548 (B)	
		AEM	ALS	AEM	ALS
R_a	Mean Height	0.12 m	0.19 m	0.19 m	0.38 m
R_q	RMS Height	0.20 m	0.25 m	0.32 m	0.51 m
R_{sk}	Skewness	3.94	3.77	3.39	2.35
R_{ku}	Kurtosis	27.25	24.61	18.05	8.95
θ(minimum resolution)	RMS slope	0.025°	0.021°	0.025°	0.022°
θ(3 m)	RMS slope	0.045°	0.043°	0.054°	0.052°
D	Fractal Dimension	1.65	1.5	1.57	1.45
	Break Point	3.76 m	2.15 m	6.45 m	2.68 m

A scattering of the roughness parameters for the individual 2-km profile sections can be seen in Figures 6.4 and 6.5. For the parameters mean height and RMS height, the scatter is particularly large in the rougher profile B, especially when measured with the laser scanner. A strong scatter can also be seen for the parameters skewness and kurtosis. Here it is particularly large in profile A. This is in agreement with the higher deformation in certain areas of profile B and with a higher topography of the laser scanner profile in some places due to the measurement with reference to the freeboard instead of level ice. The kurtosis partially shows a very strong scattering between different profile sections. This is the reason why the mean kurtosis, as listed in table 6.1, varies considerably in contrast to its median. Thus, the kurtosis is less suitable for a profile comparison than the skewness. Overall, the comparison shows that the surface roughness of profiles A and B can best be described by the parameters mean height, RMS height as well as their skewness.

Figure 6.4: Mean height, R_a, and RMS height, R_q, for 2 km sections of profile A (a, c) and profile B (b, d) measured with a laser altimeter (AEM, blue) and laser scanner (ALS, red).

(a)   (b)

(c)   (d)

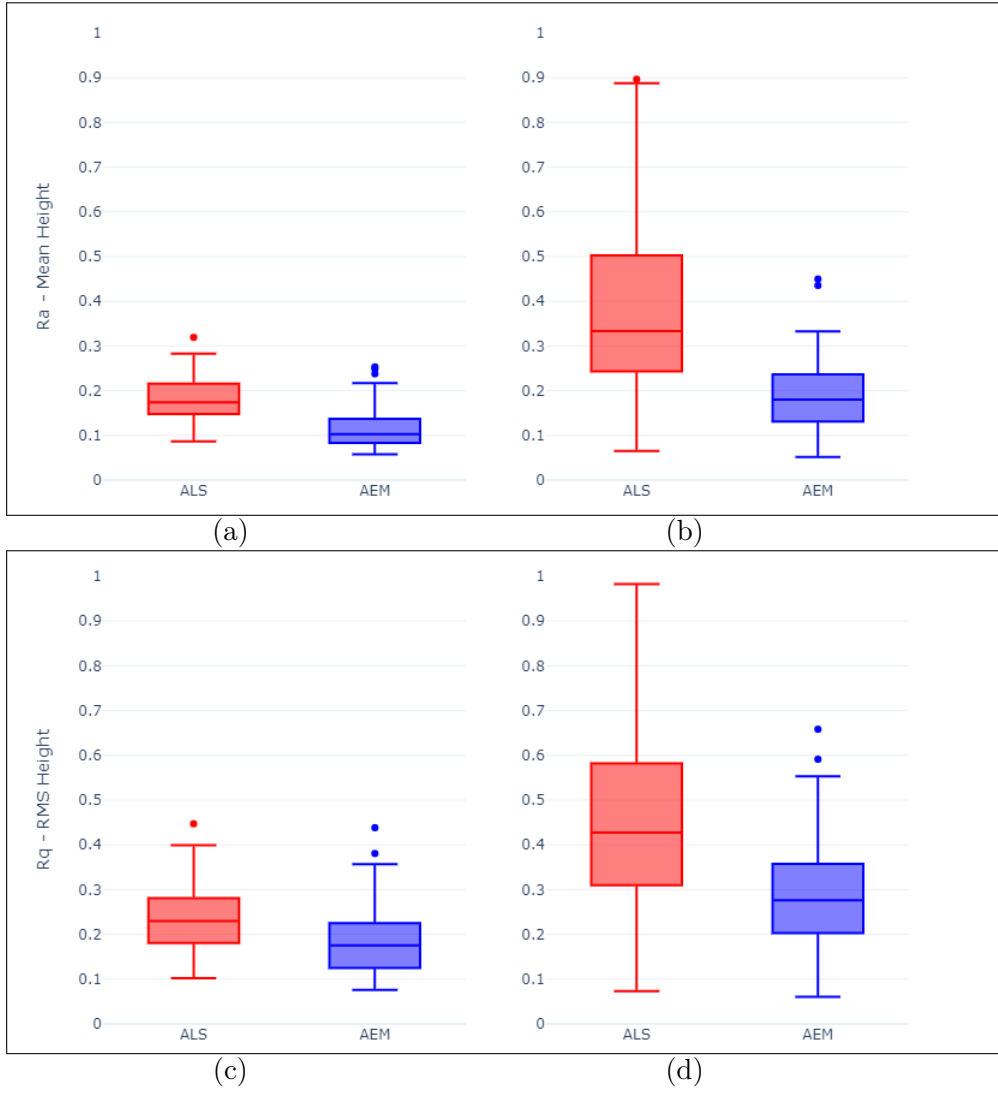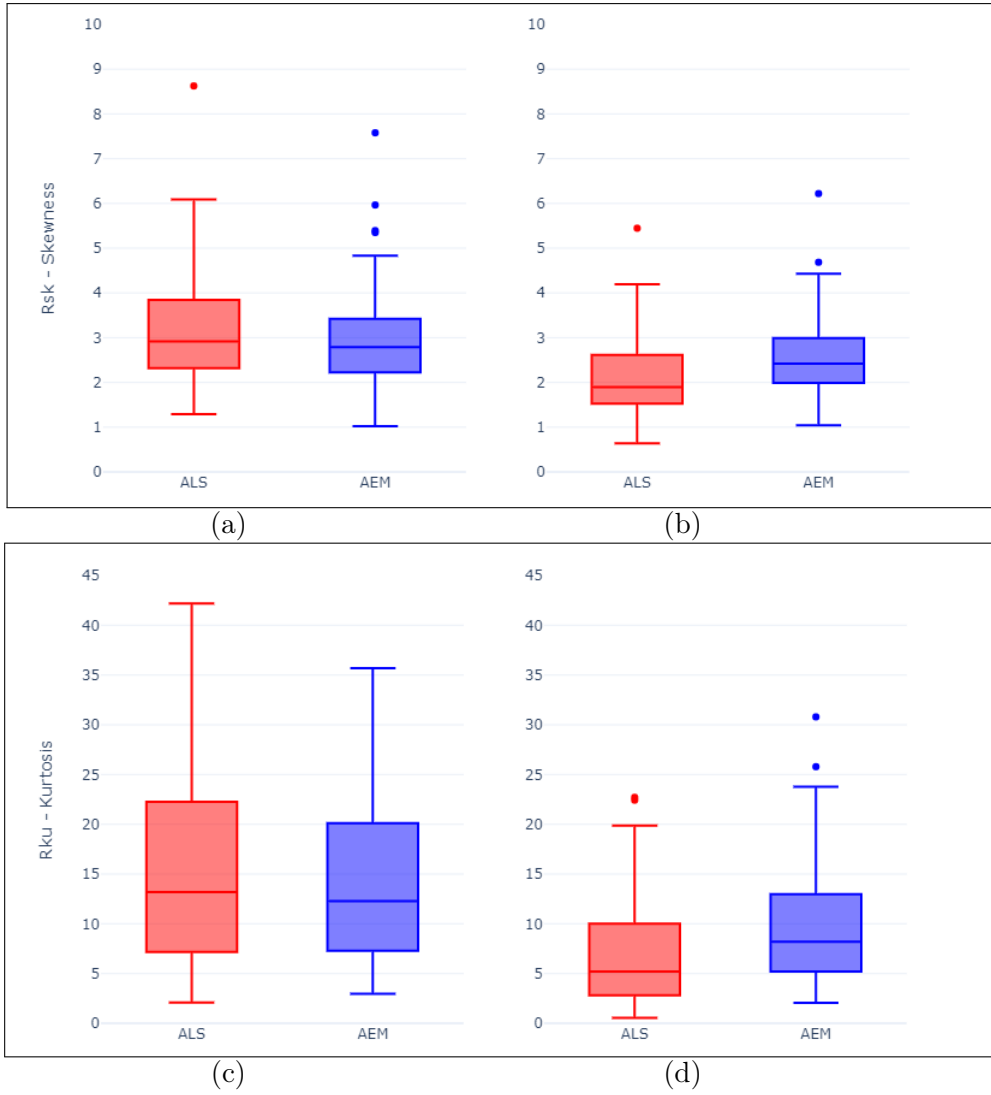Figure 6.5: Skewness, R_{sk}, and kurtosis, R_{ku}, for 2 km sections of profile A (a, c) and profile B (b, d) measured with a laser altimeter (AEM, blue) and laser scanner (ALS, red).

7 Summary and Conclusion

Sea ice in the Arctic can be found in remote locations that are usually difficult to access. One way of studying the sea ice over large areas is by airborne measurements with helicopters and airplanes. They are the platform for various instruments, including a laser altimeter, which measures the distance to the sea ice surface. This study gives an opportunity for the future to routinely investigate airborne measurements with a laser altimeter. It provides the surface profile with respect to level ice, detects ridges, and describes the surface roughness.

The following is a summarised list of the sea ice surface parameters that can be determined by means of the processing routine. A comparison with laser scanner measurements as well as visual knowledge of the results from other profiles provides an insight into the quality of the results and possible limitations. However, due to the great diversity of data, both in terms of sea ice surface and flights, and because a ground truth is not available, absolute error values could not be defined.

The surface elevation is the height of the sea ice surface relative to the level ice, i.e. the heights that rise from the surface of ice and snow. It is calculated from the difference between the measured height of the laser altimeter above the surface and the modelled trajectory of the helicopter or aircraft that pulls the laser altimeter over the surface.

The trajectory is modelled in three steps, consisting of a high and low pass filter and the search for tie points to the level ice. For the high-pass and low-pass filtering the cut-off wavelength of 60 m was chosen. Both filters were relatively insensitive to small adjustments of the filter parameter. Here, it is important to find a compromise that allows for smaller changes in the flight motion to be resolved, while avoiding an underestimation of the profile height, especially in rough areas. In addition, to model the trajectory, points on the level ice are searched within a certain window width. The best results were obtained for window widths between 10 and 100 m, depending on the surface roughness. In less deformed areas, smaller window widths can be chosen, which allow the resolution of smaller flight

manoeuvres, as there are many contact points with the level ice. In contrast, in highly deformed areas, there is little level ice, so larger window widths have to be chosen.

The greatest deviations can be found in these deformed areas. This is because the method depends on identifying tie points on the level ice to use them as reference. A certain amount of level ice in the profile is therefore necessary for a good result. If this is not given, minimum points are determined that are slightly elevated compared to the actual level ice, which results in an underestimation of surface heights. A comparison with laser scanner data showed a mean difference in the most deformed areas of up to 0.3 m. Further, an altitude effect caused by varying attitude angles of the measuring instrument during the flight can be expected. It leads to an overestimation of the surface elevation. Usually, the changes are less than 10° and therefore at altitudes of 20 m an offset of 0.3 m should be taken into account. The smallest effect observed in MAiSIE INS data was ±0.037 m and reached up to ±1.01 m in exceptional cases. An additional error is caused by the measuring device and ranges between a few centimeters. For the Riegl LD90-3100HS altimeter, used by the AWI until 2018, the accuracy is ±1.5 cm and in the worst case ±5 cm. The subsequent Jenoptik LDM301 measures the distance with an accuracy of up to ±6 cm. Overall, the comparison with ALS showed a good agreement of the data. The profile properties agree well with those of the laser scanner.

When analysing the processed data, it is important to be aware of the fact that measurements over open water will be treated as level ice because the routine is not able to distinguish them. A confident investigation of surface features is recommended starting from a height of approximately 0.3 m. This is due to the nature of the laser height data and small deviations originating from the modelled flight trajectory.

The profile length is the distance between the recorded GPS points where the laser altimeter has taken measurements at heights of less than 20 m above the ice.

The number of detected ridges Pressure ridges with a minimum height, here 0.8 m, are classified according to the Rayleigh criterion. Their number tends to be overestimated because floe edges and abrupt flight changes form similar profile features. In addition, it is difficult to determine individual ridges in heavily deformed areas and rubble fields. Very broad ridges with several separated peaks can therefore be considered as multiple ridge sails. However, this effect is the same for different

profiles and the comparison with laser scanner data has shown that the method is
suitable for identifying ridges.

The ridge width is determined by the left and right boundary which are reached when
the troughs on both sides reach a height of 0.3 m. Thus, the width does not include
the ridge elements below this threshold, so that smaller rubble, for example, is not
considered. Furthermore, the angle at which the ridge is flown over is not known
and can lead to an overestimation of the ridge width.

The ridge height includes all measurements of the sea ice surface between the left and
right ridge boundaries.

The ridge peak height is the highest point of the ridges and shows only a slight devia-
tion in the range of a few centimetres compared to those of the ALS. An average
underestimation of about 10 cm in strongly deformed areas can be estimated.

The ridge spacing is the distance between the ridge boundaries. It is therefore affected
by the width and the number of identified ridges. The average spacing of ridges in
the profile increases with the amount of open water.

These parameters can be used to calculate also the ridge density, the number of ridges
per kilometer, and the ridge intensity, the ratio of mean ridge height and spacing. Here,
as well, the proportion of open water should be taken into account when comparing the
profiles. Their values are decreasing with large ice free areas.

The statistical roughness parameters mean height, RMS height, skewness, kurtosis,
RMS slope, the fractal dimension and its break point where analysed and com-
pared with ALS data. At this point it is important that natural surfaces are not
stationary but exhibit power-law behavior. Therefore, statistic properties of a pro-
file such as the mean height, RMS height, skewness and kurtosis depend on the
profile length. It is thus not recommended to compare profiles of different lengths.
It was found that the mean height, RMS height and skewness best represent the
characteristics of the profiles. They offer the possibility to describe characteristic
properties beyond the ridge statistics.

This programming routine will help to improve the understanding of past and future
changes of sea ice and the associated climate. One of the future goals will be to study
the changes of ridge statistics in the Arctic, e.g. their height and density, over the last
decades and to put them in the context of current changes in the Arctic, such as the

decrease in ice thickness or increased drift speeds. It already has been used to study surface roughness from measurements of the 2019 MOSAiC (Multidisciplinary drifting Observatory for the Study of Arctic Climate) expedition by von Albedyll in "Thermodynamic and dynamic contributions to seasonal Arctic sea ice thickness distributions from airborne observations". The temporal development of the ice thickness distribution was investigated and the results are submitted for publication.

In the future, the three-step filtering method for deriving the surface height could be compared with a method that models the trajectory by iterative curve fitting using nonlinear least squares optimisation as used by Beckers et al. (2015). In this process, an initial curve is fitted to the measured height of the altimeter above the ice. Then points whose size is smaller than that of the curve, which would result in negative surface heights, are discarded and the curve fitting is repeated. By discarding these points, the curve is fitted to the level ice. An iterative curve fitting like this, in combination with Hibler's method, could potentially reduce the amount of negative points in the surface profile even more. Future studies could also investigate the influence of different flight styles and the difference between helicopters and airplanes on the filter parameters. Finally, it would be a great improvement for the future if it were possible to distinguish open water from undeformed ice, e.g. by different backscatter intensities, and routinely include INS data for each flight to correct for changes in attitude.

References

AMAP (1998), *AMAP assessment report: Arctic pollution issues*, Oslo, Norway.

Arya, S. P. S. (1973), 'Contribution of form drag on pressure ridges to the air stress on arctic ice', *Journal of Geophysical Research* **78**(30).

Arya, S. P. S. (1975), 'A drag partition theory for determining the large-scale roughness parameter and wind stress on the arctic pack ice', *Journal of Geophysical Research* **80**(24).

AWI (2019), 'Meereisportal: Snow depth on arctic sea ice'.
URL: *https://www.meereisportal.de/en/archive/2019-kurzmeldungen-gesamttexte/snow-depth-on-arctic-sea-ice/*

AWI (2021*a*), 'Meereisportal: Driftstories – 10: Ein wiedersehen am ausgangstor der arktis'.
URL: *https://www.meereisportal.de/mosaic/driftstories/driftstories-10-ein-wiedersehen-am-ausgangstor-der-arktis/*

AWI (2021*b*), 'Meereisportal: Flugzeug-fernerkundung'.
URL:
https://www.meereisportal.de/meereisbeobachtung/methoden/flugzeug-fernerkundung/

Banke, E. G., Smith, S. D. & Anderson, R. J. (1976), 'Recent measurements of wind stress on arctic sea ice', *Journal of the Fisheries Research Board of Canada* **33**(10), 2307–2317.

Barry, R. G. & Gan, T. Y. (2011), *The Global Cryosphere: Past, present, and future*, Cambridge University Press, Cambridge.

Barry, R. G., Moritz, R. E. & Rogers, J. C. (1979), 'The fast ice regimes of the beaufort and chukchi sea coasts, alaska', *Cold Regions Science and Technology* **1**(2), 129–152.

Beckers, J. F., Renner, A. H., Spreen, G., Gerland, S. & Haas, C. (2015), 'Sea-ice surface roughness estimates from airborne laser scanner and laser altimeter

observations in fram strait and north of svalbard', *Annals of glaciology* **56**(69), 235–244.

Bhushan, B. (2000), *Surface roughness analysis and measurement techniques.*

Bing, T., Peng, L., Zhijun, L. & Runling, L. (2013), 'Form drag on pressure ridges and drag coefficient in the northwestern weddell sea, antarctica, in winter', *Annals of glaciology* **54**(62), 133–138.

Bishop, G. C. & Chellis, S. E. (1989), 'Fractal dimension: A descriptor of ice keel surface roughness', *Geophysical Research Letters* **16**(9), 1007–1010.

Castellani, G., Lüpkes, C., Hendricks, S. & Gerdes, R. (2014), 'Variability of arctic sea-ice topography and its impact on the atmospheric surface drag', *Journal of Geophysical Research: Oceans* **119**(10), 6743–6762.

Colony, R. & Thorndike, A. S. (1985), 'Sea ice motion as a drunkard's walk', *Journal of Geophysical Research* **90**(C1), 965.

Déry, S. J. & Tremblay, L.-B. (2004), 'Modeling the effects of wind redistribution on the snow mass budget of polar sea ice*', *Journal of Physical Oceanography* **34**(1), 258–271.

Dierking, W. (1995), 'Laser profiling of the ice surface topography during the winter weddell gyre study 1992', *Journal of Geophysical Research* **100**(C3), 4807.

Duncan, K., Farrell, S. L., Connor, L. N., Richter-Menge, J., Hutchings, J. K. & Dominguez, R. (2018), 'High-resolution airborne observations of sea-ice pressure ridge sail height', *Annals of glaciology* **59**(76pt2), 137–147.

Eicken, H., Grenfell, T. C., Perovich, D. K., Richter-Menge, J. A. & Frey, K. (2004), 'Hydraulic controls of summer arctic pack ice albedo', *Journal of Geophysical Research* **109**(C8).

Fassnacht, S. R., Williams, M. W. & Corrao, M. V. (2009), 'Changes in the surface roughness of snow from millimetre to metre scales', *Ecological Complexity* **6**(3), 221–229.

Fitterman, D. V. & Yin, C. (2004), 'Effect of bird maneuver on frequency–domain helicopter em response', *GEOPHYSICS* **69**(5), 1203–1215.

Fors, A. S., Brekke, C., Doulgeris, A. P., Eltoft, T., Renner, A. H. H. & Gerland, S. (2016), 'Late-summer sea ice segmentation with multi-polarisation sar features in c and x band', *The Cryosphere* **10**(1), 401–415.

Gegiuc, A., Similä, M., Karvonen, J., Lensu, M., Mäkynen, M. & Vainio, J. (2018), 'Estimation of degree of sea ice ridging based on dual-polarized c-band sar data', *The Cryosphere* **12**(1), 343–364.

Girard, L., Weiss, J., Molines, J. M., Barnier, B. & Bouillon, S. (2009), 'Evaluation of high-resolution sea ice models on the basis of statistical and scaling properties of arctic sea ice drift and deformation', *Journal of Geophysical Research* **114**(C8).

Goff, J. A., Stewart, W. K., Singh, H. & Tang, X. (1995), 'Quantitative analysis of sea ice draft: 2. application of stochastic modeling to intersecting topographic profiles', *Journal of Geophysical Research* **100**(C4), 7005.

Goodwin, I. D. (1990), 'Snow accumulation and surface topography in the katabatic zone of eastern wilkes land, antarctica', *Antarctic Science* **2**(3), 235–242.

Guest, P. S. & Davidson, K. L. (1991), 'The aerodynamic roughness of different types of sea ice', *Journal of Geophysical Research* **96**(C3), 4709.

Guest, P. S., Davidson, K. L., Overland, J. E. & Frederickson, P. A. (1995), Atmosphere-ocean interactions in the marginal ice zones of the nordic seas, *in* W. O. Smith & J. M. Grebmeir, eds, 'Arctic Oceanography: Marginal Ice Zones and Continental Shelves', Vol. 49 of *Coastal and Estuarine Studies*, American Geophysical Union, Washington, D. C., pp. 51–95.

Haas, C., Lobach, J., Hendricks, S., Rabenstein, L. & Pfaffling, A. (2009), 'Helicopter-borne measurements of sea ice thickness, using a small and lightweight, digital em system', *Journal of Applied Geophysics* **67**(3), 234–241.

Hay, W., Wold, C. & DeConto, R. (1998), 'The role of salinity in circulation of the cretaceous ocean'.

Hendricks, S., Ricker, R. & Jutila, A. (2019), 'Icebird 2019 winter: Icesat-2 validation data acquisition report'.

Hibler, W. D. (1972), 'Removal of aircraft altitude variation from laser profiles of the arctic ice pack', *Journal of Geophysical Research* **77**(36), 7190–7195.

Hibler, W. D. (1975), 'Characterization of cold-regions terrain using airborne laser profilometry', *Journal of Glaciology* **15**(73), 329–347.

Hibler, W. D., Flato, G. M. & Trenberth, K. E. e. (1992), 'Climate system modelling', pp. 413–436.

Hibler, W. D., Weeks, W. F. & Mock, S. J. (1972), 'Statistical aspects of sea-ice ridge distributions', *Journal of Geophysical Research* **77**(30), 5954–5970.

Höfle, B., Vetter, M., Pfeifer, N., Mandlburger, G. & Stötter, J. (2009), 'Water surface mapping from airborne laser scanning using signal intensity and elevation data', *Earth Surface Processes and Landforms* **34**(12), 1635–1649.

Holladay, J. S., Lo, B. & Prinsenberg, S. K., eds (1997), *Bird orientation effects in quantitative airborne electromagnetic interpretation of pack ice thickness sounding.*

Jakobsson, M. (2002), 'Hypsometry and volume of the arctic ocean and its constituent seas', *Geochemistry, Geophysics, Geosystems* **3**(5), 1–18.

Jenoptik (2017), 'Laser distance meter ldm301 user manual: Documentation number: 012861-301-98hb-g044-b0'.

Johansson, A. M., King, J. A., Doulgeris, A. P., Gerland, S., Singha, S., Spreen, G. & Busche, T. (2017), 'Combined observations of arctic sea ice with near-coincident colocated x-band, c-band, and l-band sar satellite remote sensing and helicopter-borne measurements', *Journal of Geophysical Research: Oceans* **122**(1), 669–691.

Key, J. & McLaren, A. S. (1991), 'Fractal nature of the sea ice draft profile', *Geophysical Research Letters* **18**(8), 1437–1440.

Kovacs, A. (1970), 'On the structure of pressured sea ice'.

Kovacs, A. & Holladay, J. S. (1990), 'Sea–ice thickness measurement using a small airborne electromagnetic sounding system', *GEOPHYSICS* **55**(10), 1327–1337.

Kovacs, A. & Morey, R. M. (1991), 'Sounding sea ice thickness using a portable electromagnetic induction instrument', *GEOPHYSICS* **56**(12), 1992–1998.

Kovacs, A., Valleau, N. & Holladay, J. S. (1987), 'Airborne electromagnetic sounding of sea ice thickness and sub-ice bathymetry', *Cold Regions Science and Technology* **14**(3), 289–311.

Kovacs, A., Weeks, W. F., Ackley, S. & Hibler, W. D. (1973), 'Structure of a multi-year pressure ridge', *ARCTIC* **26**(1).

Krumpen, T., Belter, H. J., Boetius, A., Damm, E., Haas, C., Hendricks, S., Nicolaus, M., Nöthig, E.-M., Paul, S., Peeken, I., Ricker, R. & Stein, R. (2019), 'Arctic warming interrupts the transpolar drift and affects long-range transport of sea ice and ice-rafted matter', *Scientific Reports* **9**(1), 5459.
URL: *https://www.nature.com/articles/s41598-019-41456-y*

Landy, J. C., Ehn, J. K. & Barber, D. G. (2015), 'Albedo feedback enhanced by smoother arctic sea ice', *Geophysical Research Letters* **42**(24).

Landy, J. C., Petty, A. A., Tsamados, M. & Stroeve, J. C. (2020), 'Sea ice roughness overlooked as a key source of uncertainty in cryosat–2 ice freeboard retrievals', *Journal of Geophysical Research: Oceans* **125**(5).

Lange, B. A., Beckers, J. F., Casey, J. A. & Haas, C. (2019), 'Airborne observations of summer thinning of multiyear sea ice originating from the lincoln sea', *Journal of Geophysical Research: Oceans* **124**(1), 243–266.

Leppaeranta, M. (2011), *The Drift of Sea Ice*, Springer Praxis Books, Springer Berlin Heidelberg, Berlin, Heidelberg.

Lewis, J. E., LeppäRanta, M. & Granberg, H. B. (1993), 'Statistical properties of sea ice surface topography in the baltic sea', *Tellus A: Dynamic Meteorology and Oceanography* **45**(2), 127–142.

Lindsay, R. W. & Zhang, J. (2005), 'The thinning of arctic sea ice, 1988–2003: Have we passed a tipping point?', *Journal of Climate* **18**(22), 4879–4894.

Lüpkes, C., Gryanik, V. M., Hartmann, J. & Andreas, E. L. (2012), 'A parametrization, based on sea ice morphology, of the neutral atmospheric drag coefficients for weather prediction and climate models', *Journal of Geophysical Research* **117**(D13).

Lyon, W. (1963), 'The submarine and the arctic ocean', *Polar Record* **11**(75), 699–705.

Magsipoc, E., Zhao, Q. & Grasselli, G. (2020), '2d and 3d roughness characterization', *Rock Mechanics and Rock Engineering* **53**(3), 1495–1519.

Manninen, A. T. (1997), 'Surface roughness of baltic sea ice', *Journal of Geophysical Research* **102**(C1), 1119–1139.

Marshall, S. (2012), *The cryosphere*, Princeton primers in climate, Princeton University Press, Princeton, N.J.

Martin, T. (2006), 'Comparison of different ridge formation models of arctic sea ice with observations from laser profiling', *Annals of glaciology* **44**, 403–410.

Martin, T. (2007), *Arctic Sea Ice Dynamics: Drift and Ridging in Numerical Models and Observations.*

Maykut, G. A. & Untersteiner, N. (1971), 'Some results from a time-dependent thermodynamic model of sea ice', *Journal of Geophysical Research* **76**(6), 1550–1575.

Menge, J. A. R. & Jones, K. F. (1993), 'The tensile strength of first-year sea ice', *Journal of Glaciology* **39**(133), 609–618.

Meredith, M., Sommerkorn, M., Cassotta, S., Derksen, C., Ekaykin, A., Hollowed, A., Kofinas, G., Mackintosh, A., Melbourne-Thomas, J., Muelbert, M., Ottersen, G., Pritchard, H. & Schuur, E. (2019), *Polar Regions. Chapter 3, IPCC Special Report on the Ocean and Cryosphere in a Changing Climate.*

Mock, S. J., Hartwell, A. D. & Hibler, W. D. (1972), 'Spatial aspects of pressure ridge statistics', *Journal of Geophysical Research* **77**(30), 5945–5953.

Multala, J., Hautaniemi, H., Oksama, M., LeppäRanta, M., Haapala, J., Herlevi, A., Riska, K. & Lensu, M. (1996), 'An airborne electromagnetic system on a fixed wing aircraft for sea ice thickness mapping', *Cold Regions Science and Technology* **24**(4), 355–373.

Nolin, A. & Mar, E. (2019), 'Arctic sea ice surface roughness estimated from multi-angular reflectance satellite imagery', *Remote Sensing* **11**(1), 50.

Notz, D. & Community, S. (2020), 'Arctic sea ice in cmip6', *Geophysical Research Letters* **47**(10).

NSIDC (2020), 'Dynamics: Circulation'.
URL: *https://nsidc.org/cryosphere/seaice/processes/circulation.html*

Parmerter, R. R. & Coon, M. D. (1972), 'Model of pressure ridge formation in sea ice', *Journal of Geophysical Research* **77**(33), 6565–6575.

Perovich, D., Meier, W., Tschudi, M., Hendricks, S., Petty, A. A., Divine, D., Farrell, S., Gerland, S., Haas, C., Kaleschke, L., Pavlova, O., Ricker, R., Tian-Kunze, X., Wood, K. & Webster, M. (2020), 'Arctic report card 2020: Sea ice'.

Peterson, I. K., Prinsenberg, S. J. & Holladay, J. S. (2008), 'Observations of sea ice thickness, surface roughness and ice motion in amundsen gulf', *Journal of Geophysical Research* **113**(C6).

Peterson, I. K., Prinsenberg, S. J., Holladay, J. S. & Lalumiere, L. A. (2002), Validation of sea ice signatures in radarsat scansar imagery for the gulf of st. lawrence, *in* 'IEEE International Geoscience and Remote Sensing Symposium', IEEE, pp. 146–148.

Petrich, C. & Eicken, H. (2009), Growth, structure and properties of sea ice, *in* D. N. Thomas & G. S. Dieckmann, eds, 'Sea Ice', Wiley, Oxford, UK, pp. 23–77.

Pfaffhuber, A. A., Hendricks, S. & Kvistedal, Y. A. (2012), 'Progressing from 1d to 2d and 3d near-surface airborne electromagnetic mapping with a multisensor, airborne sea-ice explorer', *GEOPHYSICS* **77**(4).

Pfaffling, A., Haas, C. & Reid, J. (2004), 'Empirical processing of hem: 10th european meeting of environmental and engineering'.

Prinsenberg, S. J., van Der Baaren, A. & Peterson, I. K. (2006), 'Ice ridging and ice drift in southern gulf of st lawrence, canada, during winter storms', *Annals of glaciology* **44**, 411–417.

Rabenstein, L., Hendricks, S., Martin, T., Pfaffhuber, A. & Haas, C. (2010), 'Thickness and surface-properties of different sea-ice regimes within the arctic trans polar drift: Data from summers 2001, 2004 and 2007', *Journal of Geophysical Research* **115**(C12).

Riegl (2010), 'Laser distance and level meter ld90-3 user's manual'.

Riegl (2012), 'Riegl vq-580 - datasheet'.

Rothrock, D. A. & Thorndike, A. S. (1980), 'Geometric properties of the underside of sea ice', *Journal of Geophysical Research* **85**(C7).

Sachs, L. (2004), *Angewandte Statistik: Anwendung statistischer Methoden*, elfte, überarbeitete und aktualisierte auflage edn, Springer Berlin Heidelberg, Berlin, Heidelberg.

Saldern, C. V. (2007), 'Bestimmung verschiedener eisklassen durch statistische analyse der rauigkeit von meereis'.

Saldern, C. V., Busche, T., Haas, C. & Dierking, W. (2004), 'Analysis of sea ice surface roughness and thickness profiles for improvement of sar ice type classification'.

Saldern, C. V., Haas, C. & Dierking, W. (2006), 'Parameterization of arctic sea-ice surface roughness for application in ice type classification', *Annals of glaciology* **44**, 224–230.

Sayles, R. S. & Thomas, T. R. (1978), 'Surface topography as a nonstationary random process', *Nature* **271**(5644), 431–434.

Schweiger, A. J., Steele, M., Zhang, J., Moore, G. W. K. & Laidre, K. L. (2021), 'Accelerated sea ice loss in the wandel sea points to a change in the arctic's last ice area', *Communications Earth & Environment* **2**(1), 1–11.
URL: *https://www.nature.com/articles/s43247-021-00197-5*

Serreze, M. C., Key, J. R., Box, J. E., Maslanik, J. A. & Steffen, K. (1998), 'A new monthly climatology of global radiation for the arctic and comparisons with ncep–ncar reanalysis and isccp-c2 fields', *Journal of Climate* **11**(2), 121–136.

Shepard, M. K., Campbell, B. A., Bulmer, M. H., Farr, T. G., Gaddis, L. R. & Plaut, J. J. (2001), 'The roughness of natural terrain: A planetary and remote sensing perspective', *Journal of Geophysical Research* **106**(E12), 32777–32795.

Sinnott, R. (1984), 'Virtues of the haversine: Sky and telescope', **68**, 159.

Smeets, C. J. P. P., Duynkerke, P. G. & Vugts, H. F. (1999), 'Observed wind profiles and turbulence fluxes over an ice surface with changing surface roughness', *Boundary-Layer Meteorology* **92**(1), 99–121.

Strub-Klein, L. & Sudom, D. (2012), 'A comprehensive analysis of the morphology of first-year sea ice ridges', *Cold Regions Science and Technology* **82**, 94–109.

Sturm, M. (2002), 'Winter snow cover on the sea ice of the arctic ocean at the surface heat budget of the arctic ocean (sheba): Temporal evolution and spatial variability', *Journal of Geophysical Research* **107**(C10).

Sturm, M., Morris, K. & Massom, R. (1998), The winter snow cover of the west antarctic pack ice: Its spatial and temporal variability, *in* M. O. Jeffries, ed.,

'Antarctic Sea Ice: Physical Processes, Interactions and Variability', Antarctic Research Series, American Geophysical Union, Washington, D. C., pp. 1–18.

Sudom, D., Timco, G., Sand, B. & Fransson, L. (2011), 'Analysis of first-year and old ice ridge characteristics'.

Tan, B., Li, Z.-j., Lu, P., Haas, C. & Nicolaus, M. (2012), 'Morphology of sea ice pressure ridges in the northwestern weddell sea in winter', *Journal of Geophysical Research* **117**(C6).

Thoman, R. L., Richter-Menge, J. & Druckenmiller, M. L. (2020), 'Arctic report card 2020: Executive summary'.

Thomas, D. N. & Dieckmann, G. S., eds (2009), *Sea Ice*, Wiley, Oxford, UK.

Thomas, T. R. (1981), 'Characterization of surface roughness', *Precision Engineering* **3**(2), 97–104.

Thorndike, A. S. (1986), Kinematics of sea ice, *in* N. Untersteiner, ed., 'The Geophysics of Sea Ice', Springer US, Boston, MA, pp. 489–549.

Thorndike, A. S. & Colony, R. (1982), 'Sea ice motion in response to geostrophic winds', *Journal of Geophysical Research* **87**(C8), 5845.

Timco, G. W. & Burden, R. P. (1997), 'An analysis of the shapes of sea ice ridges', *Cold Regions Science and Technology* **25**(1), 65–77.

Timmermans, M.-L. & Marshall, J. (2020), 'Understanding arctic ocean circulation: A review of ocean dynamics in a changing climate', *Journal of Geophysical Research: Oceans* **125**(4).

Tucker, W. B. & Govoni, J. W. (1981), 'Morphological investigations of first-year sea ice pressure ridge sails', *Cold Regions Science and Technology* **5**(1), 1–12.

Tucker, W. B., Sodhi, D. S. & Govoni, J. W. (1984), Structure of first-year pressure ridge sails in the prudhoe bay region, *in* 'The Alaskan Beaufort Sea', Elsevier, pp. 115–135.

Volkov, V. A., Mushta, A. & Demchev, D. (2020), Sea ice drift in the arctic, *in* O. M. Johannessen, L. P. Bobylev, E. V. Shalina & S. Sandven, eds, 'Sea Ice in the Arctic', Springer Polar Sciences, Springer International Publishing, Cham, pp. 301–313.

von Albedyll, L. (2021), 'Thermodynamic and dynamic contributions to seasonal arctic sea ice thickness distributions from airborne observations (submitted for publication to [elementa])'.

Wadhams, P. (1980*a*), *A Comparison of Sonar and Laser Profiles along Corresponding Tracks in the Arctic Ocean.*

Wadhams, P. (1980*b*), 'Ice characteristics in the seasonal sea ice zone', *Cold Regions Science and Technology* **2**, 38–87.

Wadhams, P. (2014), *Ice in the Ocean*, first edition edn, CRC Press, Boca Raton, FL.

Wadhams, P. & Davy, T. (1986), 'On the spacing and draft distributions for pressure ridge keels', *undefined* .

Wadhams, P. & Horne, R. J. (1980), 'An analysis of ice profiles obtained by submarine sonar in the beaufort sea', *Journal of Glaciology* **25**(93), 401–424.

Wadhams, P. & Toberg, N. (2012), 'Changing characteristics of arctic pressure ridges', *Polar Science* **6**(1), 71–77.

Wadhams, P., Tucker, W. B., Krabill, W. B., Swift, R. N., Comiso, J. C. & Davis, N. R. (1992), 'Relationship between sea ice freeboard and draft in the arctic basin, and implications for ice thickness monitoring', *Journal of Geophysical Research* **97**(C12), 20325.

Warren, S. G., Rigor, I. G., Untersteiner, N., Radionov, V. F., Bryazgin, N. N., Aleksandrov, Y. I. & Colony, R. (1999), 'Snow depth on arctic sea ice', *Journal of Climate* **12**(6), 1814–1829.

Weeks, W. F., Kovacs, A. & Hibler, W. D. (1971), 'Pressure ridge characteristics in the arctic coastal environment'.

Weiss, A. I., King, J., Lachlan-Cope, T. & Ladkin, R. (2011), 'On the effective aerodynamic and scalar roughness length of weddell sea ice', *Journal of Geophysical Research* **116**(D19).

Willmes, S. & Heinemann, G. (2016), 'Sea-ice wintertime lead frequencies and regional characteristics in the arctic, 2003–2015', *Remote Sensing* **8**(1), 4.
    URL: *https://www.mdpi.com/2072-4292/8/1/4/htm*

WMO (2014), *Sea-Ice Nomenclature*, Geneva.

Zabel, I. H. H., Jezek, K. C., Gogineni, S. P. & Kanagaratnam, P. (1996), 'Search for proxy indicators of young sea ice thickness', *Journal of Geophysical Research* **101**(C3), 6697–6709.

List of Figures

80

List of Tables

A Output files (.csv, .html, .txt)

Table A.1: Header line and columns of each .csv file

fid	Fiducial number
lat	Latitude in degrees north
lon	Longitude in degrees east
distance[m]	Distance between two Latitude and Longitude points
altimeter_height[m]	Laser height in meter
modelled_trajectory[m]	Modelled flight trajectory (Laser height above level ice) in meter
profile_height[m]	Sea ice elevation with respect to level ice in meter
ridge_peak[m]	Highest ridge peak height in meter
left_border[m]	Sea ice elevation of the left ridge border in meter
width[m]	Sea ice elevation of the right ridge border in meter
spacing[m]	Distance between ridge borders in meter
ridge_heights[m]	Surface elevation of ridges between ridge border in meter
d	Day (from the file _alt.dat)
m	Month (from the file _alt.dat)
y	Year (from the file _alt.dat)
EM	EM derived ice thicknesses in meter (from the file _alt.dat)

Table A.2: Descriptive parameters in each .txt file

profile length [m]
mean surface elevation [m]
number of detected ridges
mean ridge height [m]
mean highest ridge peak height [m]
maximum ridge height [m]
mean ridge width [m]
mean ridge spacing [m]
ridge density (number of ridges per km)
ridge intensity (ratio of mean sail height and spacing)
cut-off (smallest ridge height)
R_a - arithmetic average of the height
R_q - RMS roughness
R_{sk} - skewness

Table A.3: Figures, descriptive parameters and probability distributions of each .html file

Figures:
    1: The result of the high and low pass filtering and identified minimum points
    2: The surface profile with reference to the level ice
    3: The surface profile with detected peaks ($>$ cut-off), classified ridges and their widths

Profile properties:
    profile length [m]
    mean surface elevation [m]

    number of detected ridges
    mean ridge height [m]
    mean highest ridge peak height [m]
    maximum ridge height [m]
    mean ridge width [m]
    mean ridge spacing [m]
    ridge density (number of ridges per km)
    ridge intensity (ratio of mean sail height and spacing)
    cut-off (smallest ridge height)

    R_a - arithmetic average of the height
    R_q - RMS roughness
    R_{sk} - skewness

Probability distribution:
    1. Ridge height
    2. Highest ridge peak height
    3. Ridge spacing
    4. Surface elevation with respect to level ice

B Python Script

```python
###########################################################################
#IMPORT
###########################################################################

import os
import math
import argparse
import logging

import numpy as np
import pandas as pd
from scipy import signal

import plotly.graph_objs as go
from plotly.subplots import make_subplots
import plotly


###########################################################################
#CMD - USER INPUT
###########################################################################

# go to directory of python file (cd)
# input: python file.py "C:\...\123_alt.dat"
# append -f if _allfinal.dat is present
# append -O if you want to overwrite existing file


def cli():

    # basename = r"C:\Users\miras\Desktop\AWI\DATA\embird-icebird2019-altimeter (for validation)
        \20190410_01\isit\201904101548_alt.dat"

    parser = argparse.ArgumentParser(description='Laser Altimeter Processing')
    parser.add_argument(dest='basename',
                        nargs='?',
                        metavar='BASENAME',
                        # default = basename,
                        help='(base)name of file(s) including path')
    parser.add_argument('-o','--outname',
                        dest='outname',
```

```python
                        nargs="?",
                        metavar='ROOTNAME',
                        help='(base)name of output file(s) [BASENAME]')
parser.add_argument('-a','--alt',
                        nargs="?",
                        metavar='FILE',
                        help='name of _alt.dat file [BASENAME_alt.dat]')
parser.add_argument('-g','--gps',
                        nargs="?",
                        metavar='FILE',
                        help='name of _gps.dat file [BASENAME_gps.dat]')

mutex_a=parser.add_mutually_exclusive_group()
mutex_a.add_argument('-f','--use-allfinal',
                        action='store_true',
                        default=False,
                        help='do use an _allfinal.dat file')
mutex_a.add_argument('-F','--allfinal',
                        nargs="?",
                        metavar='FILE',
                        help='name of _allfinal.dat file [BASENAME_allfinal.dat]')

parser.add_argument('-O','--overwrite',
                        action='store_true',
                        default=False,
                        help='overwrite existing data')


mutex_v=parser.add_mutually_exclusive_group()
mutex_v.add_argument('-v', '--verbose', dest='verb', action='store_const',
                        const=logging.INFO, help='enable verbose output')
mutex_v.add_argument(   '--debug', dest='verb', action='store_const',
                        const=logging.DEBUG, help='enable debugging output')
parser.set_defaults(verb=logging.WARNING)
arglist = vars(parser.parse_args())
logging.getLogger().setLevel(arglist['verb'])


arglist['basename'] = arglist['basename'][0:len(arglist['basename'])-8]

if arglist['alt'] is None:
    arglist['alt'] = arglist['basename']+'_alt.dat'
logging.info('selected alt    file: %s'%arglist['alt'])

if arglist['gps'] is None:
    arglist['gps'] = arglist['basename']+'_gps.dat'
logging.info('selected gps    file: %s'%arglist['gps'])

if arglist['use_allfinal']:
    arglist['allfinal'] = arglist['basename']+'_allfinal.dat'
```

```python
    elif arglist['allfinal'] is None:
        arglist['allfinal'] = ''

    if arglist['outname'] is None:
        arglist['outname'] = arglist['basename']
    logging.info('selected allfinal file: %s'%arglist['allfinal'])

    logging.debug(str(arglist))
    return arglist



################################################################################
#FUNCTIONS
#distance between two GPS coordinates in meter
#haversine formula (Sinnott, R.W. (1984): Virtues of the Haversine. Sky and Telescope 68, p. 159.)
################################################################################

def func_distance(lat1, lon1, lat2, lon2):
    radius = 6371 # km

    dlat = math.radians(lat2-lat1)
    dlon = math.radians(lon2-lon1)
    a = math.sin(dlat/2) * math.sin(dlat/2) + math.cos(math.radians(lat1)) \
        * math.cos(math.radians(lat2)) * math.sin(dlon/2) * math.sin(dlon/2)
    c = 2 * math.atan2(math.sqrt(a), math.sqrt(1-a))
    d = radius * c

    return d*1000

def save_html(name, data, figs):

    logging.info('saving html file %s'%name)

    text = """
    <html>
        <body>
            <font face="Calibri Light">
                <h3> %s </h3>
                <p>
                    profilelength: %.2f m <br>
                    mean surface elevation: %.2f m <br><br>
                    number of detected ridges: %d <br>
                    mean ridge height: %.2f m <br>
                    mean highest ridge peak height: %.2f m <br>
                    maximum ridge: %.2f m <br>
                    mean ridge width: %.2f m <br>
                    mean ridge spacing: %.2f m <br>
                    ridge density (number per km): %.2f <br>
                    ridge intensity (ratio of mean ridge height and spacing): %.4f <br>
                    cutoff = %.1f m <br><br>
                    Ra - arithmetic average of the height: %.2f <br>
```

```python
                        Rq - RMS roughness: %.2f<br>
                        Rsk - skewness: %.2f<br><br>
                    </p>
                </font>
            </body>
        </html>
        """

    with open(name, 'a') as f:
        f.truncate(0)
        f.write(figs['filter'].to_html(full_html=False, include_plotlyjs='cdn'))
        f.write(figs['profile'].to_html(full_html=False, include_plotlyjs='cdn'))
        f.write(figs['ridge'].to_html(full_html=False, include_plotlyjs='cdn'))
        f.write(text%data)
        f.write(figs['ridge_height'].to_html(full_html=False, include_plotlyjs='cdn'))
        f.write(figs['ridge_peak'].to_html(full_html=False, include_plotlyjs='cdn'))
        f.write(figs['spacing'].to_html(full_html=False, include_plotlyjs='cdn'))
        f.write(figs['height'].to_html(full_html=False, include_plotlyjs='cdn'))


def save_txt(name, txt_data):

    logging.info('saving text file %s'%name)

    txt_text = """%s

    profilelength: %.2f m
    mean surface elevation: %.2f m

    number of detected ridges: %d
    mean ridge height: %.2f m
    mean highest ridge peak height: %.2f m
    maximum ridge: %.2f m
    mean ridge width: %.2f m
    mean ridge spacing: %.2f m
    ridge density (number per km): %.2f
    ridge intensity (ratio of mean sail height and spacing): %.4f
    cutoff = %.1f m

    Ra - arithmetic average of the height: %.2f
    Rq - RMS roughness: %.2f
    Rsk - skewness: %.2f
    """
    with open(name, '+w') as f:
        f.write(txt_text%txt_data)
        f.close()


#############################################################################
# MAIN PROGRAM
#############################################################################
```

```python
def main():
    arglist = cli()

    alt_file = arglist['alt'].replace('\\', '/')
    gps_file = arglist['gps'].replace('\\', '/')

    ###########################################################################
    # READ DATA
    logging.info('read data')
    ###########################################################################

    logging.info('... laser data')
    laser = pd.read_table(alt_file, delim_whitespace=True, skiprows=1, names=('gpst', 'height', '
        echo100','echo10'))

    logging.info('... gps data')
    gps = pd.read_table(gps_file, delim_whitespace=True, skiprows=1, names=('week', 'sec', 'lat',
        'lon','height', 'fid', 'spd', 'dir'))

    allfinal_file = arglist['allfinal'].replace('\\', '/')
    if allfinal_file != "":
        logging.info('... allfinal data')
        allfinal = pd.read_table(allfinal_file, delim_whitespace=True, names=('y', 'm', 'd', 'GPST'
            , 'FID', 'LAT', 'LON', 'distance', 'EM_height', 'laser_height'))
    else:
        logging.info('omitting allfinal data')


    ###########################################################################
    #DATE OF SURVEY
    ###########################################################################

    date = os.path.basename(alt_file)
    date = date.replace('_alt.dat', '')
    logging.debug('date: %s'%date)

    ###########################################################################
    #MERGE FILES
    logging.info('merging data ...')
    ###########################################################################

    #merge _alt.dat and _gps.dat
    logging.debug('... laser and gps data')
    gps['fid']=gps['fid'].astype(float)
    file=laser.merge(gps, how='left',left_on='gpst', right_on='fid')
    file_start_idx = next(idx for idx, value in enumerate(file['fid']) if value >= 0)
    file = file.iloc[file_start_idx:,]
    file = file.reset_index(drop=True)

    file['dis'] = 0
    file['state'] = 1
```

```python
file['filt_sig'] = np.nan
file['minimum_points'] = np.nan
file['minimum_curve'] = np.nan
file['motion'] = np.nan
file['profile'] = np.nan
file['missing_data'] = 1
file['DX'] = np.nan

#merge _allfinal.dat
if allfinal_file != "":
    logging.info('... allfinal data')
    allfinal['FID']=allfinal['FID'].astype(float)
    file=file.merge(allfinal, how='left', left_on='fid', right_on='FID').drop(columns=['GPST',
        'FID', 'LAT', 'LON'])
else:
    logging.debug('omitting allfinal data')

logging.info('_alt.dat missing data')


############################################################################
# MISSING LASER DATA
# there must be at least p values per second
# p = int(float(input("Please enter minimum amount of points per gps second (5): ")))
p = 5
############################################################################

file.loc[file['height_x'] > 999, 'missing_data'] = np.nan

i=file.iloc[0,0]
while i < math.floor(file.iloc[-1,0,]):

    if file['gpst'].isin([i])[0] == False or file['gpst'].isin([i+1])[0] == False:
        i = i + 1
    else:
        idx_s = file[file['gpst']==i].index.values[0]

        idx_e = file[file['gpst']==i+1].index.values[0]

        count = file.iloc[idx_s:idx_e,19].isna().sum()

        if count > p:
            file.iloc[idx_s:idx_e,19] = np.nan

        i = i + 1


############################################################################
# ADJUST GPS FILE
# linear interpolation of lattitude and longitude
logging.info('adjust gps file')
```

```python
###########################################################################

file["lat"]=file["lat"].interpolate(method='linear')

file["lon"]=file["lon"].interpolate(method='linear')


###########################################################################
#CALCULATE DISTANCE BETWEEN COORDINATES
logging.info('calculate distance')
###########################################################################

for i, value in enumerate(file['sec']):
    if i == 0:
        continue

    file.iloc[i, 12] = file.iloc[i-1, 12] + func_distance(file.iloc[i-1, 6], file.iloc[i-1, 7],
        file.iloc[i, 6], file.iloc[i, 7])

###########################################################################
#CALCULATE POINT SPACING (DX)
logging.info('calculate point spacing DX')
###########################################################################

for i, value in enumerate(file['dis']):
    if i == 0:
        continue
    else:
        file.iloc[i,20] = file.iloc[i,12] - file.iloc[i-1,12]


###########################################################################
# EDIT LASER
# linear interpolation of NaN values to remove noisy data
# remove 999 values and outliers from laser
logging.info('edit laser')

# if the height difference between the value and the value before and after is higher than the
#     (value-outlier) then value = NaN
# outlier = int(float(input("Please enter minimum height difference to detect outliers (1.5):
#     ")))
outlier = 1.5
###########################################################################

file.loc[file['height_x'] >= 999, 'height_x'] = np.nan
file.loc[file['height_x'] <= 5, 'height_x'] = np.nan


for i, value in enumerate(file['height_x']):
    if i == 0 or i == len(file)-1:
        continue
```

```python
    elif file.iloc[i,1] < file.iloc[i-1,1]-outlier and file.iloc[i,1] < file.iloc[i+1,1]-
        outlier:
        file.iloc[i,1]=np.nan

file["height_x"]=file["height_x"].interpolate(method='linear')

file=file.dropna(subset=['height_x'])
file = file.reset_index(drop=True)



#############################################################################
# FILTER - REMOVAL OF AIRCRAFT MOTION
# Hibler Method:
    # 1. high pass filter
    # 2. Minumum points (from filtered profile) with corresponding height value
    #    (from unfiltered profile) and position:
            # select minimum point
            # searching the region ahead within a defined window width
        # construct curve from straight line segments
    # 3. low pass filter on curve from step 2.
#resulting smooth curve is the modelled flight trajectory

#lamda_hp = float(input("Please enter highpass-filter cut-off wavelength in m (60): "))
lamda_hp = 60 #m cut-off wavelentgh (everything greater than lamda_hp is filtered out)

#lamda_lp = float(input("Please enter lowpass-filter cut-off wavelength (60): "))
lamda_lp = 60 #m cut-off wavelength (everything smaller lamda_lp is filtered out)

logging.info('filter, lamda_hp = %f, lamda_lp %f'%(lamda_hp, lamda_lp))
#############################################################################

n=len(file.index)
DX = file.iloc[n-1,12]/n

#test of butterworth filter_____
# fs = 1000 # Sampling frequency
# # Generate the time vector properly
# t = np.arange(1000) / fs

# plt.figure()

# signala = np.sin(2*np.pi*100*t) # with frequency of 100
# plt.plot(t, signala, label='a')

# signalb = np.sin(2*np.pi*20*t) # frequency 20
# plt.plot(t, signalb, label='b')

# signalc = signala + signalb
# plt.plot(t, signalc, label='c')

# fc = 30 # Cut-off frequency of the filter
```

```python
# w = fc / (fs / 2) # Normalize the frequency
# b, a = signal.butter(5, w, 'high')
# output = signal.filtfilt(b, a, signalc)
# plt.plot(t, output, label='result')


#BUTTERWORTH HIGHPASS_____

fc = 1/(lamda_hp/DX)

b, a = signal.butter(5, fc, 'high')

file['filt_sig'] = signal.filtfilt(b, a, file['height_x'])


#BUTTERWORTH MINIMUM POINTS _____

#step_1 = int(float(input("Please enter minimum point spacing in m (10): "))/DX)
#step_2 = int(float(input("Please enter smallest maximum point spacing in m (40): "))/DX)
#step_3 = int(float(input("Please enter medium maximum point spacing in m (70): "))/DX)
#step_4 = int(float(input("Please enter largest maximum point spacing in m (100): "))/DX)

step_1 = int(10/DX)
step_2 = int(40/DX)
step_3 = int(70/DX)
step_4 = int(100/DX)


minimum = 0
for i in range(n-1):
    if i + step_4 >= n:
        break

    elif i == minimum:


        if file.iloc[i+step_1:i+step_3,14].std() <= 0.1:
            minimum = file.iloc[i+step_1:i+step_2,14].idxmax()
            file.iloc[minimum,15] = file.iloc[minimum,14]

        elif file.iloc[i+step_1:i+step_3,14].std() <= 0.4:
            minimum = file.iloc[i+step_1:i+step_3,14].idxmax()
            file.iloc[minimum,15] = file.iloc[minimum,14]

        else:
            minimum = file.iloc[i+step_1:i+step_4,14].idxmax()
            file.iloc[minimum,15] = file.iloc[minimum,14]


file.loc[file['minimum_points'] > 0, 'minimum_curve'] = file['height_x']
file['minimum_curve']=file['minimum_curve'].interpolate(method='linear')

drop_idx = next(i for i, value in enumerate(file['minimum_curve']) if value >= 0)
```

```python
file = file.iloc[drop_idx:,]
file = file.reset_index(drop=True)
n = len(file.index)

#BUTTERWORTH LOWPASS_____

fc = 1/(lamda_lp/DX)

b, a = signal.butter(5, fc, 'low')

file['motion'] = signal.filtfilt(b, a, file['minimum_curve'])


###########################################################################
#CUT TO 20 m
logging.info('CUT TO 20 m')
###########################################################################

#save FID where data is cut
cut = pd.DataFrame()
cut['start']=np.zeros(1)
cut['end']=np.zeros(1)

file.loc[file['motion'] > 40, 'height_x'] = 100.0
file.loc[file['motion'] < 6, 'height_x'] = 100.0

#Start
if file.iloc[0,1] == 100:
    start_idx = next(idx for idx, value in enumerate(file['height_x']) if value <= 20)
    cut['start']=file.iloc[start_idx,0]
else:
    cut['start']=file.iloc[0,0]
    start_idx = 0

#End
if file.iloc[n-1,1] == 100:
    end_idx = next(idx for idx, value in reversed(list(enumerate(file['height_x']))) if value
        <= 20)
    cut['end']=file.iloc[end_idx,0]
else:
    cut['end']=file.iloc[n-1,0]
    end_idx = n-1

#eliminate Start & End
file = file.iloc[start_idx:end_idx+1,]
file = file.reset_index(drop=True)

#find the amount of zero-measurments
nummer,_ = signal.find_peaks(file['height_x'], height = 40, prominence = 40)
amount_zero_measurements = len(nummer)
```

```python
#Cut zero-measurements
logging.info('Cut zero-measurements')
n = len(file)
zero_measurements_interate = 0
e=0

while amount_zero_measurements > zero_measurements_interate:

    #in case the section is already cut out
    if nummer[zero_measurements_interate]<= e and e!=0:

        zero_measurements_interate += 1
        amount_zero_measurements = amount_zero_measurements - 1

        continue

    else:

        zero_initial_idx = next(idx for idx, value in enumerate(file['height_x']) if value ==
            100)

        s=0
        i=zero_initial_idx
        while s==0 and i<=n:
            if file.iloc[i,1] < 20 and file.iloc[i,1] >= 17:
                s=i
            else:
                i = i-1

        e=0
        i=zero_initial_idx
        while e==0 and i<=n:
            if file.iloc[i,1] < 20 and file.iloc[i,1] >= 17:
                e=i
            else: i = i+1

        file.iloc[s+1:e,1]=np.nan

        cut = cut.append({'start':file.iloc[s,0],'end':file.iloc[e,0]}, ignore_index =True)

        zero_measurements_interate += 1

        file = file.dropna(subset=['height_x'])

file = file.reset_index(drop=True)


############################################################################
#PROFILELENGTH
#cotnains only measurements < 20 m
```

```python
logging.info('profilelength')
###############################################################################

n = len(file)
profilelength = 0
s=0
e=0

if amount_zero_measurements == 0:
    profilelength = file.iloc[-1,12]-file.iloc[0,12]
elif amount_zero_measurements > 0:
    profilelength = file.iloc[-1,12]-file.iloc[0,12]
    for i in range(amount_zero_measurements):

            s = file[file['gpst']==cut.iloc[i+1,0]].index.values[0]
            e = file[file['gpst']==cut.iloc[i+1,1]].index.values[0]

            profilelength = profilelength - (file.iloc[e,12]-file.iloc[s,12])


###############################################################################
#PROFILE
#substract aircraft motion from measured laser altimeter height
logging.info('surface profile')
###############################################################################

file['profile'] = file['motion'] - file['height_x']

# amount of data below zero - quantile 5%
below_zero = np.nanquantile(file['profile'], 0.05)

#level ice
zero = np.zeros(n)

###############################################################################
# DROP MISSING VALUES
# drop data with more than q continues missing values

#q = int(float(input("Please enter amount of coherent missing values that are dropped from the
      profile (8): ")))
q = 8

logging.info('drop data with more than %i continues missing values'%q)
###############################################################################

missing_distance = 0

i = 0
idx = 0
idx_last = 0
while i < len(file):
```

```python
        if math.isnan(file.iloc[i,19]) == True :
            idx = i+1
            while idx < len(file)-1 and math.isnan(file.iloc[idx,19])== True:
                idx = idx+1

            #set to nan if datagap is > q points
            if idx - i > q:
                #set profile to nan
                file.iloc[i:idx,18] = np.nan

                #adjust usable profilelength
                missing_distance = missing_distance + (file.iloc[idx,12]-file.iloc[i,12])


                #set to nan if data is < q points
                if idx_last != 0 and (i - idx_last) <= q:
                    file.iloc[idx_last:i,18] = np.nan

                    #adjust usable profilelength
                    missing_distance = missing_distance + (file.iloc[i,12]-file.iloc[idx_last,12])

                idx_last = idx


            i = idx +1

        else:
            i = i+1


profilelength = profilelength - missing_distance



##########################################################################
#AVERAGE POINT SPACING
logging.info('average point spacing')
##########################################################################

DX = file['DX'].mean()



##########################################################################
#RIDGES & STATISTICS

# min_height_peak = float(input("Please enter minimum ridge height in m (0.8): "))
min_height_peak = 0.8            # minimum ridge height/ cut-off value

#width = int(float(input("Please enter maximum flank width of ridge in m (20): "))/DX)
width = int(20/DX)               # only ridges with a flank width below 20 m are detected

# trsh = float(input("Please enter threshhold/ height of ridge border in m (0.3): "))
trsh =  0.3                      # border threshold
```

```python
##peak_distance = int(float(input("Please enter minimum distance between ridges in m (10): "))
    /DX)
peak_distance = int(10/DX)

logging.info('ridges & statistics')
##############################################################################

logging.info('... min_height_peak = %f'%min_height_peak)
logging.info('... width = %f'%width)
logging.info('... trsh = %f'%trsh)
logging.info('... peak_distance = %f'%peak_distance)

ridge = pd.DataFrame()
ridge['profile'] =file['profile']    #0
ridge['distance'] = file['dis']       #1
ridge['peak']= np.nan                 #2
ridge['ridge']=np.nan                 #3
ridge['lborder']=np.nan               #4
ridge['rborder']=np.nan               #5
ridge['width']=np.nan                 #6
ridge['width_line']=np.nan            #7
ridge['ridge_height']=np.nan          #8
ridge['spacing']=np.nan               #9
ridge['gpst']=file['gpst']            #10


# set values next to zero measurement to nan -> avoid ridge width error
i=1
if amount_zero_measurements != 0:
    while i <= len(cut)-1:

        #start zero meaurement
        s = cut.iloc[i,0]
        #end zero measurement
        e = cut.iloc[i,1]

        for idx, value in enumerate(ridge['gpst']):
            if value == s or value == e:
                ridge.iloc[idx,0]= np.nan

        i = i+1

#find local maxima
maxima, _ = signal.find_peaks(ridge['profile'], height = min_height_peak, distance =
    peak_distance)

#mark detected maxima in dataframe
for i, value in enumerate(maxima):
    ridge.iloc[value,2] = 1       #peak
    ridge.iloc[value,3] = 1       #ridge
```

```python
last_e = 0
last_ridge = 0
for i, value in enumerate(ridge['ridge']):

    if ridge.iloc[i,3]==1:

        #check left side
        j = i-1
        j_width = 0
        s=0
        e=0
        while j_width <= width:
            if i<=0 or i>= len(ridge) or j<=0 or j>=len(ridge):
                ridge.iloc[i,3] = np.nan
                break
            elif math.isnan(ridge.iloc[j,0]) == True:
                ridge.iloc[i,3] = np.nan
                break
            elif ridge.iloc[j,0] >= ridge.iloc[i,0]:
                ridge.iloc[i,3] = np.nan
                break
            elif ridge.iloc[j,0]<(0.5*ridge.iloc[i,0]):
                if ridge.iloc[j,0]>trsh and math.isnan(ridge.iloc[j,5]) == True:
                    j = j-1
                else:
                    ridge.iloc[j,4] = 1
                    s = j
                    break
            else:
                j = j-1

                j_width = j_width+1


        ##check right side
        if ridge.iloc[i,3]==1:
            j = i+1
            j_width = 0
            while j_width <= width:
                if i<=0 or i>=len(ridge) or j<=0 or j>=len(ridge):
                    ridge.iloc[i,3] = np.nan
                    break
                elif math.isnan(ridge.iloc[j,0]) == True:
                    ridge.iloc[i,3] = np.nan
                    break
                elif ridge.iloc[j,0] >= ridge.iloc[i,0]:
                    ridge.iloc[i,3] = np.nan
                    break
```

```python
            elif ridge.iloc[j,0]<(0.5*ridge.iloc[i,0]):

                    #border is where threshold value is or where maxima is shared by two
                        neighboring ridges
                    if ridge.iloc[j,0]>trsh and math.isnan(ridge.iloc[j,4]) == True:
                        j = j+1
                    else:
                        ridge.iloc[j,5] = 1
                        e = j
                        break
                else:
                    j = j+1

                    j_width = j_width+1

        if e > 0 and s > 0 and e <len(ridge) and s < len(ridge):

            #check width
            if ridge.iloc[i,3]==1:
                ridge.iloc[i,6] = ridge.iloc[e,1]-ridge.iloc[s,1] #width of ridge
                ridge.iloc[s:e+1,7]=0                             #ridge width line for plotting
                ridge.iloc[s:e+1,8]= ridge.iloc[s:e+1,0]        #ridge height values

            #check ridge spacing
                if last_e != 0:
                    ridge.iloc[last_ridge,9] = ridge.iloc[s,1] - ridge.iloc[last_e,1] #distance
                        in m between this and last ridge

                last_e = e
                last_ridge = i
        else:
            ridge.iloc[i,3] = np.nan


#remove ridge spacing where a zero-measurement is inbetween ridges
i=1
if amount_zero_measurements != 0:
    while i <= len(cut)-1:

        fid_s = cut.iloc[i,0]

        idx = ridge[ridge['gpst']==fid_s].index.values[0]

        file.iloc[idx,18] = np.nan

        stop = 0

        while idx > 0 and stop !=1:

            idx = idx-1
```

```python
            if ridge.iloc[idx,9]>0:
                ridge.iloc[idx,9] = np.nan
                stop = 1

                break
        i = i+1

#replace indicator with height value
ridge.loc[ridge['peak']== 1, 'peak']=ridge['profile']
ridge.loc[ridge['ridge']== 1, 'ridge']=ridge['profile']
ridge.loc[ridge['lborder']== 1, 'lborder']=ridge['profile']
ridge.loc[ridge['rborder']== 1, 'rborder']=ridge['profile']


##########################################################################
#ridge statistics_____

ridge_amount = ridge['ridge'][ridge['ridge'] > 0].count()

ridge_height_mean = ridge['ridge_height'].mean(skipna=True)

ridge_highest_peak_height_mean = ridge['ridge'].mean(skipna=True)

maximum_ridge = ridge['ridge_height'].max()

ridge_mean_width = ridge['width'].mean(skipna=True)

ridge_mean_spacing = ridge['spacing'].mean(skipna=True)

ridge_density = 1000*ridge_amount/profilelength

ridge_intensity = ridge['ridge_height'].mean(skipna=True) / ridge['spacing'].mean(skipna=True)


# roughness parameters_____
#####Ra     mean height
Ra = file['profile'].mean()

#####Rq     RMS height
Rq = np.sqrt((file['profile']**2).mean())

#####Rstd - standard deviation
Rstd = np.std(file['profile'])

#####Rsk - Skewness
Rsk = (((file['profile'] - file['profile'].mean()) / np.std(file['profile'])) ** 3).mean()

#####Rku - Kurtosis
Rku = ((((file['profile'] - file['profile'].mean()) / np.std(file['profile'])) ** 4)-3).mean()

#####RMS Slope
```

```python
def allan(dis,x):

    allan = 0
    n = 0
    for i, value in enumerate(x):
        if i + dis >= len(x):
            break

        allan = allan + ((file.iloc[i+dis, 18] - file.iloc[i, 18])**2)
        n=n+1

    allan = np.sqrt(allan/n)

    return allan


#3 m
RMS_Slope_3 = math.atan(allan(int(3/DX), file['profile'])/3)



#Roughness parameters for 2 km_____

if profilelength <= 2000:
    print('Profile is shorter than two kilometers.')
else:

    rough = pd.DataFrame(np.nan, index=range(0,int(profilelength/2000)), columns=['Ra', 'Rq','
        Rstd','Rsk','Rku','Rslope3'])

    n=0
    i = 0
    while n < int(profilelength/2000):

        #Ra
        rough.iloc[n,0] = file.iloc[i:i+2000,18].mean()

        #Rq
        rough.iloc[n,1] = np.sqrt((file.iloc[i:i+2000,18]**2).mean())

        #Rstd
        rough.iloc[n,2] = np.std(file.iloc[i:i+2000,18])

        #Rsk
        rough.iloc[n,3] = (((file.iloc[i:i+2000,18] - file.iloc[i:i+2000,18].mean()) / np.std(
            file.iloc[i:i+2000,18])) ** 3).mean()

        #Rku
        rough.iloc[n,4] = ((((file.iloc[i:i+2000,18] - file.iloc[i:i+2000,18].mean()) / np.std(
            file.iloc[i:i+2000,18])) ** 4)-3).mean()


        #RMS slope 3 m
```

```python
        rough.iloc[n,5] = math.atan(allan(int(3/DX), file.iloc[i:i+2000,18])/3)

        i = i+2000
        n = n+1



################################################################################
#PLOTS
logging.info('plots')
################################################################################

figs = {}
#minimum points/ filter results_____
figs['filter'] = make_subplots(rows=2, cols=1, shared_xaxes=True,
                    x_title='distance [m]',
                    y_title='height [m]')

#altimeter measurement
figs['filter'].append_trace(
    go.Scatter(
    x = file['dis'],
    y = file['height_x'],
    mode = 'lines',
    line=dict(color="Green"),
    name = 'laser altimeter'),
    row=1, col=1)

#curve composed of straight line segments between minimum points
figs['filter'].append_trace(
    go.Scatter(
    x = file['dis'],
    y = file['minimum_curve'],
    mode = 'lines',
    line=dict(color="Orange"),
    name = 'minimum curve'),
    row=1, col=1)

#flight trajectory
figs['filter'].append_trace(
    go.Scatter(
    x = file['dis'],
    y = file['motion'],
    mode = 'lines',
    line=dict(color="LightGreen"),
    name = 'LP-filter result (flight trajectory)'),
    row=1, col=1)

#high pass result
figs['filter'].append_trace(
    go.Scatter(
    x = file['dis'],
```

```python
        y = file['filt_sig'],
        mode = 'lines',
        line=dict(color="LightBlue"),
        name = 'HP-filter result'),
        row=2, col=1)

#minimum points
figs['filter'].append_trace(
    go.Scatter(
    x = file['dis'],
    y = file['minimum_points'],
    mode = 'markers',
    line=dict(color="Orange"),
    name = 'minimum points'),
    row=2, col=1)

figs['filter'].update_layout(template='plotly_white', title=date+' minimum points')

# plotly.offline.plot(figs['filter'], filename=date+"_Minimum_Points")


#profile _____
figs['profile'] = make_subplots(rows=2, cols=1, shared_xaxes=True,
                x_title='distance [m]',
                y_title='height [m]')

#surface elevation
figs['profile'].append_trace(
    go.Scatter(
    x = file['dis'],
    y = file['profile'],
    mode = 'lines',
    line=dict(color="LightGrey"),
    name = 'surface elevation'),
    row=1, col=1)

#level ice
figs['profile'].append_trace(
    go.Scatter(
    x = file['dis'],
    y = zero,
    mode = 'lines',
    line=dict(color="DimGrey"),
    name = 'level ice'),
    row=1, col=1)

#altimeter measurement
figs['profile'].append_trace(
    go.Scatter(
    x = file['dis'],
    y = file['height_x'],
```

```python
        mode = 'lines',
        line=dict(color="Green"),
        name = 'laser altimeter'),
        row=2, col=1)

#flight trajectory
figs['profile'].append_trace(
    go.Scatter(
    x = file['dis'],
    y = file['motion'],
    mode = 'lines',
    line=dict(color="LightGreen"),
    name = 'flight trajectory'),
    row=2, col=1)

figs['profile'].update_layout(template='plotly_white', title=date+' surface elevation')

# plotly.offline.plot(figs['profile'], filename=date+"_surface_elevation")


#ridge identifification_____

figs['ridge'] = make_subplots(rows=2, cols=1, shared_xaxes=True,
                    x_title='distance [m]',
                    y_title='height [m]')

#surface elevation
figs['ridge'].append_trace(
    go.Scatter(
    x = file['dis'],
    y = file['profile'],
    mode = 'lines',
    line=dict(color="LightGrey"),
    name = 'surface elevation'),
    row=1, col=1)

#level ice
figs['ridge'].append_trace(
    go.Scatter(
    x = file['dis'],
    y = zero,
    mode = 'lines',
    line=dict(color="DimGrey"),
    name = 'level ice'),
    row=1, col=1)

#ridge (width)
figs['ridge'].append_trace(
    go.Scatter(
    x = file['dis'],
    y = ridge['width_line'],
```

```python
        mode = 'lines',
        line=dict(color="Red"),
        name = 'ridge'),
        row=1, col=1)


#peaks
figs['ridge'].append_trace(
        go.Scatter(
        x = file['dis'],
        y = ridge['peak'],
        mode = 'markers',
        line=dict(color="LightBlue"),
        name = ('peak (>'+str(min_height_peak)+' m)')),
        row=1, col=1)


#highest peak
figs['ridge'].append_trace(
        go.Scatter(
        x = file['dis'],
        y = ridge['ridge'],
        mode = 'markers',
        marker=dict(color='LightBlue', line=dict(color='Blue', width=1)),
        name = 'highest peak'),
        row=1, col=1)


#altimeter measurement
figs['ridge'].append_trace(
        go.Scatter(
        x = file['dis'],
        y = file['height_x'],
        mode = 'lines',
        line=dict(color="Green"),
        name = 'laser altimeter'),
        row=2, col=1)


#flight trajectory
figs['ridge'].append_trace(
        go.Scatter(
        x = file['dis'],
        y = file['motion'],
        mode = 'lines',
        line=dict(color="LightGreen"),
        name = 'flight trajectory'),
        row=2, col=1)

figs['ridge'].update_layout(template='plotly_white', title=date+' ridges')

# plotly.offline.plot(figs['ridge'], filename=date+"_ridges")
```

```python
########################################################################
#HISTOGRAMM
########################################################################
logging.info('histogram')

#histogram log scale_____
updatemenus = list([
    dict(active=1,
         buttons=list([
            dict(label='Log Scale',
                method='update',
                args=[{'visible': [True]},
                      {'yaxis': {'type': 'log', 'title':"count"}}]),
            dict(label='Linear Scale',
                method='update',
                args=[{'visible': [True]},
                      {'yaxis': {'type': 'linear', 'title':"count"}}])
         ]),
    )
])


#ridge height_____
figs['ridge_height'] = go.Figure()
figs['ridge_height'].add_trace(go.Histogram(
    x=ridge['ridge_height'],
    name='ridge height',
    xbins=dict(start = 0, size=0.1),
    marker_color='LightBlue'))

figs['ridge_height'] .update_layout(
    updatemenus=updatemenus,
    template='plotly_white',
    title_text='ridge height',
    xaxis_title_text='height [m]',
    yaxis_title_text='count',
    bargap=0.05)

#plotly.offline.plot(figs['ridge_height'])

#highest ridge peak height_____
figs['ridge_peak'] = go.Figure()
figs['ridge_peak'].add_trace(go.Histogram(
    x=ridge['ridge'],
    name='highest ridge peak height',
    xbins=dict(start=min_height_peak, size=0.1),
    marker_color='LightBlue'))

figs['ridge_peak'].update_layout(
    updatemenus=updatemenus,
    template='plotly_white',
    title_text='highest ridge peak height',
```

```python
    xaxis_title_text='height [m]',
    yaxis_title_text='count',
    bargap=0.05)

#plotly.offline.plot(figs['ridge_peak'], filename=date+"_ridge_height")


#spacing_____
figs['spacing'] = go.Figure()
figs['spacing'].add_trace(go.Histogram(
    x=ridge['spacing'],
    name='ridge spacing',
    xbins=dict(start=0,size=50),
    marker_color='LightBlue'))

figs['spacing'].update_layout(
    updatemenus=updatemenus,
    template='plotly_white',
    title_text='ridge spacing',
    xaxis_title_text='distance [m]',
    yaxis_title_text='count',
    bargap=0.05)

#plotly.offline.plot(figs['spacing'], filename=date+"_ridge_distance")


#surface elevation _____
figs['height'] = go.Figure()
figs['height'].add_trace(go.Histogram(
    x=ridge['profile'],
    name='distribution of sea ice thickness with respect to level ice',
    xbins=dict(start = -1, size=0.1),
    marker_color='LightBlue'))

figs['height'].update_layout(
    updatemenus=updatemenus,
    template='plotly_white',
    title_text='distribution of sea ice thickness with respect to level ice',
    xaxis_title_text='height [m]',
    yaxis_title_text='count',
    bargap=0.05)

#plotly.offline.plot(figs['height'])


##############################################################################
# CSV
logging.info('csv')
##############################################################################

csv_output = pd.DataFrame()
```

```python
csv_output['fid'] = file['gpst']                              #0
csv_output['lat'] = file['lat']                               #1
csv_output['lon'] = file['lon']                               #2
csv_output['distance[m]'] = file['dis']                       #3
csv_output['altimeter_height[m]'] = file['height_x']          #4
csv_output['modelled_trajectory[m]'] = file['motion']         #5
csv_output['profile_height[m]'] = file['profile']             #6
csv_output['ridge_peak[m]'] = ridge['ridge']                  #7
csv_output['left_border[m]'] = ridge['lborder']               #8
csv_output['right_border[m]'] = ridge['rborder']              #9
csv_output['width[m]'] = ridge['width']                       #10
csv_output['spacing[m]'] = ridge['spacing']                   #11
csv_output['ridge_heights[m]'] = ridge['ridge_height']        #12

if allfinal_file != "":
    csv_output['d'] = file['d']                               #13
    csv_output['m'] = file['m']                               #14
    csv_output['y'] = file['y']                               #15
    csv_output['EM'] = file['EM_height']                      #16
else:
    csv_output['d'] = np.nan
    csv_output['m'] = np.nan
    csv_output['y'] = np.nan
    csv_output['EM'] = np.nan


############################################################################
#SAVE
############################################################################
logging.info('save')

file_name = arglist['outname']
file_name_html = file_name + ".html"
file_name_txt = file_name + ".txt"
file_name_csv = file_name + ".csv"

if os.path.exists(file_name_html) == True and arglist.get('overwrite') == False:
    logging.warning("no data saved")
else:
    txt_data = (date, profilelength, Ra, ridge_amount, ridge_height_mean,
            ridge_highest_peak_height_mean,
        maximum_ridge, ridge_mean_width, ridge_mean_spacing, ridge_density, ridge_intensity,
            min_height_peak, Ra, Rq, Rsk)

    save_html(file_name_html, txt_data, figs)

    save_txt(file_name_txt, txt_data)

    csv_output.to_csv(path_or_buf = file_name_csv, index=False, header=True, sep=";",
        float_format='%.7f')
```

```
###########################################################################
###########################################################################


if __name__=='__main__':
    main()
```

C Acknowledgement

I would like to thank for helping with this research project:

The Sea Ice Physics Section of the Alfred Wegener Institute for Polar and Marine Research, which provided me with the data and gave me the opportunity to gain insight into the research. Especially Dr. Krumpen as well as Dr. Belter, who gave me the idea, always encouraged me and offered to help if I had any questions.

The Department of Meteorology of the University Trier. Dr. Willmes as well as Prof. Dr. Heinemann for the supervision and the connection to the Alfred-Wegener-Institute, as well as Dr. Drüe for the help with content related questions.

My family and friends for the emotional support, who cheered me up and gave me motivation.

D Eidesstattliche Erklärung

Hiermit erkläre ich, dass ich die Bachelorarbeit selbstständig verfasst und keine anderen als die angegebenen Quellen und Hilfsmittel benutzt und die aus fremden Quellen direkt oder indirekt übernommenen Gedanken als solche kenntlich gemacht habe. Die Arbeit habe ich bisher keinem anderen Prüfungsamt in gleicher oder vergleichbarer Form vorgelegt. Sie wurde bisher nicht veröffentlicht.

———————————————   ————————————————————————
DATUM   UNTERSCHRIFT